Seismological Constraints on Inner Core Properties

by

Aimin Cao

B.S. (Yunnan University) 1989
M.S. (Chinese Academy of Science) 1995

A dissertation submitted in partial satisfaction of the
requirements for the degree of
Doctor of Philosophy

in

Geophysics

in the

GRADUATE DIVISION
of the
UNIVERSITY of CALIFORNIA at BERKELEY

Committee in charge:

Professor Barbara Romanowicz, Chair
Professor Douglas Dreger
Professor Richard Muller

Fall 2005

The dissertation of Aimin Cao is approved:

_____

Chair   Date

_____

                                                              Date

_____

                                                              Date

University of California at Berkeley

Fall 2005

Seismological Constraints on Inner Core Properties

Copyright Fall 2005

by

Aimin Cao

Abstract

Seismological Constraints on Inner Core Properties

by

Aimin Cao

Doctor of Philosophy in Geophysics

University of California at Berkeley

Professor Barbara Romanowicz, Chair

We constrain seismic properties of the inner core using various body wave observations. In the epicentral distance range of $10-70^o$, our high quality measurements of the amplitude ratio of PKiKP and PcP provide a new estimate of the density contrast (0.6-0.9 g/cm^3) at the Inner Core Boundary (ICB). This estimate is compatible with a recent reevaluation of normal mode data, and thus reconciles the long-term discrepancy between body wave and normal mode measurements. Our Q_α study based on the amplitude ratio of PKIKP and PKiKP reveals an attenuation transition at the top of the inner core. In the western hemisphere Q_α decreases first with depth from the ICB and then turns to increase at a depth of $\sim 85km$, and in the eastern hemisphere we infer that the attenuation transition takes place at the top $\sim 32km$ beneath the ICB. We find high Q_α and low velocity in the western hemisphere, and low Q_α and high velocity in the eastern hemisphere. This remarkable hemispherical pattern starts to disappear at a depth of $\sim 85km$. This might constrain the depth extent of the mushy zone at the top of the inner core. Taking advantage of the long-term high quality broadband $Gr\ddot{a}fenberg$ seismic array, we observed a reliable inner core shear wave phase PKJKP. Four kinds of evidence (travel time, slowness, back-azimuth, and comparison with a pseudo-liquid inner core model) are jointly presented. The high signal-to-noise waveform of PKJKP, for the first time, gives us an opportunity to constrain the inner core shear wave velocity and attenuation directly using body waves. The envelope modeling results suggest that, in the inner core, the shear wave velocity

may be slightly faster ($\sim 1.5\%$) and Q_β may be significantly larger ($\sim 315 \pm 150$) than obtained from normal mode observations. Taking into account the fact that normal mode data mainly sample the shallow portion of the inner core and PKJKP samples the central part, this implies that both shear wave velocity and Q_β increase with depth in the inner core.

<div style="text-align:right;">

_____

Professor Barbara Romanowicz
Dissertation Committee Chair

</div>

Contents

List of Figures

List of Tables

Acknowledgements

First of all, I would like to express sincere gratitude to my advisor, Prof. Barbara Romanowciz. Thanks for her great support and concern. She led me into an exciting field of study on the Earth's interior. Whenever I encountered tough issues (from data processing, manuscript writing, to paper revision), her enlightening instructions, suggestions, and comments would always help me out quickly.

I am also grateful to my committee members Prof. Doug Dreger and Prof. Richard Muller. Prof. Muller's encouragement and kindness made my oral exam much more smooth. His knowledge of geophysics surprised me during the exam. Even right now I still remember his good questions of that day. Prof. Dreger taught me two courses in strong motion seismology. His instructive teaching was very impressive. I was planning to work with him for a project on the Coast Ranges in northern California. But, unfortunately, I missed the opportunity. I wish to have other chance to work with him in the coming future.

Thanks to my former and current fellow group members, Nozomu Takeuchi, Yuangchen Gung, Mark Panning, Akiko To, Junkee Rhie, Sebastien Rousset, Alexey Shulgin, Ved Lekic, and others for their help and stimulating discussions. Charley Paffenbarger, Eleanor Blair, and Bob Uhrhammer provided invaluable assistance in my research.

Finally, I am indebted to my family. Without the support and sacrifice of my wife, Yan Zhao, I could not have finished this dissertation!

Chapter 1

Introduction

Before 1936, the Earth was considered as a sphere with three shells (a solid crust, mantle, and a liquid core) (e.g., [*Oldham*, 1906; *Jeffreys*, 1924]). Due to the remarkably lower velocity in the core than in the mantle, there exists a "shadow zone" in the epicentral distance range of 103° to 143°, seismic phases were supposed to be barely observed in the "shadow zone".

However, the above knowledge was severely challenged after the great New Zealand earthquake ($M_s = 7.6$) in 1929. A large number of European seismic stations, which were located in the range of the "shadow zone", recorded clear P wave onsets (now called PKIKP). These phases were generally described as diffracted phases by the mid 1930s. It was *Lehmann* (1936) who suggested the existence of the inner core and interpreted the phases as refracted waves from the top of the inner core.

This breaking view was soon accepted. Birch (1940) further suggested that the inner core should be solid due to the freezing of the liquid iron in the outer core. Thirty years later, *Dziewonski and Gilbert* (1971) found the first seismic evidence of the solidity of the inner core from normal mode observations. The direct evidence, PKJKP (traveling through the inner core as a shear wave), was also claimed [*Julian*

et al., 1972; *Okal & Cansi*, 1998], but these were soon proved to be misidentifications [*Doornbos*, 1974; *Deuss et al.*, 2000].

The absence of direct evidence of the solidity of the inner core has not hindered studies of the inner core structure at all. In fact, even before the presentation of the indirect evidence [*Dziewonski & Gilbert*, 1971], the inner core attenuation study had already started. Short-period body wave observations suggested that Q_α (P-wave quality factor) is very low beneath the Inner Core Boundary (ICB) and increases with depth [*Sacks*, 1969]. A mushy layer may exist at the top of the the inner core [*Doornbos*, 1974; *Fearn et al.*, 1981; *Loper & Fearn*, 1983]. This is because the liquid outer core material is not pure iron. There are about 10% of the light elements such as Si, O, C, or S. During the freezing process, some of light elements are excluded from the inner core to power the geodynamo [*Braginsky*, 1963; *Gubbins et al.*, 2003] and the residual is kept within the inner core.

Based on the LASA (Large Aperture Seismic Array) data, *Engdahl* (1970) and *Bolt* (1977) observed PKiKP (reflected P wave on the outside of the ICB) and PKIIKP (reflected P wave on the inside of the ICB), respectively. The sharp onsets of PKiKP and PKIIKP revealed that the ICB is very sharp (only a few kilometers thick), and their travel times gave a tight constraint on the radius of the inner core ($\sim 1,216km$).

The successful observations of PKiKP (together with PcP) in the short epicentral distance range ($\sim 10^o$) also make it possible to estimate the density contrast at the ICB by means of amplitude ratios. *Bolt and Qamar* (1970) first suggested that the density contrast should be less than 1.8 gcm^{-3} at the ICB. In 1990, *Shearer and Masters* further reduced the maximum bound on the density contrast down to 1.0 gcm^{-3} based on the PKIKP/PcP ratio in a larger epicentral distance range of $10 - 70^o$. On the other hand, estimates of the density contrast based on normal mode observations are much smaller [*Dziewonski & Gilbert*, 1971; *Gilbert et al.*, 1973; *Masters*, 1979]. In the preliminary reference earth model (PREM) [*Dziewonski & Anderson*, 1981], which is based on from normal mode data, the contrast is only 0.6

gcm^{-3}.

In 1986, the seismic structure of the inner core was suggested to be anisotropic from both body wave [*Morelli et al.*, 1986] and normal mode [*Woodhouse et al.*, 1986] observations. The P-wave velocity in the inner core along polar paths may be faster than along equatorial paths. Subsequent studies provided more complicated and more controversial inner core anisotropic views. The P-wave velocity anisotropy might increase with depth (e.g., [*Vinnik et al.*, 1994; *Song*, 1996]); the anisotropy might be much weaker in the quasi-eastern hemisphere than in the quasi-western hemisphere in the depth range from 100 to 400 km [*Tanaka & Hamaguchi*, 1997; *Creager*, 1999]. At the top of the inner core ($< \sim 100km$), P-wave velocity might be isotropic and faster in the quasi-eastern hemisphere than in the quasi-western hemisphere [*Niu & Wen*, 2001; *Garcia*, 2002].

The above complexity of the inner core anisotropy was questioned by *Romanowicz et al.* (2002) and *Ishii et al.* (2002), respectively. *Romanowicz et al.* suggested that the complex lateral variation of P-wave velocity could be due to the mantle (or elsewhere) heterogeneity. And *Ishii et al.* suggested that there might be no an isotropic layer at the top of the inner core and that a constant anisotropy model in the whole inner core may explain both body wave and normal mode observations. In contrast, still based on normal mode observations, *Beghein and Trampert* (2003), instead, suggested a layered anisotropic model in the inner core.

On the other hand, recent studies of inner core attenuation based on short-period and broadband observations confirmed *Sacks'* (1969) suggestion that Q_α increases with depth [*Souriau & Roudil*, 1995; *Li & Cormier*, 2002]. Meanwhile, similar to the P-wave velocity anisotropy, Q_α was also revealed to be anisotropic [*Souriau & Romanowicz*, 1996].

It is evident that great progress has been made in studies of the inner core seismic structure. However, there are still a lot of unsettled issues. For example, (1) there is a significant discrepancy in estimates of the density contrast at the ICB from body

waves and normal modes. A much tighter constraint on $\Delta\rho_{ICB}$ is expected for the geodynamo study. (2) How deep is the suggested mushy layer in the inner core? Does it go deep into the center [*Loper & Fearn*, 1983] or is it strongly confined at the top of the inner core? (3) The dramatic contrast between the extremely high Q_α ($> 10,000$) in the outer core [*Cormier & Richards*, 1976] and the low Q_α in the inner core (~ 400) (increasing with depth towards the center) requires an attenuation transition at the top of the inner core, where Q_α should first decrease from the ICB and then increase with depth. This transition is intuitive, but it has not been observed yet. (4) Sixty-nine years have passed since *Lehmann* (1936) discovered the inner core, yet a reliable observation of PKJKP is still a controversial issue. *Deuss et al.* (2000) argued that previous PKJKP detections were not correct, but their own results are also problematic due to the induced artificial energy, incoherent signal, and interfering phases. (5) So far, the inner core shear wave attenuation has still been solely constrained by a few normal mode observations [*Dziewonski & Anderson*, 1981; *Widmer et al.*, 1991]. There is not any report on Q_β (S-wave quality factor) from the inner core shear body wave. This shortcoming has been impeding us to get a complete view of the inner core shear attenuation structure, because normal modes mainly sample the top of the inner core. Only PKJKP (or SKJKP) can penetrate the central portion of the inner core.

In this dissertation, we will discuss these issues. We start with the theoretical background (Chapter 2), where essential physical principles are systematically described. And then we provide a new estimate of $\Delta\rho_{ICB}$ (density contrast at the Inner Core Boundary) (Chapter 3), taking advantage of the recent 10 year (1990 to 1999) IRIS broadband dataset. We employ a new approach to process PKIKP and PKiKP phases at the top of the inner core (Chapter 4). It makes it possible to associate the mushy layer and the P-wave attenuation transition together. Finally, we present a reliable observation of PKJKP (Chapter 5), which settles a long-term concern in seismology. Based on our observed high signal-to-noise PKJKP waveform, we obtain a body-wave constraint on the shear wave attenuation in the inner core (Chapter 6).

In Chapter 2, we address the essential theories involved in our studies. The inner core is beneath the heterogeneous crust and mantle, $\sim 5,100$ km deep into the Earth's interior. Therefore, whenever we try to interpret our observations of the inner core seismic structure, an inevitable issue we have to face is the heterogeneity of the crust and the mantle. At present there are generally two distinct ways to reduce their influence: doing the correction of crust and mantle effects or using two phases whose ray paths are close in the crust and mantle. The first method is mainly used in studies of the P-wave velocity structure of the inner core. For the density contrast at the ICB (Chapter 3), inner core compressional and shear wave attenuation (Chapter 4 and 6), and the inner core shear wave velocity (Chapter 5), we have to use the second method (or both).

The theoretical calculation of the amplitude ratio of two phases is the cornerstone of this dissertation. It consists of two steps. The first step is to compute the reflection and transmission coefficients of a ray at each discontinuity (section 2.1). Here we focus on the discontinuities specifically for cases (solid-liquid and liquid-solid) of the core phases, which most seismological textbooks do not discuss in detail. The second step is to compute the geometrical spreading factor of the ray (section 2.2). The product of the calculated geometrical spreading factor and coefficients is the theoretical amplitude of the phase.

The computation of the theoretical amplitude ratio may provide us significant information on the inner core, but it is not enough for the study of PKJKP identification and the inner core shear wave attenuation. Synthetic waveform modeling is necessary. In section 2.3, we briefly review the Direct Solution Method (DSM) synthetic technique. PKJKP is a very elusive phase. A lot of unknown mantle and crust multiples, which are usually negligible, become serious interfering phases in the study of PKJKP. Therefore, the completeness and accuracy of the synthetics is important. The DSM is one of the few techniques eligible for this requirement. It directly solves the Galerkin weak form of the elastic equation of motion, and so we do not need to specify each ray path in advance.

In addition, because PKJKP is very weak, it is impossible to discern PKJKP without stacking of seismic array data. Among several stacking methods, we choose the Phase Weighted Stack (PWS) (section 2.4), as the PWS can resolve the arrival time and slowness better for the weak and coherent phases than other stacking methods.

In Chapter 3, we discuss the density contrast $\Delta\rho_{ICB}$ at the ICB. $\Delta\rho_{ICB}$ is an important parameter for the study of the geodynamo. *Stacey and Stacey* (1999) have argued that the dominant source of energy is the buoyancy from the released light elements from the inner core. If this conclusion is true, then the released energy, which drives the outer core convection, is proportional to the assumed density contrast. Based on the density contrast in the seismic reference model PREM [*Dziewonski & Anderson*, 1981], the inner core could not have existed more than 2 billion years ago. This is not consistent with the palaeomagnetic observations, which suggest that the earth has sustained a magnetic field for at least 3 billion years [*McElhinny & Senanayake*, 1980]. In order to discuss this issue, we search 10 year (from 1990 to 1999) IRIS broadband data. We find a number of high quality pairs of PKiKP and PcP records. Based on these high quality observations, we provide a $\Delta\rho$ which is compatible with a recent normal mode constraint [*Masters & Gubbins*, 2003]. Chapter 3 has been published in *Geophysical Journal International* under the reference [*Cao & Romanowicz*, 2004a].

In Chapter 4, we use PKIKP and PKiKP phases to study the top 100 km of the inner core. The ray paths of the two phases are very close in the mantle. Their separation at the Core Mantle Boundary (CMB) is less than $\sim 110km$. We obtain very consistent measurements of Q_α. The results illustrate a clear attenuation transition in the western hemisphere of the top of the inner core, where Q_α first decreases from extremely high ($> 10,000$) to much lower (~ 200) values, and then increases with depth towards to the center of the inner core. Chapter 4 has been published in *Earth and Planetary Science Letters* under the reference [*Cao & Romanowicz*, 2004b].

In Chapter 5, we present a convincing observation of PKJKP based on the high quality broadband seismic array data. When *Lehmann* (1936) discovered the inner

core, she could not tell whether the inner core is solid or liquid due to the limited seismic information at that time. It was from the geodynamo study that the inner core was suggested to be solid [*Birch*, 1940]. In order to confirm the solidity of the inner core, *Bullen* (1950, 1951) pointed out that the direct evidence is PKJKP. However, it is difficult to detect PKJKP. In fact, before the establishment of digital broadband seismic arrays, the observation of PKJKP seemed impossible. We discuss the reasons in section 5.2.

For the first time, four kinds of evidence (travel time, slowness, back-azimuth, and comparison with a pseudo-liquid inner core model) are jointly provided for an observation of PKJKP. The clear stacked PKJKP waveform which we obtain gives us an opportunity to characterize the shear wave velocity structure by means of the PKJKP synthetic modeling. Chapter 5 has been published in *Science* under the reference [*Cao et al.*, 2005].

In Chapter 6, we discuss the inner core shear wave attenuation. Because of the difficulty of the observation of PKJKP or other inner core shear wave phases (e.g., SKJKP), the inner core shear wave attenuation was solely constrained by normal mode observations. Our observed high signal-to-noise PKJKP waveform presents us an unprecedented opportunity to put a constraint on the shear wave attenuation by the body wave. In order to avoid the potential dispersion and phase shift caused by mantle heterogeneity, we use envelope modeling rather than direct waveform modeling.

The envelope function is the modulus of a complex trace. Its real part is the original trace and its imaginary part is the Hilbert transform of the original trace. In general, the envelope function can characterize the amplitude and arrival time better than the waveform because the possible phase shift is avoided. For example, after making 90 degree phase shift to an oberved seismic phase, the resulted waveform is different from the original one. At this moment, we cannot used the amplitude peak of the waveform to read the arrival time any longer. But their envelope functions are the same. We use the peak of the envelope function to read the arrival time of the maximum energy

of the phase.

We also do the back-ground noise experiments. The noise is taken from the realistic source (100 seconds in front of the first arrival). The experiments show us the potential uncertainty of the Q_β estimated by PKJKP. Our estimated Q_β is significantly larger than that constrained from normal mode observations. Chapter 6 has been submitted to *Earth and Planetary Science Letters* under the reference [*Cao & Romanowicz, 2005*].

Chapter 2

Theoretical Background

Summary

The theoretical calculation of the amplitude ratio between two distinct phases plays a key role in this dissertation. Compared with the synthetic waveform modeling, the amplitude ratio and phase shift computation sometimes may give us more clear and direct physical sense. For instance, when we observe PKJKP (Chapter 5), the theoretical amplitude ratio of PKJKP and PKIKP helps us solve two crucial issues (what is the favorable epicentral distance range to look for PKJKP and why the broadband seismic array is necessary to observe PKJKP); when we present the attenuation transition at the top of the inner core (Chapter 4), the calculated theoretical phase shift suggests us a direct and effective criterion for data processing; when we constrain the density contrast across the inner core boundary (Chapter 3), the fitting of the theoretical amplitude ratio of PKiKP and PcP reconciles the results from body waves and normal mode observations. However, most of seismology textbooks (e.g., [*Bullen*, 1963; *Aki & Richards*, 1980; *Bullen & Bolt*, 1985; *Aki & Richards*, 2002]) do not discuss it explicitly for cases equivalent to the core phases. Only *Ben-Menahem and Singh* (1981) mentions it briefly. Therefore, here it seems useful to give the detailed

formulations which apply to the core phases (sections 2.1 and 2.2). Then we will introduce the waveform synthetic technique called "Direct Solution Method (DSM)" (section 2.3) and the stacking method called "Phase Weighted Stack (PWS)" (section 2.4), which are used in Chapter 5 and 6 for the PKJKP study.

2.1 Reflection and Transmission Coefficient at CMB and ICB

In oder to calculate the amplitude ratio and the phase shift of two core phases (no depth phases taken into account here), the first step is to get their reflection and transmission coefficients at various discontinuities (solid-solid, solid-liquid, and liquid-solid) in the earth. The cases for the solid-solid discontinuities are well discussed in most textbooks on seismology. Here we only focus on the solid-liquid and liquid-solid cases for the Core Mantle Boundary and the Inner Core Boundary.

2.1.1 S to P conversion at the solid-liquid discontinuity

This applies to the PKJKP phase conversion at the ICB near the receiver side (Fig. 2.1). The incident phase is an SV wave. It is partitioned as reflected P and SV waves in the inner core and as refracted P wave in the outer core. In terms of P and SV wave potentials, the displacement and stress can be expressed as

$$\vec{u} = \vec{u_p} + \vec{u_s} = (\frac{\partial \phi}{\partial x_1} + \frac{\partial \psi}{\partial x_3})\vec{x_1} + (\frac{\partial \phi}{\partial x_3} - \frac{\partial \psi}{\partial x_1})\vec{x_3} \tag{2.1}$$

and

$$\sigma_{33} = \lambda\Delta^2\phi + 2\mu(\frac{\partial^2\phi}{\partial x_3^2} - \frac{\partial^2\psi}{\partial x_1\partial x_3}) \tag{2.2}$$

$$\sigma_{31} = \mu(2\frac{\partial^2\phi}{\partial x_1\partial x_3} - \frac{\partial^2\psi}{\partial x_1^2} + \frac{\partial^2\psi}{\partial x_3^2}) \tag{2.3}$$

where ϕ and ψ are P and SV potentials, respectively.

Based on conditions on continuity of displacement and stress at the boundary, the reflection and transmission coefficients may be readily derived.

At two sides of the boundary, the potentials of S and P wave can be represented by (e.g., [*Aki & Richards*, 1980])

$$
\begin{aligned}
\phi_1 &= A_2 exp[i\omega(px_1 - \eta_{\alpha_1}x_3 - t)] & (2.4)\\
\psi_1 &= B_1 exp[i\omega(px_1 + \eta_{\beta_1}x_3 - t)] &\\
&\quad + B_2 exp[i\omega(px_1 - \eta_{\beta_1}x_3 - t)] & (2.5)\\
\phi_2 &= A_3 exp[i\omega(px_1 + \eta_{\alpha_2}x_3 - t)] & (2.6)
\end{aligned}
$$

where B_1 is the amplitude for the incident SV wave, A_2 and B_2 are amplitudes for the reflected P and SV waves, A_3 is the amplitude for the refracted P wave, p is the ray parameter, and η is the vertical slowness.

The condition on the continuity of the normal displacement (2.1) gives

$$-\eta_{\alpha_1}A_2 - pB_1 - pB_2 = A_3\eta_{\alpha_2} \tag{2.7}$$

and conditions on the continuity of normal (2.2) and horizontal (2.3) stresses give

$$\frac{\lambda_1}{\alpha_1^2}A_2 + 2\mu_1(\eta_{\alpha_1}^2 A_2 - p\eta_{\beta_1}B_1 + p\eta_{\beta_1}B_2) = \frac{\lambda_2}{\alpha_2^2}A_3 + 2\mu_2\eta_{\alpha_2}^2 A_3 \qquad (2.8)$$

$$-2\eta_{\alpha_1} - (p^2 - \eta_{\beta_1^2})B_1 - (p^2 - \eta_{\beta_1^2})B_2 = 0 \qquad (2.9)$$

Thus we have the following set of equations

$$\begin{aligned}
-\eta_{\alpha_1}\frac{A_2}{B_1} - p\frac{B_2}{B_1} - \eta_{\alpha_2}\frac{A_3}{B_1} &= p \\
(\frac{\lambda_1}{\alpha_1^2} + 2\mu_1 p\eta_{\beta_1}^2)\frac{A_2}{B_1} + 2\mu_1 p\eta_{\beta_1}\frac{B_2}{B_1} - \frac{\lambda_2}{\alpha_2^2}\frac{A_3}{B_1} &= 2\mu_1 p\eta_{\beta_1} \\
-2\eta_{\alpha_1}p\frac{A_2}{B_1} - (p^2 - \eta_{\beta_1}^2)\frac{B_2}{B_1} &= p^2 - \eta_{\beta_1}^2
\end{aligned} \qquad (2.10)$$

And solutions are

$$\begin{pmatrix} \frac{A_2}{B_1} \\ \frac{B_2}{B_1} \\ \frac{A_3}{B_1} \end{pmatrix} = \begin{pmatrix} -\eta_{\alpha_1} & -p & -\eta_{\alpha_2} \\ \frac{\lambda_1}{\alpha_1^2} + 2\mu_1 p\eta_{\beta_1}^2 & 2\mu_1 p\eta_{\beta_1} & -\frac{\lambda_2}{\alpha_2^2} \\ -2\eta_{\alpha_1}p & -p^2 + \eta_{\beta_1}^2 & 0 \end{pmatrix}^{-1} \begin{pmatrix} p \\ 2\mu_1 p\eta_{\beta_1} \\ p^2 - \eta_{\beta_1}^2 \end{pmatrix} \qquad (2.11)$$

where $\frac{A_3}{B_1}$ is the S to P transmission coefficient, which we use to characterize the J to K conversion of PKJKP at ICB (Fig. 2.7).

2.1.2 P to S conversion, P to P transmission, and P to P reflection from the liquid to the solid discontinuity

This applies to the PKJKP conversion and PKIKP(PKPdf) transmission at the ICB near the source side, PKP transmission at the CMB near the receiver side, and PKiKP

reflection at the ICB (Fig. 2.2). The potentials of P and S waves on the two sides of the boundary can be represented by

$$\phi_1 = A_1 exp[i\omega(px_1 + \eta_{\alpha_1}x_3 - t)]$$
$$+A_2 exp[i\omega(px_1 - \eta_{\alpha_1}x_3 - t)] \tag{2.12}$$
$$\psi_1 = B_3 exp[i\omega(px_1 + \eta_{\beta_2}x_3 - t)] \tag{2.13}$$
$$\phi_2 = A_3 exp[i\omega(px_1 + \eta_{\alpha_2}x_3 - t)] \tag{2.14}$$

where A_1 is the amplitude for the incident P wave, A_2 is the amplitude for the reflected P, A_3 and B_3 are amplitudes for the refracted P and SV waves.

The condition on the continuity of the normal displacement (2.1) gives

$$\eta_{\alpha_1}(A_1 - A_2) = \eta_{\alpha_2}A_3 - pB_3 \tag{2.15}$$

and conditions on the continuity of normal (2.2) and horizontal (2.3) stresses give

$$\lambda_1(p^2 + \eta_{\alpha_1}^2)(A_1 + A_2) = \lambda_2(p^2 + \eta_{\alpha_2}^2)A_3 + 2\mu_2\eta_{\alpha_2}^2 A_3 - 2\mu_2 p\eta_{\beta_2}B_3 \tag{2.16}$$

$$2p\eta_{\alpha_2}A_3 - (p^2 - \eta_{\beta_2^2})B_3 = 0 \tag{2.17}$$

Thus we have the following set of equations

$$\eta_{\alpha_1}\frac{A_2}{A_1} + \eta_{\alpha_2}\frac{A_3}{A_1} - p\frac{B_3}{A_1} = \eta_{\alpha_1}$$
$$\frac{\lambda_1}{\alpha_1^2}\frac{A_2}{A_1} - (\frac{\lambda_2}{\alpha_2^2} + 2\mu_2\eta_{\alpha_2}^2)\frac{A_3}{A_1} + 2\mu_2 p\eta_{\beta_2}\frac{B_3}{A_1} = -\frac{\lambda_1}{\alpha_1^2} \tag{2.18}$$
$$2p\eta_{\alpha_2}\frac{A_3}{A_1} - (p^2 - \eta_{\beta_2}^2)\frac{B_3}{A_1} = 0$$

And solutions are

$$
\begin{pmatrix} \frac{A_2}{A_1} \\ \frac{A_3}{A_1} \\ \frac{B_3}{A_1} \end{pmatrix} = \begin{pmatrix} \eta_{\alpha_1} & \eta_{\alpha_2} & -p \\ \frac{\lambda_1}{\alpha_1^2} & -\frac{\lambda_2}{\alpha_2^2} - 2\mu_2\eta_{\alpha_2}^2 & 2\mu_2 p\eta_{\beta_2} \\ 0 & 2p\eta_{\alpha_2} & -p^2 + \eta_{\beta_2}^2 \end{pmatrix}^{-1} \begin{pmatrix} \eta_{\alpha_1} \\ -\frac{\lambda_1}{\alpha_1^2} \\ 0 \end{pmatrix} \tag{2.19}
$$

where $\frac{B_3}{A_1}$ is the transmission coefficient for the K to J conversion of PKJKP at ICB (Fig. 2.7), $\frac{A_3}{A_1}$ is for the K to I transmission of PKIKP at ICB and the K to P transmission of PKP, and $\frac{A_2}{A_1}$ is the reflection coefficient for PKiKP (Fig. 2.5).

2.1.3 P to P reflection and P to P transmission from the solid to the liquid discontinuity

This applies to the PcP reflection at the CMB and the PKP transmission at the CMB near the source side (Fig. 2.3). The potentials of P and S waves at two sides of the boundary can be represented by

$$
\begin{aligned}
\phi_1 &= A_1 exp[i\omega(px_1 + \eta_{\alpha_1}x_3 - t)] \\
&\quad + A_2 exp[i\omega(px_1 - \eta_{\alpha_1}x_3 - t)] \tag{2.20} \\
\psi_1 &= B_2 exp[i\omega(px_1 - \eta_{\beta_1}x_3 - t)] \tag{2.21} \\
\phi_2 &= A_3 exp[i\omega(px_1 + \eta_{\alpha_2}x_3 - t)] \tag{2.22}
\end{aligned}
$$

where A_1 is the amplitude for the incident P wave, A_2 and B_2 are amplitudes for the reflected P and SV waves, A_3 is amplitude for the refracted P wave.

The condition on the continuity of the normal displacement (2.1) gives

$$\eta_{\alpha_1}(A_1 - A_2) - pB_2 = \eta_{\alpha_2}A_3 \tag{2.23}$$

and conditions on the continuity of normal (2.2) and horizontal

(2.3) stresses give

$$(\frac{\lambda_1}{\alpha_1^2} + 2\mu_1\eta_{\alpha_1}^2)(A_1 + A_2) + 2\mu_1 p\eta_{\beta_1}B_2 = \frac{\lambda_2}{\alpha_2^2}A_3 \tag{2.24}$$

$$2p\eta_{\alpha_1}(A_1 - A_2) - (p^2 - \eta_{\beta_1}^2)B_2 = 0 \tag{2.25}$$

Thus we have the following set of equations

$$
\begin{aligned}
\eta_{\alpha_1}\frac{A_2}{A_1} + p\frac{B_2}{A_1} + \eta_{\alpha_2}\frac{A_3}{A_1} &= \eta_{\alpha_1} \\
(\frac{\lambda_1}{\alpha_1^2} + 2\mu_1\eta_{\alpha_1}^2)\frac{A_2}{A_1} + 2\mu_1 p\eta_{\beta_1}\frac{B_2}{A_1} - \frac{\lambda_2}{\alpha_2^2}\frac{A_3}{A_1} &= -\frac{\lambda_1}{\alpha_1^2} - 2\mu_1\eta_{\alpha_1}^2 \\
-2p\eta_{\alpha_1}\frac{A_2}{A_1} - (p^2 - \eta_{\beta_1}^2)\frac{B_2}{A_1} &= -2p\eta_{\alpha_1}
\end{aligned}
\tag{2.26}
$$

And solutions are

$$
\begin{pmatrix} \frac{A_2}{A_1} \\ \frac{B_2}{A_1} \\ \frac{A_3}{A_1} \end{pmatrix} = \begin{pmatrix} \eta_{\alpha_1} & p & \eta_{\alpha_2} \\ \frac{\lambda_1}{\alpha_1^2} + 2\mu_1\eta_{\alpha_1}^2 & 2\mu_1 p\eta_{\beta_1} & -\frac{\lambda_2}{\alpha_2^2} \\ -2p\eta_{\alpha_1} & -p^2 + \eta_{\beta_1}^2 & 0 \end{pmatrix}^{-1} \begin{pmatrix} \eta_{\alpha_1} \\ -\frac{\lambda_1}{\alpha_1^2} - 2\mu_1\eta_{\alpha_1}^2 \\ -2p\eta_{\alpha_1} \end{pmatrix} \tag{2.27}
$$

where $\frac{A_2}{A_1}$ is the reflection coefficient for PcP at CMB and $\frac{A_3}{A_1}$ is the coefficient of the P to K transmission for PKP at CMB (Fig. 2.4).

2.2 Geometric Spreading

The amplitude of an arrival phase depends not only on the energy partition at various discontinuities but also on the geometric spreading of a tube of rays. The amplitude is inversely proportional to the wavefront area within the tube. The tube may expand or contract due to the velocity heterogeneity accompanied by the amplitude decrease and increase, respectively. But, in general, the wave amplitude decays with respect to the epicentral distance. Referring to the definition of geometric spreading [*Ben-Menahem & Singh*, 1981], we have

$$A(\Delta) = A_0 \sqrt{\frac{v_h tani_h}{a^2 r_h cosi_0}(\frac{\partial p}{\partial \Delta})} \qquad (2.28)$$

where $A(\Delta)$ is the amplitude of a recorded phase in a seismogram, A_0 is the original amplitude when the phase takes off the source, v_h is the velocity at the source, i_h is the take-off angle of the phase, a is the radius of the earth, i_0 is the incident angle of the phase at the station, r_h is the radial distance from the source to the earth's center, p is the phase ray parameter, and Δ is the epicentral distance.

From (2.11), (2.19), (2.27), and (2.28), we may calculate the theoretical amplitude ratio (Chapter 3, 5, and 6) or conduct reflection, transmission, and geometric spreading corrections for the observed amplitude ratios (Chapter 4).

2.3 Direct Solution Method Synthetics

In our studies of PKJKP (Chapter 5 and 6), the synthetic waveform modeling provides us a decisive evidence to confirm our detection of PKJKP. Moreover, it also helps us make the first attempt to constrain shear wave attenuation from body wave observation . As PKJKP is a very weak phase due to the poor phase conversion

and strong attenuation in the inner core, the interference of outer-core, mantle, and crust phases is a serious issue. The number of possible phases is theoretically infinite. However, from observations, we can only identify ~ 100 phases so far, for which the ray paths can be specified. This means that most of the phases are weak and unidentifiable. We usually do not need to consider them in most studies. But, these weak interfering phases may put us in trouble when we discuss the elusive phase PKJKP.

Thus the completeness and accuracy of the synthetics is our primary concern while we are doing the synthetic waveform modeling. All the synthetic methods, which are based on the specification of ray paths, are not appropriate. The Direct Solution Method (DSM) is a well documented technique to generate highly accurate and complete synthetic seismograms ([*Geller & Ohminato*, 1994; *Takeuchi et al.*, 1996]). The method based on the normal mode superposition can also be used to compute complete and accurate synthetics. The difference is that the DSM computation is faster when we have to change the inner core seismic structure (in PREM) very often. Here we will introduce the main theories used in DSM briefly.

2.3.1 Elastic equation of motion in frequency domain

In the time domain, the general elastic equation of motion is

$$\rho \ddot{u}_i + (C_{ijkl} u_{k,l})_{,j} + f_i = 0 \tag{2.29}$$

We may readily rewrite it as

$$\rho \omega^2 u_i + (C_{ijkl} u_{k,l})_{,j} + f_i = 0 \tag{2.30}$$

in the frequency domain. The DSM is exactly based on solving the Galerkin weak form of (2.30).

In the homogeneous isotropic media the equation of motion (2.29) may be expressed as

$$\rho\ddot{\vec{u}} = (\lambda + \mu)\nabla(\nabla \bullet \vec{u}) - (\mu\nabla \times \nabla \times \vec{u}) \qquad (2.31)$$

For an SH wave, it may be further simplified into

$$\rho\ddot{u} = \mu\nabla^2 u \qquad (2.32)$$

This is the well-known wave equation. In a flat layered model, its solution is

$$u_i = A_i exp[i(\omega t - k_x x - k_z z)] \qquad (2.33)$$

Substituting (2.33) into (2.32) yields

$$(\rho\omega^2 - k_x^2\mu)u + \frac{d}{dz}(\mu\frac{du}{dz}) = -f \qquad (2.34)$$

This is the equation of motion in a vertically heterogeneous medium in the frequency domain for the SH wave.

2.3.2 Method of Weighted Residuals

All numerical methods for solving the elastic equation of motion adopt the Method of Weighted Residuals (MWR) (e.g., [*Finlayson*, 1972]). The displacement $\vec{u}$ is expressed as

$$u_i(\vec{x}) = \sum_{n=1}^{N} c_n \phi_i^{(n)}(\vec{x}) \tag{2.35}$$

where c_n are the unknown coefficients, $\phi_i^{(n)}$ are the independent vector trial functions. In general, the displacement expression (2.35) will not satisfy the equation of motion and boundary conditions exactly. The corresponding errors are classified into the domain residuals and the boundary residuals.

According to the residuals, the MWR is further divided into three methods. (1) Domain Residuals Method. Trial functions are chosen to satisfy boundary and continuity (i.e., boundary residuals are zero). So the partial differential equation has residuals. (2) Boundary Residuals Method. Trial functions are chosen to satisfy the partial differential equation (i.e., its residuals are zero). So the boundary conditions have residuals. (3) Mixed Method. The chosen trial functions satisfy neither the boundary conditions nor the partial differential equation. The DSM uses the Domain Residuals Method.

Weights used in MWR are a set of linearly independent vector weight functions $w_i^{(m)}$ $(m = 1, \cdots, N)$. The domain residuals (or boundary residuals) are multiplied by the weight functions, and then integrated to get the weighted residuals. Setting the N weighted residuals to zero gives us a set of simultaneous linear equations for the coefficients c_n in (2.35).

2.3.3   Strong and weak forms of the elastic equation of motion

Based on the domain residual method of MWR, in the general elastic medium, the strong form of the elastic equation of motion is represented by

$$\int_V w_i^{(m)}[\rho\omega^2 u_i + (C_{ijkl}u_{k,l})_{,j} + f_i]dV = 0 \tag{2.36}$$

where $(m = 1, \cdots, N)$. On the other hand, the weak form of the elastic equation of motion is defined as

$$\omega^2 \int_V y_i^{(m)} \rho v_i dV - \int_V y_{i,j}^{(m)} C_{ijkl} v_{k,l} dV = - \int_V y_i^{(m)} f_i dV \tag{2.37}$$

where

$$v_i(\vec{x}) = \sum_{n=1}^{N} d_n \psi_i^{(n)}(\vec{x})$$

It is simple to prove that the strong (2.36) and weak (2.37) forms of the elastic equation of motion are equivalent.

Integrating the second item on the left of (2.37) by parts gives

$$\int_V y_{i,j}^{(m)} C_{ijkl} v_{k,l} dV = \int_S y_i^{(m)} C_{ijkl} v_{k,l} ds - \int_V y_i^{(m)} (C_{ijkl} v_{k,l})_{,j} dV \tag{2.38}$$

Substituting (2.38) into (2.37), we have

$$\int_V y_i^{(m)} [\rho \omega^2 u_i + (C_{ijkl} u_{k,l})_{,j} + f_i] dV - \int_S y_i^{(m)} [C_{ijkl} v_{k,l} n_j] ds = 0 \tag{2.39}$$

Because weight functions $y^{(m)}$ are a complete set, their coefficients in the two integrals should be zero, respectively.

$$\rho \omega^2 u_i + (C_{ijkl} u_{k,l})_{,j} + f_i = 0 \tag{2.40}$$

$$C_{ijkl} v_{k,l} n_j = 0 \tag{2.41}$$

The expression (2.40) is corresponding to the strong form of the elastic equation of

motion and the expression (2.41) is the free surface boundary condition. Therefore, the weak form of the elastic equation of motion in fact combines both the strong form and the boundary condition.

The free surface boundary condition (2.41) is a special case of the natural boundary condition

$$(C_{ijkl}v_{k,l})n_j - S_{ij}v_j = 0 \tag{2.42}$$

where $S_{ij}(i = 1, 2, 3)$ are constants (varying with positions). If considering the natural boundary condition, we may rewrite the weak form (2.37) as

$$\omega^2 \int_V y^{(m)}\rho v_i dV - \int_V y_{i,j}^{(m)}C_{ijkl}v_{k,l}dV + \int_S y_i^{(m)}S_{ij}v_j ds = -\int_v y_i^{(m)}f_i dV \tag{2.43}$$

2.3.4 Direct Solution Method

If taking the weight function $y_i^{(m)}$ in (2.43) as

$$y_i^{(m)} = (\phi_i^{(m)})^* \tag{2.44}$$

and displacement representation v_i in (2.43) as

$$v_i = \sum_{n=1}^N c_n \phi_i^{(n)} \tag{2.45}$$

We may obtain the Galerkin weak form of the elastic equation of motion for a solid medium with arbitrary natural boundary conditions

$$(\omega^2 T - H + R)\vec{c} = -\vec{g} \qquad (2.46)$$

where

$$T_{mn} = \int_V (\phi_i^{(m)})^* \rho \phi_i^{(n)} dV$$

which is mass (kinetic energy) matrix;

$$H_{mn} = \int_V (\phi_{i,j}^{(m)})^* C_{ijkl} \phi_{k,l}^{(n)} dV$$

which is still (potential energy) matrix;

$$R_{mn} = \int_S (\phi_i^{(m)})^* S_{ij} \phi_j^{(n)} dV$$

which is the boundary condition matrix;

$$g_m = \int_V (\phi_i^{(m)})^* f_i dV$$

which is the excitation vector.

In order to improve the accuracy, especially when $\omega \to \omega_m$ (ω_m is the eigenfrequency of the mth mode), *Geller and Takeuchi* (1995) modified T as T', and H as H':

$$T'_{mn} = c_m^* T c_n \qquad (2.47)$$

$$H'_{mn} = c_m^* H c_n \qquad (2.48)$$

where c_m^* is the conjugate of the eigenvector c_m. The DSM currently can be used to calculate very accurate and complete 1-D spherical synthetics by solving the equation (2.46) [*Takeuchi et al.*, 1996].

2.4   Phase Weighted Stacking Method

In our studies of PKJKP (Chapter 5 and 6) we also use an important tool, Power Weighted Stack (PWS) ([*Schimmel & Paulssen*, 1997]), to extract the elusive inner core shear wave phase. The PWS is a recent method developed to reduce the incoherent noise in the seismic array data. Compared to other stacking techniques (e.g., linear stack, *n*th root stack [*Muirhead*, 1968] and semblance stack [*Taner & Koehler*, 1969]), the PWS has a remarkable advantage: it can resolve arrival time and slowness better for the weak and coherent phases.

The PWS measures the coherency by means of the instantaneous phases of the traces in the complex domain. A complex trace $S(t)$ is constructed from the seismic trace $s(t)$:

$$S(t) = s(t) + iH(s(t)) \tag{2.49}$$

where $H(s(t))$ is the Hilbert transform of $s(t)$. We can rewrite (2.49) as

$$S(t) = A(t)exp[i\phi(t)] \tag{2.50}$$

where $A(t)$ is the envelope of $s(t)$ and $\phi(t)$ is the instantaneous phase.

After normalizing each complex trace in the form of (2.50), summing up them together, and calculating the mean, we obtain

$$c(t) = \frac{1}{N}\left|\sum_{k=1}^{N} exp[i\phi(t)]\right| \tag{2.51}$$

where N is the number of traces. This is a phase stack as the amplitudes are normalized. The value of $c(t)$ ranges from 1 to 0. At a certain point, if the instantaneous

phases are very close (e.g., traces are coherent), $c(t)$ approximates to 1; if the phases are incoherent (or even opposite each other), $c(t)$ would be much smaller than 1 and close to 0.

Taking advantage of the property of $c(t)$, the Phases Weighted Stacking method is defined as

$$g(t) = \frac{1}{N} \sum_{j=1}^{N} s_j(t) \left| c(t) \right|^{\nu} = \frac{1}{N} \sum_{j=1}^{N} s_j(t) \left| \frac{1}{N} \sum_{k=1}^{N} exp[i\phi(t)] \right|^{\nu} \tag{2.52}$$

When the power ν is zero, the PWS becomes the linear stack. Thus $|c(t)|^{\nu}$ virtually acts as a weight at every sample. Higher ν means stronger reduction of the noise. Depending on the background noise level, ν is usually chosen in a range of 1 to 5. However, the stacked amplitude of the coherent signals would not be biased too much as $c(t)$ is close to 1. *Schimmel and Paulssen* (1999) demonstrated this point using both synthetic and realistic seismograms in comparison with other stacking methods. We also do the similar background noise experiments in Chapter 6.

Figure 2.1: Rays for an incident SV wave on a solid-fluid interface. The SV wave is reflected as SV and P waves on the solid side, and refracted as P on the fluid side. It applies to the J to K phase conversion of PKJKP at the ICB near the array side (Fig. 2.7).
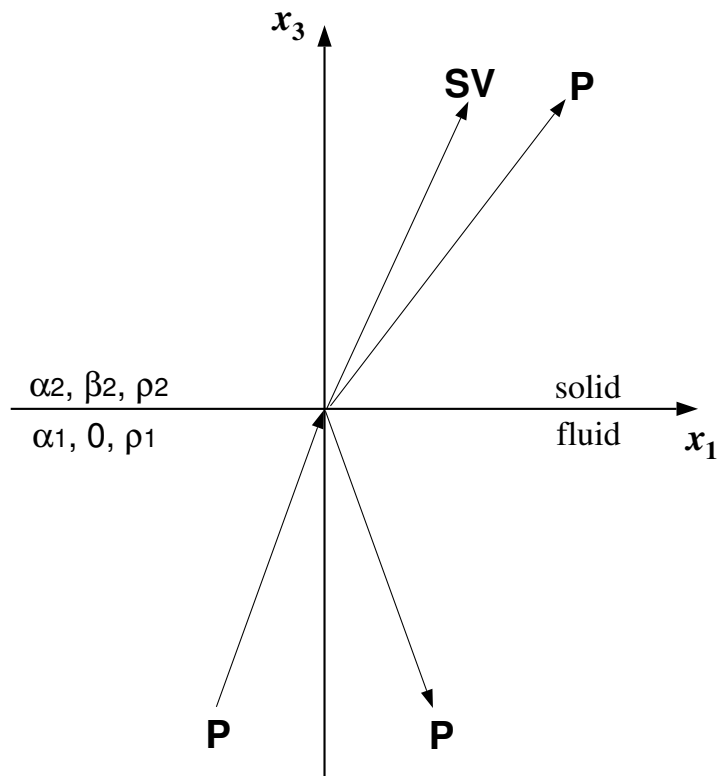
Figure 2.2: Rays for an incident P wave on a fluid-solid interface. The P wave is only reflected as P wave on the fluid side, and refracted as P and SV waves on the solid side. It applies to the K to J phase conversion of PKJKP at the ICB near the source side (Fig. 2.7), K to I phase transmission of PKIKP at the ICB near the source side, K to P phase transmission of PKP at the CMB near the station side, and K to K reflection of PKiKP at the ICB (Fig. 2.4, 2.5, 2.6).
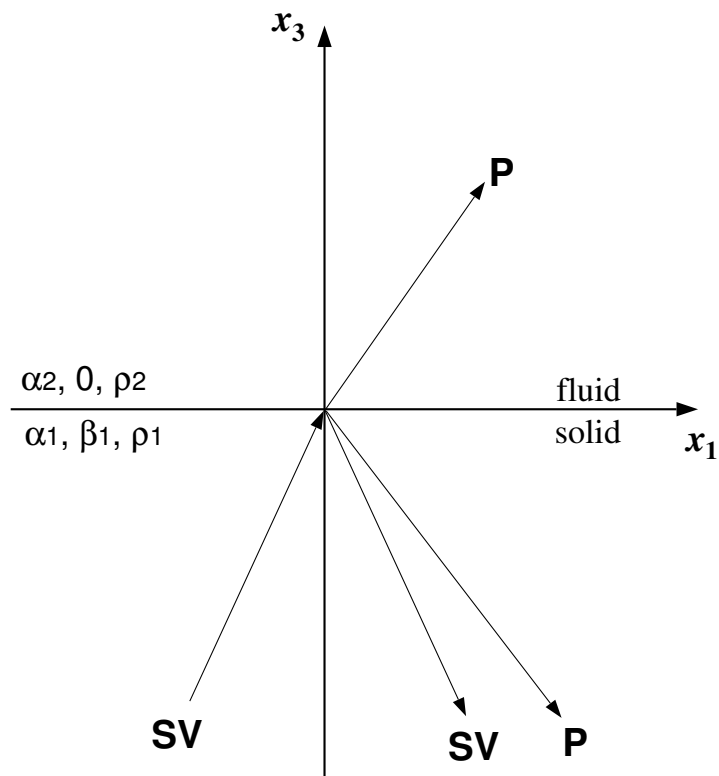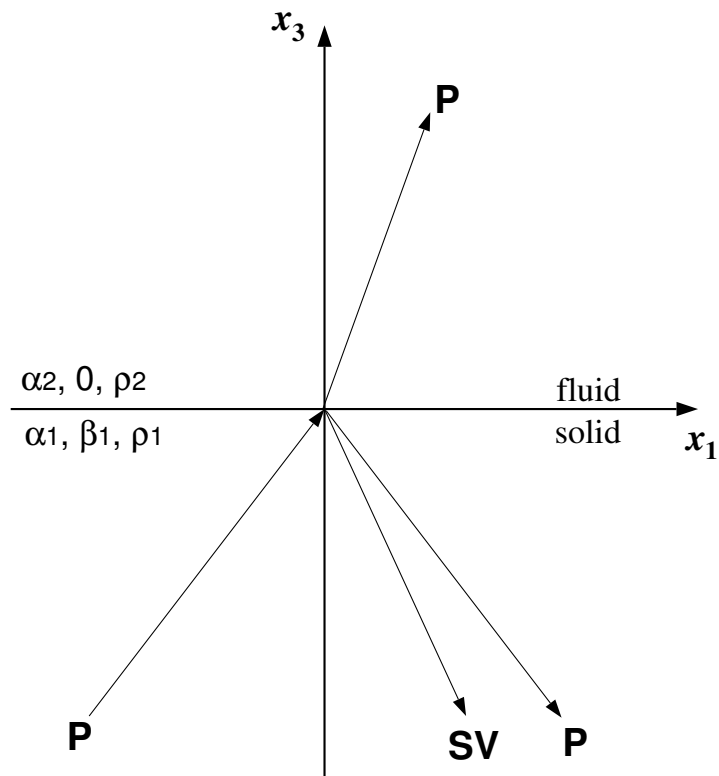
Figure 2.3: Rays for an incident P wave on a solid-fluid interface. The P wave is reflected as P and SV waves on the solid side, and refracted as P wave on the fluid side. It applies to the I to K phase transmission of PKIKP at the ICB near the station side, P to K phase transmission of PKP at the CMB near the source side, and P to P reflection of PcP at the CMB (Fig. 2.4, 2.5).
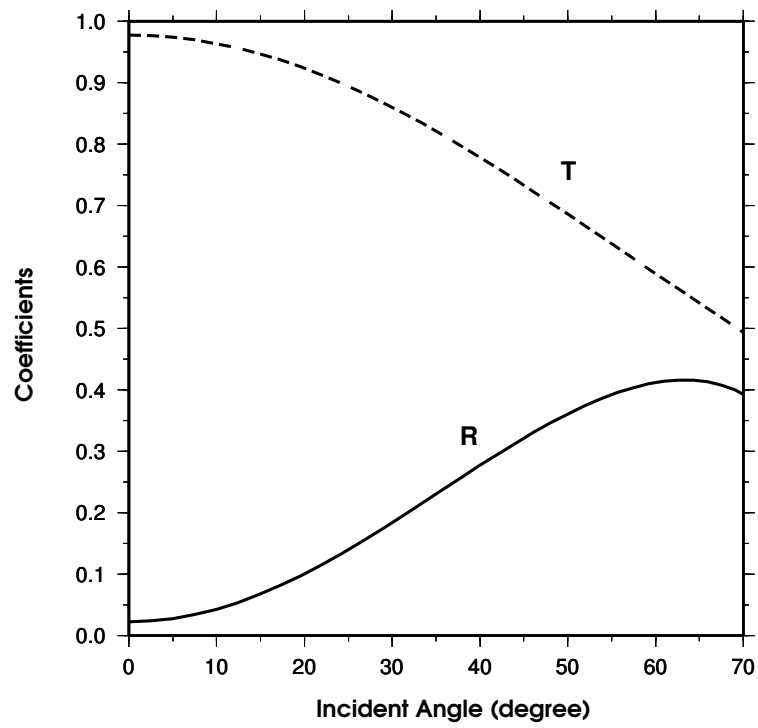
Figure 2.4: Transmission and reflection coefficients at the CMB. The dashed line denotes P to K transimission at the CMB; the solid line denotes reflected P wave (PcP) at the CMB. Coefficients are calculated with reference to PREM [*Dziewonski & Anderson*, 1981] model.
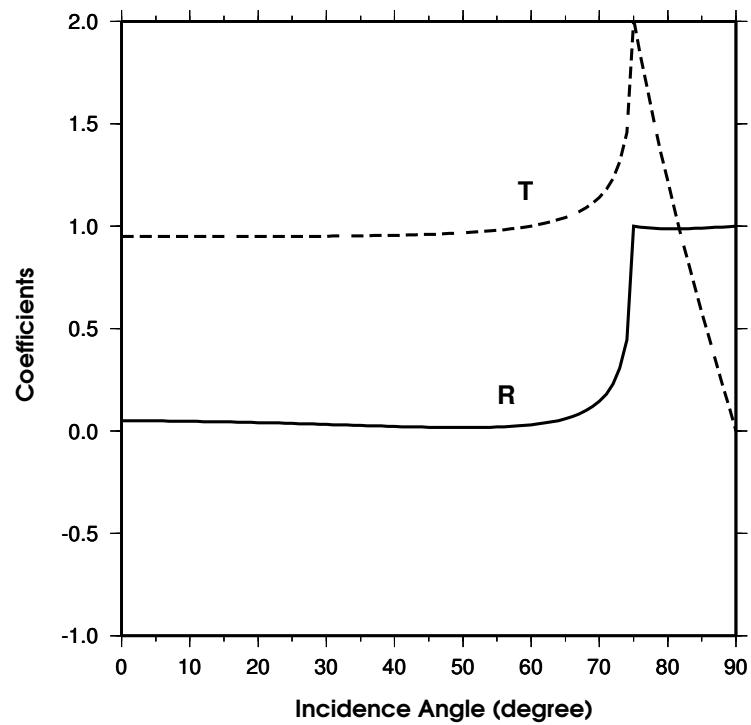
Figure 2.5: Transmission and reflection coefficients at the ICB. The dashed line denotes K to I transimission at the ICB; the solid line denotes reflected K wave (PKiKP) at the ICB. Coefficients are calculated with reference to PREM [*Dziewonski & Anderson*, 1981] model.
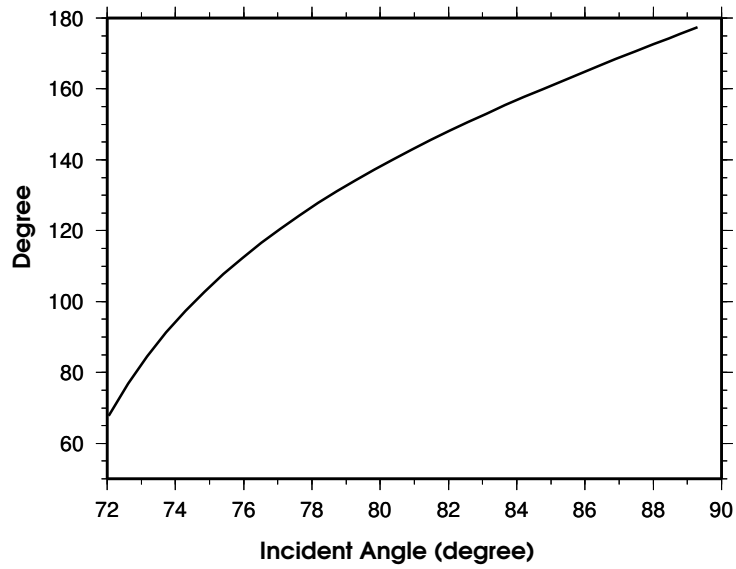
Figure 2.6: Phase shift of PKiKP at the ICB based on PREM model. The phase shift is due to the post-critical reflection of PKiKP at the ICB.
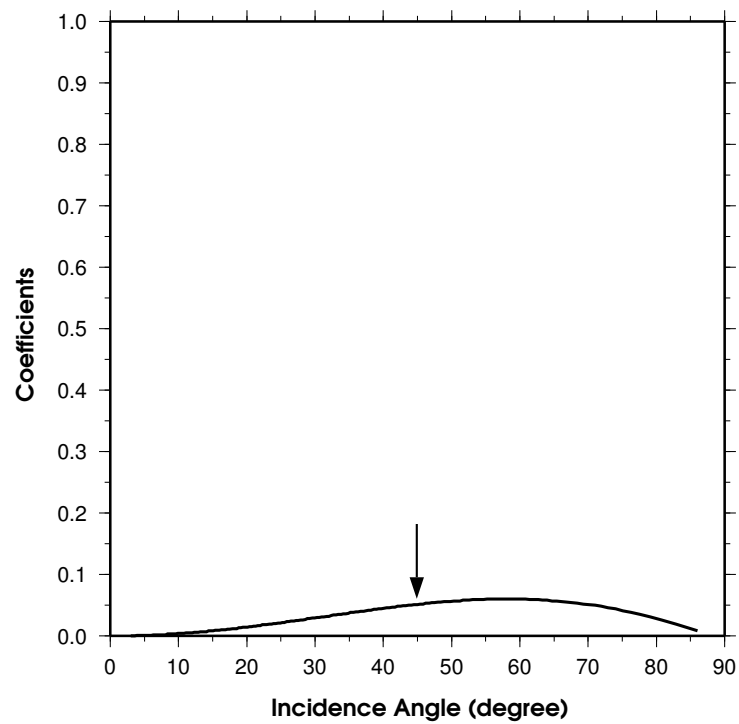
Figure 2.7: Conversion coeffient of PKJKP at the ICB. The curve characterizes the product of the K to J and J to K phase conversion coefficients at ICB. Coefficients are calculated with reference to PREM [*Dziewonski & Anderson*, 1981] model. The arrow marks the incident angle corresponding to our PKJKP study in this dissertaton.

Chapter 3

Density Contrast at ICB

This chapter was published in *Geophysical Journal International* [*Cao & Romanowicz, 2004a*] with the title 'Constraints on Density and Shear Velocity Contrasts at the Inner Core Boundary'

Summary

The density jump ($\Delta\rho_{ICB}$) at the Inner Core Boundary (ICB) is an important constraint on the dynamics and history of the Earth's core. Two types of seismological data sensitive to $\Delta\rho_{ICB}$ have been studied since the 1970's: free oscillation eigenfrequencies and amplitudes of core reflected phases (PKiKP/PcP). The reference PREM model (Dziewonski and Anderson, 1981), based largely on normal mode data, has a relatively low value of $\Delta\rho_{ICB} = 0.60 gcm^{-3}$, whereas most studies based on PKiKP/PcP amplitude ratios find significantly larger values, sometimes in excess of $1.0 gcm^{-3}$. It has been argued that, because PKiKP is rarely observed in the distance range considered ($10 - 70^o$), the latter type of measurement provides only upper

bounds on $\Delta\rho_{ICB}$ (e.g. Shearer and Masters, 1990). We have analyzed 10 years of high quality global broadband data accumulated since the work of Shearer and Masters (1990). We systematically analyzed over 4500 seismograms from intermediate/deep events (depth > 70 km) and nuclear explosions, in the distance range $10 - 70^o$. The data were filtered in the 2-poled Butterworth band-pass 0.7-3 Hz. We performed a rigorous data selection and identified 5 pairs of very clear (Quality A), and 15 possible (Quality A^-) PKiKP and PcP arrivals. In addition, 58 records showed no PKiKP but a clear PcP. Together, we obtain a much less dispersed dataset than previously available, with the quality A data at the lower end of the ensemble of amplitude ratios versus distance. We combine our high quality measurements with 2 measurements from the literature that fall within our rigorous selection criteria and obtain estimates of $\Delta\rho_{ICB}$ in the range $0.6 - 0.9 gcm^{-3}$ and $\Delta\beta_{ICB}$ in the range $2 - 3kms^{-1}$. Our estimate of $\Delta\rho_{ICB}$ is in agreement with a recent reevaluation of normal mode data (Masters and Gubbins, 2003), thus reconciling results from body wave and mode studies and providing a tighter constraint on $\Delta\rho_{ICB}$ for geodynamicists. Our study also provides evidence for a shear velocity gradient at the top of the inner core.

3.1   Introduction

The density $\Delta\rho_{ICB}$ and shear velocity $\Delta\beta_{ICB}$ contrasts at the Inner Core Boundary (ICB), estimated using seismological methods, are important constraints for the understanding of the character of the Earth's geodynamo and the evolution of the inner core (e.g. [*Hewitt et al.*, 1975; *Gubbins*, 1977; *Buffett et al.*, 1996; *Stacey & Stacey*, 1999])

So far, three distinct approaches have been used to constrain the density and shear velocity contrasts at the ICB, but the resulting estimates vary significantly. The first method uses data for normal modes which are sensitive to the inner core structure

[*Dziewonski & Gilbert*, 1971; *Gilbert et al.*, 1973; *Gilbert & Dziewonski*, 1975; *Masters*, 1979]. The reference PREM model [*Dziewonski & Anderson*, 1981], which incorporates constraints from normal mode data, has $\Delta\rho_{ICB} = 0.60 gcm^{-3}$ and $\Delta\beta_{ICB} = 3.5 kms^{-1}$.

The second method uses body wave amplitude and waveform modeling of PKP and PKiKP. This technique has resulted in estimates of $\Delta\rho_{ICB} \sim 0 - 1.2 gcm^{-3}$ [*Hage*, 1983] and $\Delta\beta_{ICB}$ ranging from $\sim 0 kms^{-1}$ [*Choy & Cormier*, 1983], to $2.5 - 3.0 kms^{-1}$ [*Hage*, 1983], or $2 - 4 kms^{-1}$ [Cummins & Johnson, 1988].

The third method is based on measurements of $PKiKP/PcP$ amplitude ratios in the distance range 10° to 70°. The first convincing observation of PKiKP in this distance range was reported by *Engdahl et al.* [1970] and was based on stacking of LASA array data. *Bolt and Qamar* [1970] first proposed the amplitude ratio technique and estimated a maximum density jump of 1.8 gcm^{-3} at the ICB. *Souriau and Souriau* [1989] further constrained the density jump to be in the range of 1.35-1.6 gcm^{-3} based on array data. Finally, *Shearer and Masters* [1990] estimated maximum bounds on PKiKP/PcP ratios and obtained $\Delta\rho_{ICB} < 1.0 gcm^{-3}$ and $\Delta\beta_{ICB} > 2.5 kms^{-1}$.

Compared with the results derived from normal modes, the constraint on the density contrast from body waves is considered to be much less robust, as it is based on few reliable measurements, and most recently, a set of rather scattered "upper bound" data [*Shearer & Masters*, 1990]. Indeed, PKiKP is such a weak phase in the distance range from 10° to 70° that it is rarely observed, and even more rarely so, without stacking. *Shearer and Masters* [1990] systematically searched for PKiKP arrivals in over 4900 GDSN vertical component seismograms. They found only two seismograms with both clear PKiKP and clear PcP arrivals. Both *Souriau and Souriau* [1989] and *Shearer and Masters* [1990] used "non-observations" of PKiKP as upper bounds on the observed amplitude of this phase, leading to upper bounds on the corresponding PKiKP/PcP amplitude ratios.

At present, geodynamo simulations usually refer to the density contrast derived from

normal mode data. Nevertheless, a recent geodynamo study [*Stacey & Stacey*, 1999] explicitly pointed out that the inner core would not have existed 2 billion years ago if the density contrast at the ICB was as low as inferred from current seismological models. This is obviously against the paleomagnetic evidence, which shows that the Earth has sustained a magnetic field for at least 3 billion years [*McElhinny & Senanayake*, 1980].

In this study, we take advantage of the accumulation of large quantities of high quality global broadband seismic data in the last 15 years, to revisit the question of estimating the density and shear velocity contrasts at the ICB using PKiKP/PcP amplitude ratios.

3.2   Data, Method, and Results

All of the broadband vertical component data for deeper ($\geq 70km$) natural earthquakes and nuclear explosions in the distance range 10° to 70°, for the time span 1990-1999, were systematically downloaded from IRIS Data Management Center (DMC), to search for simultaneous observations of PKiKP and PcP. The ray paths of these phases for a given source-station pair are shown in Fig. 3.1. The seismograms were filtered in the 2-poled Butterworth band-pass 0.7-3 Hz (the dominant frequency of PKiKP is typically ~ 1 Hz). We used relocated origin time and hypocentral parameters from the catalog of *Engdahl et al.* [1998], recently extended to include the year 1999. We then marked the seismograms with the theoretical arrival times of 11 phases (PcP, PKiKP as well as P, pP, sP, PP, PPP, S, sS, SS, and ScS) computed with respect to model $AK135$ [*Kennett et al.*, 1995], and corrected for ellipticity [*Dziewonski & Gilbert*, 1976]. Those 9 phases are the most likely ones to interfere with our target PcP and PKiKP phases. Finally only the seismograms were kept whose background noise before the direct P wave was significantly less than the average amplitude level in the vicinity of the theoretical PKiKP arrival.

We divided the resulting 79 seismograms (out of an initial collection of more than 4500) into three categories (A, A^-, B), according to the following criteria. Quality A data exhibit very clear PKiKP and PcP phases within 5 seconds of their expected theoretical arrivals, there is no other theoretical arrival 15 seconds preceding or following the identified PKiKP or PcP phases (unless the potential interfering arrival can be verified from a nodal plane inspection), and the average peak-to-peak noise-to-signal ratio is less than 40%. Quality A^- includes seismograms with clear PKiKP and PcP phases within 5 seconds of their theoretical arrivals, there is no other theoretical arrival 15 seconds preceding or following the identified PKiKP or PcP, but the average peak-to-peak noise-to-signal ratio is larger than 40%. Finally, in Quality B, we collected seismograms with no observable PKiKP phase within 5 seconds of its theoretical arrival, but there is also no other predicted arrival 50 seconds preceding and 10 seconds following the theoretical PKiKP arrival, and the PcP phase is very clear and within 5 seconds of its predicted arrival.

Based on the above criteria, we collected 5, 15, and 59 Quality A, A^-, and B data, respectively. All of our Quality A data are shown in Fig. 3.2. We measured peak-to-peak amplitudes of the identified PKiKP and PcP phases and computed PKiKP/PcP amplitude ratios for Quality A and Quality A^- data. For Quality B data, the maximum peak-to-peak amplitude 5 seconds around the PKiKP theoretical arrival was used as an upper limit for the PKiKP amplitude (e.g. [*Shearer & Masters*, 1990]) In the epicentral distance range considered, for Quality A data, the difference in take-off angles between PKiKP and PcP is small (approximately from 2.3^o to 11.9^o) and the two rays are close to the maxima of the radiation lobes, as we have verified (Fig. 3.2), Therefore, the effect of the radiation pattern at the source is neglected (e.g. [*Souriau & Souriau*, 1989]).

Additionally, we also applied our selection criteria to re-examine available seismograms from the literature. *Shearer and Masters* [1990] identified only two seismograms with clear simultaneous PKiKP and PcP observations. The theoretical SS arrival is only 1.97 seconds in front of the theoretical PKiKP arrival for the first seismogram.

Table 3.1: Comparison of seismic contrasts at ICB and CMB

Models	$\Delta\alpha_{ICB}$	$\Delta\alpha_{CMB}$	$\Delta\beta_{ICB}$	$\Delta\beta_{CMB}$	$\Delta\rho_{ICB}$	$\Delta\rho_{CMB}$
PREM	0.67	5.65	3.50	7.26	0.60	4.34
PREM2	0.78	5.45	3.50	7.26	0.60	4.34
IASP91	0.83	5.68	3.44	7.30	0.56	4.36
AK135	0.75	5.66	3.50	7.28	0.56	4.36

* units of velocity and density contrasts are kms^{-1} and gcm^{-3}, respectively

For their second seismogram, a theoretical SS arrival is 13.38 seconds in front of the theoretical PKiKP arrival with reference to model $AK135$. Hence it is possible that the discrepancy in the corresponding PKiKP/PcP amplitude ratios (almost a factor of 3) is due to interference with SS in the first example, even though the corresponding epicentral distances are almost the same (39.8^o and 39.2^o, respectively). We included the second of these two measurements, which, according to our criteria, is much more reliable, in our Quality A dataset. We also included one stacking measurement $(0.032, \Delta = 51.4^o)$ [*Schweitzer*, 1992], which has recently been re-measured $(0.038 - 0.048)$ by the author himself (Schweitzer, personal communication, 2003).

We then compared our PKiKP/PcP amplitude ratio measurements to theoretical predictions using several reference models: PREM [*Dziewonski & Anderson*, 1981] , PREM2 [*Song & Helmberger*, 1995], IASP91 [*Kennett & Engdahl*, 1991], and AK135 [*Kennett et al.*, 1995]. Models differ by the velocity contrasts and density contrasts at the ICB and CMB (Table 3.1).

In order to obtain the theoretical PKiKP/PcP amplitude ratio, we calculated transmission and reflection coefficients at various seismic discontinuities as well as ratios of PKiKP and PcP geometrical spreading factors, which may be readily expressed as functions of ray parameters and their corresponding derivatives [*Bolt & Qamar*, 1970]. As for the attenuation factor, we neglected its effect on the predicted ratios in the mantle due to the arguably close ray paths of PKiKP/PcP there, and we assumed that the quality factor in the outer core is infinite because there is no significant change when using a realistic quality factor ($\geq 10,000$) [*Cormier & Richards*, 1976].

As previous authors, we also neglected finite frequency effects, as these are likely within the uncertainties of other factors such as the earth models used, in particular, a possible topography of the CMB. When we explored different models, the computed geometrical spreading factors were very close, but reflection coefficients varied significantly. For each of the models, we searched for the best variance reduction in the parameter space $(\Delta\rho_{ICB}, \Delta\beta_{ICB})$. We note that the set of Quality A measurements spans the entire epicentral distance range considered (Fig. 3.4), thus providing relatively tight fits on the resulting ICB parameters: $\Delta\beta_{ICB}$ is constrained at large distance $(\Delta > 50^o)$ whereas $\Delta\rho_{ICB}$ is constrained by data at shorter distance. The best fitting density contrasts at the ICB vary somewhat from one model to the other, as illustrated in Fig. 3.3: from $\sim 0.6 gcm^{-3}$ (IASP91) to $\sim 0.9 gcm^{-3}$ (PREM2). On the other hand, the range of the best fitting shear velocity contrasts is somewhat tighter: from $\sim 2.4 kms^{-1}$ to $\sim 2.6 km^{-1}$. In fact, because the shear velocity and density contrasts at the CMB are very consistent in each model, the uncertainty in $\Delta\rho_{ICB}$ and $\Delta\beta_{ICB}$ stems mostly from the difference in $\Delta\alpha_{ICB}$ and $\Delta\alpha_{CMB}$ for the different models. In particular, the results for IASP91 show the lowest $\Delta\rho_{ICB}$ because its $\Delta\alpha_{ICB}$ is significantly larger $(> 6\%)$ than for the other models.

3.3   Discussion

In our study, we have identified 7 definite PKiKP arrivals and 15 probable ones, but compared with the huge initial data pool, the percentage of observations is still quite small. It has been argued that PKiKP is observable only when it is anomalously large, probably due to focusing from heterogeneities within the Earth, and even the PKiKP/PcP data measured from the identified PKiKP arrivals represent only upper limits for this ratio (Souriau and Souriau, 1989; Shearer and Masters, 1990). However, when we compare our A, A^- and B quality measurements (Fig. 3.4), we note the following: 1) the data are overall much less scattered than in previous studies; 2) the A quality measurements generally fall near the lower bound of all our measure-

ments, including those found in the literature and corresponding to explicit reports of PKiKP observations. We thus believe that, although the PKiKP arrival is generally weak, our Quality A observations are not significantly biased either by interfering phases (we ruled those out) or focusing effects, and that they simply correspond to favorable geometry with respect to the maximum in P radiation pattern, as we have checked. On the other hand, some of our A^- measurements plot above the best fitting theoretical curves computed using only the quality A data, which indicates that, for these measurements, there may be some constructive interference between noise and PKiKP. We did not use these data in computing the optimal ICB parameters, but we find that they are compatible with the resulting predictions, as are our Quality B data (Fig. 3.4).

On the other hand, we did not include other data from the literature for which seismograms were not available for verification (we show them as open symbols in Fig. 3.4). In particular, several previous measurements used stacking of traces (e.g. [*Bolt & Qamar*, 1970; *Souriau & Souriau*, 1989]). The stacking technique is very effective in extracting the weak seismic signal, but it seems difficult to keep the amplitudes of PKiKP and PcP arrivals from being distorted in the summation (especially when using a nonlinear stacking process).

The density contrast inferred at the ICB depends on the reference seismic models (Fig. 3.3). The main reason is that the reflection coefficients of PcP at the CMB and PKiKP at the ICB also depend on the corresponding P-wave velocity contrasts. In general, the larger $\Delta\alpha_{ICB}$, the lower $\Delta\rho_{ICB}$, for a fixed $\Delta\alpha_{CMB}$; the larger $\Delta\alpha_{CMB}$, the lower $\Delta\rho_{ICB}$, for a fixed $\Delta\alpha_{ICB}$. Further refinement of $\Delta\rho_{ICB}$ will depend on the improvement of our knowledge of P-wave velocity structure at both ICB and CMB. In the four reference seismic models, PREM [*Dziewonski & Anderson*, 1981] and IASP91 [*Kennett & Engdahl*, 1991] are based on absolute travel times from the International Seismological Center (ISC) and free oscillation eigenfrequencies. PREM2 [*Song & Helmberger*, 1995] is modified from PREM by fitting PKP differential travel times, amplitude ratios, and waveforms, but shear velocity and density structure in PREM

are left untouched. AK135 [*Kennett et al.*, 1995] is updated from IASP91 by the authors themselves taking additional account of PKP differential travel times and event relocations. The differences in velocity between AK135 and IASP91 are generally very small except for the reduced velocity gradients at the ICB in AK135. From our experience [*Tkalucic et al.*, 2002] AK135 gives better fits to PKP travel time data than PREM and IASP91. We are therefore inclined to favor the bounds obtained from AK135. The main difference between PREM and IASP91 is in the $\Delta\alpha_{ICB}$; and the main difference between PREM2 and AK135 is in $\Delta\alpha_{CMB}$ (Table 3.1). We note from Fig. 3 and 4 that the PREM $\Delta\rho_{ICB} = 0.6 gcm^{-3}$ is clearly a minimum value compatible with the data, and that $\Delta\rho \approx 0.85 gcm^{-3}$ is optimal.

Compared with the constraint on $\Delta\rho_{ICB}$, the constraint on $\Delta\beta_{ICB}$ (2-3 kms^{-1}) is almost independent of the seismic models. While compatible with the results of other body wave studies, this well-constrained value is significantly lower than the average shear velocity contrast ($\sim 3.5 km^{-1}$) estimated from normal mode data. It is constrained by the trend in PKiKP/PcP amplitude ratios at distances $\Delta > 50^o$ (Fig. 3.4). This may provide further evidence for the existence of a shear velocity gradient at the top of the inner core (e.g. [*Choy & Cormier*, 1983; *Hage*, 1983; Cummins & Johnson, 1988]. Indeed, normal mode data provide an estimate averaged over tens of km of depth, whereas the reflected wave data considered here provide a much more local estimate.

In the quality A observations, which we used to constrain density and shear velocity contrasts at the ICB, all of the corresponding focal depths of the natural events are deeper than 100 km. The usually shorter source time functions than those of shallow ($< 70km$) events (with equivalent magnitudes) enhance the sharpness and signal-to-noise ratio of the phase arrivals. This beneficial feature may significantly help us to uniquely identify the weak PKiKP arrivals. Although our strict selection criteria have limited the global coverage of our observations, the quality A data span a wide geographical distribution (Fig. 3.5). The PKiKP (PcP) bouncing points at the ICB (also CMB) are located beneath Western Pacific Ocean, Australia, Southeastern Asia,

Middle Asia, Eastern Europe, and South America.

3.4 Conclusion

We have obtained a set of high quality PKiKP and PcP observations in the distance range 10° to 70° that provide tighter constraints on the density and shear velocity contrasts at the ICB. The identification of arguably unbiased PKiKP and PcP arrivals greatly improve the body wave constraints on the density and shear velocity contrasts at the ICB. Our preferred value for $\Delta\rho_{ICB}$ is $\sim 0.85 gcm^{-3}$, with some uncertainties remaining, primarily due to uncertainties in the P-wave velocity contrast at the ICB. Our estimates are compatible with a recent reevaluation $(0.64 - 1.0 gcm^{-3})$ of normal mode data [*Masters & Gubbins*, 2003], thus reconciling previously incompatible results from normal mode and body wave measurements. On the other hand, the shear velocity contrast at the ICB is somewhat lower than the average shear velocity in the inner core as obtained from normal mode data. Our study thus provides evidence for 1) a larger density contrast at the ICB than generally assumed in dynamo studies and 2) the existence of a gradient of structure at the top of the inner core. The former is of significance for studies of the geodynamo, whose energy is proportional to the assumed density contrast (Stacey and Stacey, 1999). The inferred gradient may also provide constraints on the cooling and solidifying processes in the inner core and may be of significance in studies of the geodynamo, as well as of the chemical and physical evolution of the inner core [*Gubbins*, 1977; *Loper*, 1978; *Loper*, 1991; *Gubbins et al.*, 1979].
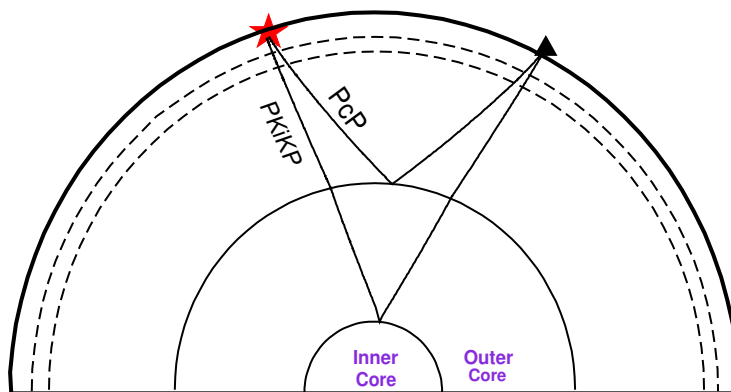
Figure 3.1: Ray paths of PKiKP (reflected P wave from the ICB) and PcP (reflected P wave from the CMB). The star denotes an assumed source and the triangle denotes a seismological station.
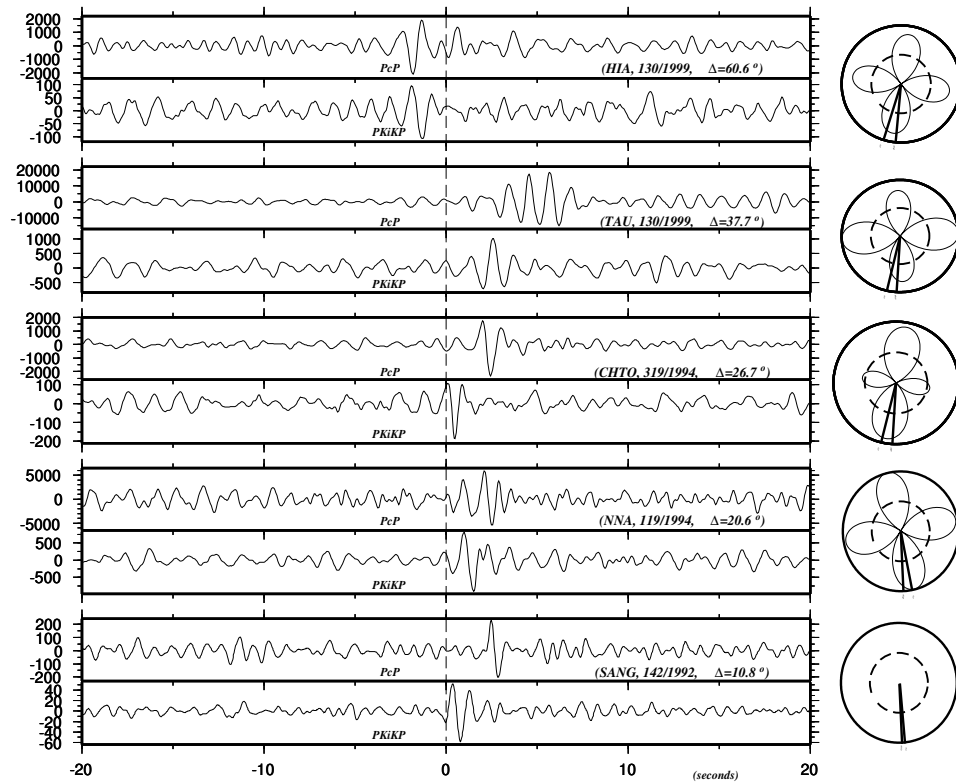
Figure 3.2: Quality *A* observations with very clear PKiKP and PcP phases. Dashed lines are the theoretical arrival times referring to AK135 seismic model, taking into account ellipticity corrections. From top to bottom, the observed PKiKP/PcP amplitude ratios are 0.052, 0.052, 0.071, 0.151, and 0.250, respectively. At right of each pair of traces are the corresponding P-wave radiation patterns derived from the Harvard CMT moment tensors. From top to bottom the differential take-off angles between PKiKP and PcP are approximately 11.9^o, 9.6^o, 10.0^o, 8.6^o, and 2.3^o, respectively. The last observation (SANG) corresponds to a nuclear explosion event.
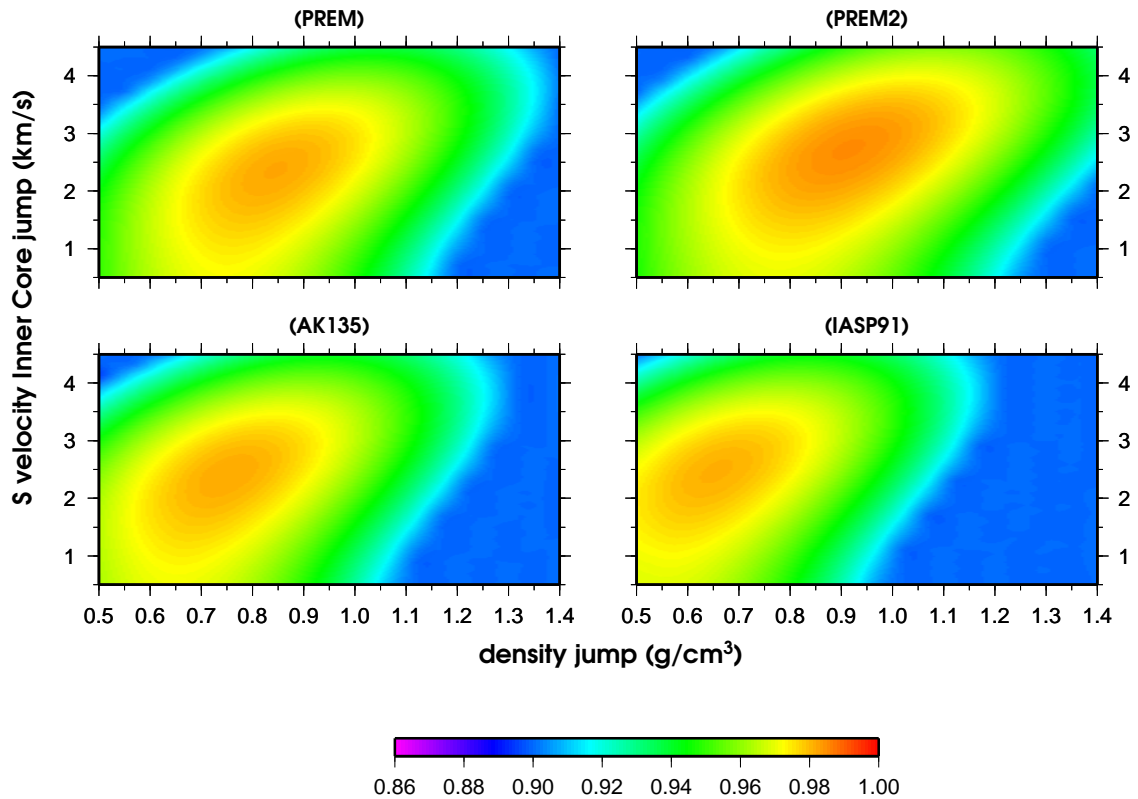
Figure 3.3: Variance reduction with respect to PREM [*Dziewonski & Anderson*, 1981], PREM2 [*Song & Helmberger*, 1995], IASP91 [*Kennett & Engdahl*, 1991], and AK135 [*Kennett et al.*, 1995]. The best fitting $\Delta\rho_{ICB}$ and $\Delta\beta_{ICB}$ are $\sim 0.85 gcm^{-3}$ and $\sim 2.5 kms^{-1}$, $\sim 0.91 gcm^{-3}$ and $\sim 2.6 kms^{-1}$, $\sim 0.65 gcm^{-3}$ and $\sim 2.5 kms^{-1}$, and $\sim 0.75 gcm^{-3}$ and $\sim 2.4 kms^{-1}$, respectively.
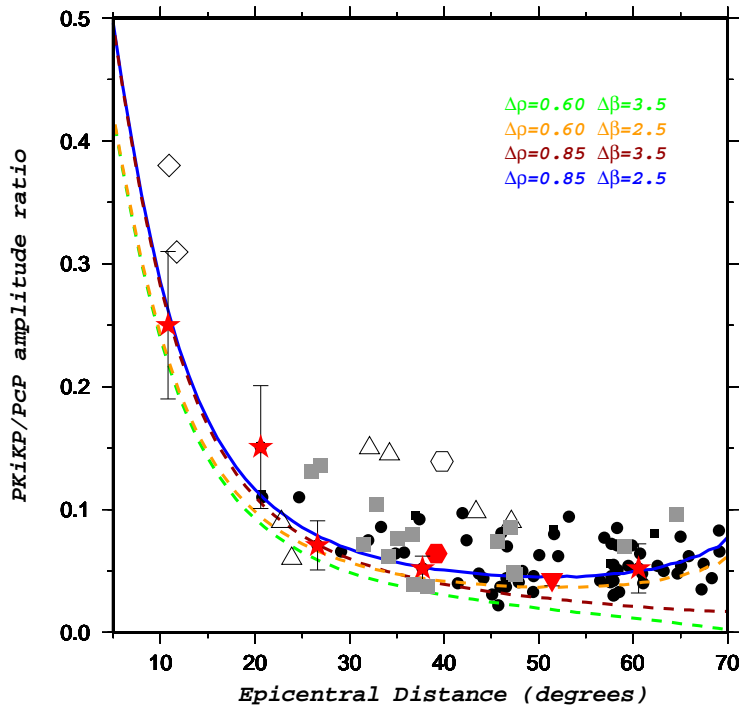
Figure 3.4: Measurements of PKiKP/PcP amplitude ratios. The red stars denote the Quality A data, and their error bars are derived from the fractional ratios of the average peak-to-peak amplitudes of background noise to the peak-to-peak amplitude of the identified phase arrivals; the red hexagon is *Shearer and Masters'* [1990] second measurement with clear PKiKP; the inverted red triangle is a stacking measurement [*Schweitzer*, 1992] which has been remeasured by the author himself recently; the grey squares denote the Quality A^- data; and the black dots are the Quality B data. The curves are the theoretical PKiKP/PcP amplitude ratio calculated with respect to PREM model. For the dashed green curve $\Delta\rho_{ICB} = 0.60gcm^{-3}$ and $\Delta\beta_{ICB} = 3.5kms^{-1}$ (original values in PREM model); for the dashed orange curve $\Delta\rho_{ICB} = 0.60gcm^{-3}$ and $\Delta\beta_{ICB} = 2.5kms^{-1}$; for the dashed red curve $\Delta\rho_{ICB} = 0.85gcm^{-3}$ and $\Delta\beta_{ICB} = 3.5kms^{-1}$; and for the solid blue curve $\Delta\rho_{ICB} = 0.85gcm^{-3}$ and $\Delta\beta_{ICB} = 2.5kms^{-1}$ (our best fitting values using PREM model). The open symbols are other data from previous studies, which were not used in our analysis (triangles: [*Souriau & Souriau*, 1989]; hexagon: [*Shearer & Masters*, 1990]; diamonds: [*Engdahl et al.*, 1970]; [*Bolt & Qamar*, 1970].
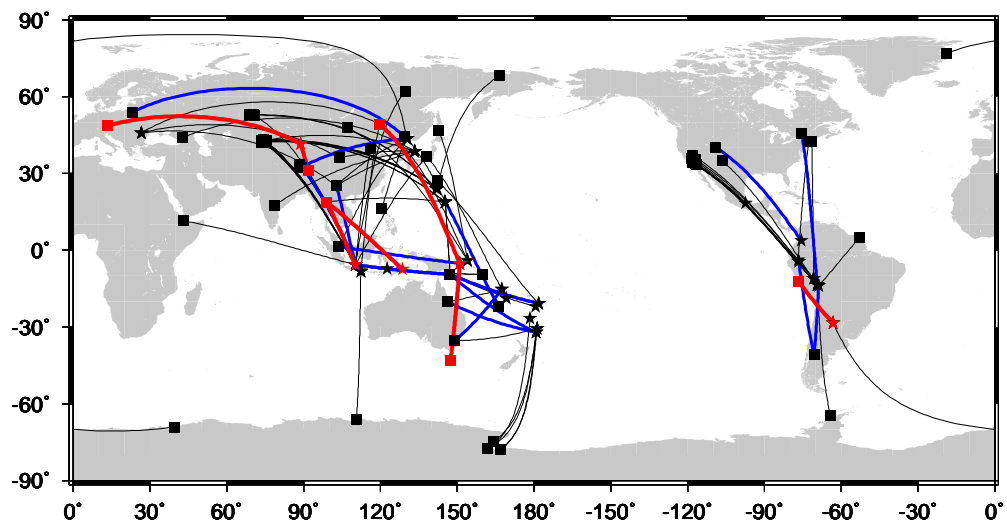
Figure 3.5: Geographical distribution of PKiKP and PcP ray paths. The red, blue, and black lines correspond to Quality A, A^-, and B subsets of data, respectively. The stars denote the events and the squares denote the stations.

Chapter 4

Attenuation Transition at the Top of the Inner Core

This chapter was published in *Earth and Planetary Science Letters* [*Cao & Romanowicz*, 2004b] with the title 'Hemispherical Transition of Seismic Attenuation at the Top of the Earth's Inner Core'

Summary

In contrast to the liquid outer core, the earth's inner core is mostly solid, and its composition is more pure iron. Based on dynamic arguments related to the freezing process of the inner core, and the observation of much lower P wave quality factor in the inner core ($Q_\alpha < 450$), than in the outer core ($Q_\alpha > 10,000$), it has been suggested that a mushy layer with liquid inclusions may exist at the top of the inner core. On the other hand, seismic measurements indicate that Q_α increases towards

the center of the inner core. We here present estimates of Q_α in the depth range 32-110 km beneath the Inner Core Boundary (ICB), based on the measurement of PKIKP/PKiKP amplitude ratios after a narrow band-pass filtering (0.7-2.0 Hz). Our measurements indicate that there are pronounced hemispherical differences in the values of Q_α ($\sim$ 335 and $\sim$ 160 in the western (180^oW to 40^oE) and eastern (40^oE to 180^oE) hemispheres, respectively), and in the depth of transition from decreasing to increasing Q_α ($<$ 32 km beneath the ICB in the eastern hemisphere and $\sim$ 85 km in the western hemisphere). Below 85 km, the hemispherical pattern disappears. We also confirm the existence of a correlated hemispherical pattern in P velocity down to 85 km. The P velocity and Q_α variations are compatible with an interpretation in terms of small hemispherical variations of temperature at the top of the inner core and their influence on the morphology of porosity and connectivity of liquid inclusions in the mushy zone. The disappearance of the differences in Q_α beneath 85 km provide constraints on the likely depth extent of the mushy zone.

4.1   Introduction

The Earth's inner core is formed by a freezing process of iron as the liquid outer core gradually cools [*Jacobs*, 1953; *Stacey*, 1980]. Because the outer core material is not pure iron [*Braginsky*, 1963; *Birch*, 1964], some of the light elements are excluded from the inner core during this dynamic process, to power the geodynamo [*Braginsky*, 1963; *Gubbins*, 1977; *Loper*, 1978; *Gubbins et al.*, 2003], while the residual is likely kept within a mushy layer at the top of the inner core [*Fearn et al.*, 1981; *Loper & Fearn*, 1983; *Sumita et al.*, 1996; *Singh et al.*, 2000]. Thus, constraining the characteristics of the mushy layer at the top of the inner core, as revealed by seismic velocity and attenuation measurements, should give us important insights into the dynamics of the Earth's core.

Since the existence of seismic anisotropy in the inner core was first suggested [*Morelli*

et al., 1986; *Woodhouse et al.*, 1986], its proposed structure has become more complicated and more controversial. The P-wave velocity anisotropy could vary with depth [*Vinnik et al.*, 1994; *Song*, 1996; McSweeney et al., 1997]; in the 100-400 km depth range, there may be a very weakly anisotropic quasi-eastern hemisphere and an anisotropic quasi-western hemisphere for P-wave velocity [*Tanaka & Hamaguchi*, 1997; *Creager*, 1999] and attenuation [*Souriau & Romanowicz*, 1996; *Oreshin & Vinnik*, 2004]; at the top 80 km of the inner core, there may be an isotropic layer characterized by faster P-wave velocity in the quasi-eastern hemisphere than in the quasi-western hemisphere [*Niu & Wen*, 2001; *Garcia*, 2002; *Wen & Niu*, 2002]. However, *Romanowicz et al.* [2002] and *Ishii et al.* [2002] questioned the above complexity. *Ishii et al.* [2002] suggested that there might be no an isotropic layer at the top of the inner core and that constant anisotropy in the whole of the inner core may explain the bulk of the data. *Bréger et al.* [2000] and *Romanowicz et al.* [2002] suggested that the complex lateral variations of P-wave velocity could be due to structure elsewhere in the earth.

The outer core Q_α is usually regarded as infinite ($\geq 10,000$) [*Cormier & Richards*, 1976], but the estimated Q_α in the inner core is constrained to be less than 450 [*Dziewonski & Anderson*, 1981; it Bhattacharyya et al., 1993]. This huge contrast indicates that a zone of decreasing Q_α with depth must exist beneath the ICB [*Loper & Fearn*, 1983]. However, this zone of decreasing Q_α should be confined to the top of the inner core, because multiple seismic observations confirm that Q_α increases with depth below a depth of approximately 100 km beneath the ICB [*Song & Helmberger*, 1995; *Souriau & Roudil*, 1995; *Li & Cormier*, 2002; *Singh et al.*, 2000]. Therefore, the existence of a transition zone at the top of the inner core, where Q_α turns from decreasing to increasing with depth, seems likely.

In order to study the seismic structure at the top of the inner core, the most suitable body wave phases are PKIKP and PKiKP in the epicentral distance range from 120° to 144° (Fig. 4.1). In this distance range, PKIKP samples the top 0-110 km of the inner core and PKiKP is reflected from ICB. The two phases have almost the

same ray paths in the mantle and very close ray paths in the outer core. Hence the assumption that they experience almost the same heterogeneities in the mantle and outer core is valid in a first approximation [*Cormier & Choy*, 1986; *Niu & Wen*, 2001; *Garcia*, 2002; *Wen & Niu*, 2002]. The differences in travel times and amplitudes can therefore be attributed to the vicinity of the ICB.

Unfortunately, these two phases present a great challenge. The separation of PKIKP and PKiKP is very small. For example, it is less than 1.3 seconds when the epicentral distance is less than 135° (when referred to the seismic reference model PREM [*Dziewonski & Anderson*, 1981] (Fig. 4.2b). On the other hand, the source time functions are usually longer than 3.0 seconds for events of $m_b \geq 5.5$ [*Cormier & Choy*, 1986]. Interference between the two phases seems inevitable.

In order to solve this problem, both *Wen and Niu* [2001] and *Garcia* [2002] adopted a waveform modeling technique. However, because they chose different methods to deal with the problem of event source time functions and directivities, their estimations of Q_α are significantly different (at least by a factor of 3). In this paper we will present a direct, but arguably effective, approach to circumvent the complex issue of event source time functions and directivities. We discuss the observed distribution of differential travel time residuals and amplitude ratios in terms of structure near the ICB.

4.2   Data, Method, and Results

We systematically downloaded both broadband and short-period vertical component seismograms from IRIS DMC, GRF, GRSN, Jarray, and F-net seismic networks corresponding to recordings in the epicentral distance range of $134^o - 144^o$, for intermediate and deep earthquakes (focal depth >70 km, $M_w \geq 5.5$). These deeper events have shorter source time functions and higher signal-to-noise ratios than shallow events. To preprocess the seismograms, we employed a strictly narrow bandpass filter (2-poled

Butterworth) with corner frequencies of 0.7 and 2.0 Hz (corresponding to 1.5 and 0.5 seconds in period). The goal is to try to retrieve events whose 1.0 Hz energy was released in a short time and impulsively (within about 1.0 second), no matter how long their overall source time functions were. For this kind of events, we expect to observe pairs of well-separated PKIKP and PKiKP phases. Obtaining well-separated pairs of PKIKP and PKiKP phases requires us to apply a high frequency narrow band-pass filter. Therefore, we will not use the slope of amplitude spectrum ratio to estimate Q_α, as *Souriau and Roudil* [1995] did, taking advantage of the broad-band naturally well-separated PKIKP and PKPbc waveforms. In this paper, we directly measure amplitude ratios of PKIKP versus PKiKP in the time domain in order to estimate Q_α at the top of the inner core.

Our method requires to account for the phase shift of PKiKP with respect to PKIKP. Because PKiKP is a post-critically reflected wave at the ICB, the phase shift between PKiKP and PKIKP is approximately in the range of 142° to 163° (arguably close to 180°) in the epicentral distance range of our study (Fig. 4.2a). This means that if we reverse (that is multiplying the corresponding portion of the seismogram by -1) the PKiKP phase, the two phases should be very similar, as we verified using synthetic seismograms.

After data preprocessing, our data-picking criteria are as follows: (1) the signal-to-noise ratio before the identified PKIKP is ~ 6 or more; (2) the signal-to-noise ratio within about one duration of the waveform after the identified PKIKP is ~ 3 or more; (3) the identified PKIKP and PKiKP phases are well-separated; (4) the reversed PKiKP waveform is similar to the PKIKP waveform. Following the above criteria, we successfully selected 280 pairs of high-quality PKIKP and PKiKP phases (Fig. 4.3).

This large dataset of well-separated and similar PKIKP and reversed PKiKP waveforms provides us a unique opportunity to explore the seismic structure at the top of the inner core. In order to study the P-wave velocity structure, we adopt two

distinct methods to measure the differential travel time between PKiKP and PKIKP. The first one is hand-picking [*Niu & Wen*, 2001; *Wen & Niu*, 2002; *Stroujkova & Cormier*, 2004] before reversing PKiKP phases, and the second is cross-correlation after reversing PKiKP phases. Results from these two methods differ little (less than ~ 0.1 sec). Then we calculate the differential travel time residuals between PKiKP and PKIKP with respect to the reference seismic model PREM [*Dziewonski & Anderson*, 1981].

In order to study the Q_α structure, firstly, we measure the peak-to-peak amplitude ratios of PKIKP to PKiKP in the narrow band considered. Our measurements are carried on with Seismic Analysis Code (SAC). The measurement error of these amplitude ratios is negligible. Thus any possible source of random error should be related to the background noise. Our strict criteria of selection above can help us reduce this kind of random error significantly.

Secondly, we apply geometrical spreading, transmission, and reflection corrections for the measured amplitude ratios [*Cao & Romanowicz*, 2004a], based on the reference seismic model PREM. The ratios of PKIKP and PKiKP geometrical spreading factors are functions of take-off angles, ray parameters, and their corresponding derivatives. The transmission and reflection coefficients are calculated with respect to various discontinuities (solid-solid, solid-liquid, and liquid-solid) in the earth.

Finally, we directly estimate Q_α from corrected amplitude ratios according to the definition of the seismic attenuation in the time domain:

$$\frac{A_{PKIKP}}{A_{PKiKP}} = e^{-\pi f t / Q_\alpha}$$

where A_{PKIKP} and A_{PKiKP} are the corrected amplitudes for PKIKP and PKiKP, respectively; t is the travel time of PKIKP in the inner core; f is the frequency, and Q_α is the quality factor which characterizes the seismic attenuation at the top of the inner core. Although, theoretically, the phase shift between PKIKP and PKiKP

doesn't affect the measurement of amplitude ratios, we verified this in an experiment. We computed a series of phase shifted waveforms (140°, 145°, 150°, 155°, 160°, and 180°, respectively) with respect to an observed PKIKP phase. The resulting variations of amplitude ratios are ~ 0.01, which is too small to cause a noticeable change of the estimated Q_α.

The uncertainty of our Q_α estimations can be divided into random and systematic errors. The systematic error is related to the reference seismic model. When we estimated Q_α using AK135 [*Kennett et al.*, 1995] and PREM2 [*Song & Helmberger*, 1995] instead of PREM model, results are very compatible. The difference between Q_α estimated from AK135 and PREM2 is less than ± 10, and both estimates are consistently higher (~ 30) than those estimated from PREM model. In these three models, P-wave velocity contrasts (or sharpness) at the ICB and seismic structure near (both above and below) the ICB are rather different, but their influence on our Q_α estimations are small.

As for the random error (corresponding to our first step), an ideal way to estimate it is to use a number of different events in similar locations recorded by the same stations. Unfortunately, we do not have this kind of data. Thus we try to estimate standard deviations by distinguishing three cases. (1) in the epicentral distance range from 142° to 144°, we directly estimate a standard deviation ~ 43. (2) in the shorter epicentral distance range, we look for the regions where azimuths, sampling depths, and turning points of PKIKP are close ($\sim 2^o$ x 2°) in the eastern hemisphere. We obtain an average standard deviation ~ 24. (3) Similarly, in the western hemisphere, we obtain an average standard deviation ~ 50. These estimated standard deviations cannot be completely attributed to the background noise because of the likely contribution from small scale heterogeneity at the top of the inner core.

For differential travel time residuals, our results show a striking hemispherical pattern in the epicentral distance range 135° to 142° (corresponding to depths of approximately 32 to 85 km beneath the ICB) (Fig. 4.4a and b), in agreement with the

observations of *Niu and Wen* [2001] and *Garcia* [2002]. Beyond 142°, the hemispherical pattern is not as clear (Fig. 4.4b).

For the quality factor Q_α, our results also show a reliable hemispherical pattern almost in the same epicentral distance range (135°-141.5^o) (Fig. 4.4c, 4.5b). In the western hemisphere Q_α steadily decreases as a function of distance, with a mean of about 335 ± 50 which is lower than *Wen and Niu*'s [2002] estimate ($Q_\alpha \sim 600$).

In the eastern hemisphere, Q_α increases as a function of distance, with a mean of about 160, which is also lower than *Wen and Niu*'s [2002] estimate ($Q_\alpha \sim 250$). In the distance range overlapping that of *Garcia* [2002] (from 135° to 136°) the mean of Q_α is about 125 ± 24, which is relatively compatible with his values (< 100).

Beyond an epicentral distance of 141.5^o, the hemispherical pattern in Q_α disappears (Fig. 4.4d, 4.5b), as does that in the differential travel time residuals. The Q_α measurements are consistent with a mean of 210 ± 43. This value is compatible with *Souriau and Roudil*'s [1995] estimate ($Q_\alpha \sim 200$).

We also examine the variation of Q_α versus ξ (PKIKP ray angle with respect to the Earth's spin axis) and differential travel time residuals versus ξ, respectively (Fig. 4.6). Our observations do not show any evidence for seismic anisotropy, however, our range of ξ is too limited to draw any definitive conclusions.

4.3   Discussion

4.3.1   Measurement Robustness

In comparison with the method of waveform modeling, our approach has several advantages. We don't have to consider source time functions, directivities, and station-sided crustal structure, which are usually regarded as the main source of the uncer-

tainty in the Q_α measurement [*Garcia*, 2002]. In comparison with the method of amplitude ratio of PKIKP versus PKPbc, which is used at larger distance and therefore samples deeper in the inner core, the sampling depth range of PKIKP is much closer to the ICB and so the revealed seismic structure may be more directly related to the freezing process at the ICB. Also, the entry (and exit) points of PKIKP and PKiKP into the core at the CMB are much closer (less than ~ 120 km) than those of PKIKP and PKPbc (from ~ 210 to ~ 550 km). The two phases PKIKP and PKiKP are so close that we may assume that they are affected in the same way by heterogeneities in the crust, mantle, and even the outer core. If we assume a 10% velocity perturbation at the base of the D", its influence on our estimation of Q_α is less than 1%. On the other hand, for the reflection of PKiKP at the ICB, if we assume a 5% velocity change (keeping its super critical reflection), the coefficient variation is also less than 1%, and so resulting influence on Q_α estimations is negligible. Finally, the difference in take-off angle between PKIKP and PKiKP at the source is significantly smaller (less than 1.5^o) than that between PKIKP and PKPbc (from $\sim 3.0^o$ to $\sim 6.0^o$). So the uncertainty related with the P-wave radiation pattern can be more confidently ignored in our estimation of Q_α.

The noise sources for our measurements are mainly the random background noise near stations, PKP precursors scattered in the mantle [*Hedlin et al.*, 1997], and the possible interference with the PKPbc phase beyond an epicentral distance of 141°. The reference seismic model PREM [*Dziewonski & Anderson*, 1981], IASP91 [*Kennett & Engdahl*, 1991], and AK135 [*Kennett et al.*, 1995] all predict that PKPbc doesn't appear until 144.5^o, but it has been pointed out that in practice PKPbc might be observed as early as at the epicentral distance of 141° [*Souriau & Roudil*, 1995]. We believe our strict data picking criteria can effectively avoid the possible influence from the unexpected PKPbc in our range of study and expand the distance range of PKiKP versus PKIKP to the epicentral distance of 144°: (1) The waveforms of PKIKP and PKPbc are very similar. Once the PKPbc starts to appear, its travel time should be very close to that of PKIKP, and so a strong constructive interference usually happens. (2) in our epicentral distance range of study, the travel time difference of

PKIKP and PKiKP is at most 3.2 seconds. If PKPbc appears between PKIKP and PKiKP we could not identify two almost completely separated phases. (3) If PKPbc arrives closer to PKiKP, the two phases would destructively interfere with each other. Consequently, no PKiKP could be identified. (4) The most important point is that we are always looking for two well separated phases and the latter one is almost reversed in polarity with respect to the first one. Therefore, as we showed in Fig. 3c, we can't wrongly identify PKPbc as PKiKP even if it might occasionally appear before 144°. In fact, the potential PKPbc in our range of study is most likely a kind of low frequency diffracted wave near B cusp (Cormier, personal communication). After our relatively high frequency filtering, it will not to affect our identification of PKiKP.

The energy level of scattered PKP precursors is usually $\sim 10\%$ of the PKIKP's [39]. Sometimes they are hard to be discerned from the background noise without stacking and sometimes they are clear even in single station traces. Our required signal-to-noise ratios may help us limit the influence of both background noise and anomalous PKP precursors. Also, the requirement of similarity of PKIKP and reversed PKiKP phases further reduces the influence of noise through our data selection.

Although we employ a strictly narrow filter, we can not obtain any well-separated pairs of PKIKP and PKiKP phases in the epicentral distance range from 134° to 135°. Our observations show that the duration of the PKIKP waveform is usually longer than 1.3 seconds (Fig. 4.3), which is larger than the predicted differential travel time between PKIKP and PKiKP in the distance range less than 135°. So the interference is a significant issue when using PKIKP and PKiKP phases to study the structure at the very top of the inner core [*Cormier & Choy*, 1986; *Garcia*, 2002]. It is possible to measure the differential travel time of the interfering phases of PKIKP and PKiKP using waveform modeling, but it seems very difficult to accurately measure the amplitude ratio of PKIKP versus PKiKP. *Garcia* [2002], *Wen and Niu* [2002] used distinct methods to do the waveform modeling of PKIKP and PKiKP. They both proposed a hemispherical pattern for P-wave velocity but they obtained incompatible estimates of Q_α in the eastern hemisphere (by a factor of more than 3.0). In the

epicentral distance range (135° to 136°) our estimate of Q_α in the eastern hemisphere is closer to *Garcia*'s [2002] result. This suggests to us that the direct consideration of source time functions and directivities is important for PKIKP and PKiKP waveform modeling due to the likely interference of these phases in a broadband sense. On the other hand, our Q_α measurements are compatible with *Souriau and Roudil*'s [1995] broadband estimates in the overlapping distance range (142° to 144°), further adding confidence in our results.

4.3.2 Interpretation

Our observations present additional evidence for a seismically isotropic hemispherical structure (high velocity low Q_α in the eastern hemisphere and low velocity high Q_α in the western hemisphere) at the top of the inner core [*Niu & Wen*, 2001; *Garcia*, 2002; *Wen & Niu*, 2002]. Variations of velocity and Q_α are not related to ξ, which is the ray angle of PKIKP with respect to the Earth's spin axis (Fig. 4.6).

Our observations also further indicate that this hemispherical isotropic structure disappears at a depth of about 85 km beneath the ICB. The most intriguing point is that our observation of Q_α provides evidence for a pronounced transition region of seismic attenuation at the top of the inner core, with hemispherical differences (Fig. 4.7).

So far, both scattering related with the iron crystal structure [*Bergman*, 2002] and diffusion related with liquid inclusion [*Singh et al.*, 2000] can account for previous observations that Q_α increases with depth (deeper than 100 km) [*Song & Helmberger*, 1995; *Souriau & Roudil*, 1995; *Li & Cormier*, 2002]. As for which is the dominant factor, it is still an unsettled issue. Possibly this question depends on the depth range of study. *Cormier and Li* [2002] suggested that the inner core can be roughly divided into three sections based on iron crystal texturing: perfectly aligned deep part, incomplete aligned upper part, and a mushy zone at the top of the inner core. In the

mushy zone, there would be significant exchange of fluid with the outer core because the estimated mushy zone Rayleigh number is at least one thousand times supercritical [*Bergman*, 2002]. In what follows, we discuss our results under the assumption that the mushy zone exists, although alternative interpretations could be sought in terms of solid state texture effects. The mushy zone at the very top of the inner core may exhibit lateral variations in its melt fraction content, related to possible differences in heat flow near the ICB induced by lateral variations in temperature at the CMB. In the mushy zone it is reasonable to assume that the porosity (or melt fraction) decreases with depth, due to the compaction of the solid-liquid composite resulting from expulsion of liquid towards the outer core [*Loper & Fearn*, 1983; *Sumita et al.*, 1996]. *Singh et al.*'s [2000] experiment, in which they assume that melt inclusions are not connected to each other, explicitly demonstrates that Q_α decreases as a function of the increasing melt fraction. Based on their experiment, we can readily infer that Q_α should increase with depth.

In the eastern hemisphere, at least up to 32 km beneath the ICB (the upper limit of our sampling in the inner core), our Q_α estimates are compatible with such a model. In the western hemisphere, however, the behavior is different. From ~ 32 to ~ 85 km beneath the ICB, Q_α decreases from ~ 335 to ~ 210. We suggest that in the western hemisphere porosity is higher and melt inclusions are connected and exchange fluid with the outer core [*Bergman*, 2002], resulting in higher Q_α. P-wave velocity may, in turn, be reduced. Nevertheless, the well-linked or concentrated liquid may not be distributed evenly in the western hemisphere. In some regions (for example, the offshore northwest of Africa) or other yet unsampled areas (Fig. 4.4c, 4.5b), there may be well-isolated liquid inclusions.

The contrast between high Q_α and low P-wave velocity in western hemisphere and low Q_α and high P-wave velocity in the eastern hemisphere most likely reflects significant hemispherical difference of the freezing rate at the ICB. *Sumita and Olson* [1999] suggest that a thermally heterogeneous mantle could control the convection in the liquid outer core and result in different heat flow near the ICB. On the cold western

side the rapid freezing might lead to higher porosity.

The disappearance of the hemispherical pattern in Q_α suggests to us that there is no significant difference in the nature of liquid inclusions in the two hemispheres within the depth range from ~ 85 km to 110 km. In consequence, the resulting contributions to attenuation, due to the thermal and material diffusion [*Loper & Fearn*, 1983], are basically compatible. (Fig. 4.5b). However, the more scattered differential travel time residuals (Fig. 4.5a) imply that the perturbation of velocity in this depth range can not be controlled by the texturing difference of liquid inclusions as in the upper portion of the top of the inner core. At this time we have too few travel time measurements at distances greater than 142° to propose a unique interpretation of this scatter.

The existence of a mushy layer theoretically might cause weak P-to-P and P-to-S conversions more or less at the ICB. However, this kind of influence should strongly depend on the frequency range of study. The mushy layer is not so soft as the mud. It has solid iron crystal frame and is filled with liquid inclusions. The dimension of the liquid inclusions is supposed to be around 10 km. So, they are visible for short period seismic wave study (e.g., this Chapter) and almost invisible for our long period seismic wave study (e.g., Chapter 5 and 6).

4.4   Conclusion

Our estimations of Q_α at the top of the inner core strongly suggest the existence of a transition zone of the seismic attenuation in the western hemisphere, where Q_α first decreases from almost infinite [*Cormier & Richards*, 1976] at the ICB to ~ 210 at about 85 km beneath the ICB and then increases with depth into the inner core [*Souriau & Roudil*, 1995]. In the eastern hemisphere, we do not directly observe the transition but we infer that must be located in the top 32 km of the inner core, which is supported by *Stroujkova and Cormier*'s [2004] most recent result that there is a

low velocity layer in the upper most inner core in this region. The observed striking hemispherical pattern in seismic attenuation is presumably related to the melt fraction and the connectivity of the liquid inclusions. We infer that the liquid inclusions may be well isolated in the eastern hemisphere, while in the western hemisphere, they are better connected (as a result, the porosity is also higher). This kind of hemispherical pattern is probably caused by hemispherical temperature differences at the ICB [*Sumita & Olson*, 1999]. On the cold western side, a faster freezing rate of the liquid material at the ICB can lead to higher porosity.

Our measurements of differential travel time residuals of PKiKP versus PKIKP confirm the existence of a hemispherical pattern of the isotropic P-wave velocity at the top of the inner core [*Niu & Wen*, 2001; *Garcia*, 2002]. Low velocity, high Q_α, and high porosity are present in the western hemisphere, and high velocity, low Q_α, and low porosity, respectively, in the eastern hemisphere.

However, the hemispherical patterns of Q_α and P-wave velocity can not extend very deep into the inner core. Both of them disappear almost simultaneously ~ 85 km beneath the ICB. Below this depth, as *Creager* [1999] suggested, the isotropic average velocities may be the same in both hemispheres.

Figure 4.1: Ray paths of PKiKP (reflected P wave from the ICB) and PKIKP (P wave passing through the inner core). The two phases may appear simultaneously as early as 120°, but we can only obtain well-separated PKIKP and PKiKP phases in the epicentral distance range from 135° to 144°.
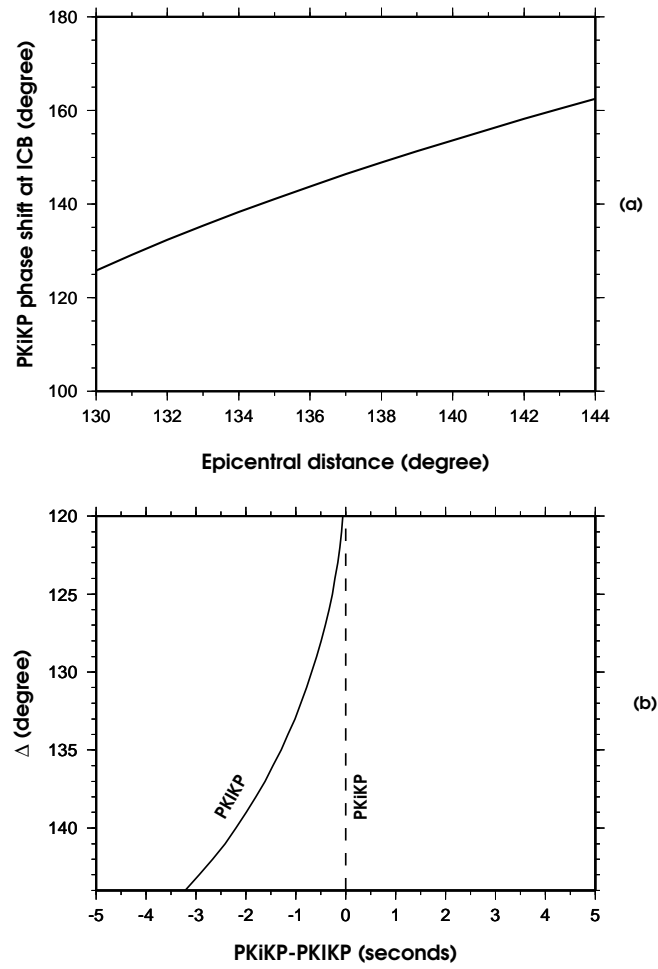
Figure 4.2: (a) Phase shift of the post-critically reflected PKiKP with respect of PKIKP. (b) Differential travel time of PKIKP and PKiKP. The reference seismic model is PREM.
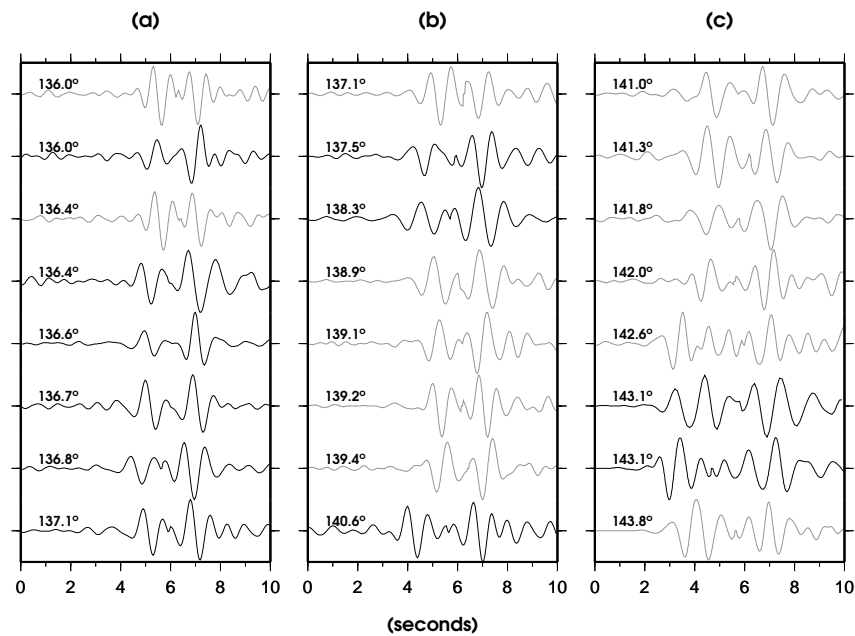
Figure 4.3: Examples of well-separated PKIKP and reversed PKiKP phases. The original broadband or short period seismograms are filtered with a strictly narrow bandpass filter (around 1.0 Hz from 0.7 to 2.0 Hz). Grey traces are with PKIKP turning points in the western hemisphere, and black ones are with PKIKP turning points in the eastern hemisphere. In the distance range from 141° to 144° (panel c) we observe well-separated pairs of PKIKP and reversed PKiKP as both in the shorter (a) and longer (b) distance ranges.
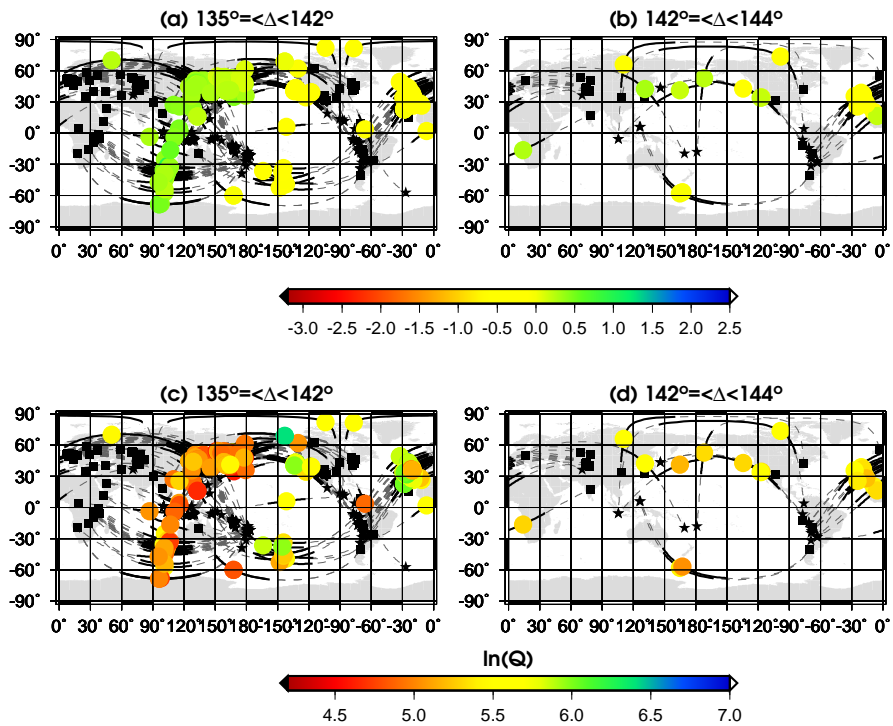
Figure 4.4: Geographical distribution of differential travel time residuals between PKiKP and PKIKP and estimations of Q_α (referring to seismic model PREM). (a) and (c) show clear hemispherical patterns of residuals and Q_α, respectively, in the epicentral distance range from 135° to 142° (corresponding to ~ 32 to ~ 85 km beneath the ICB). (b) and (d) show that hemispherical patterns disappear deeper than ~ 85 km beneath the ICB. Dashed lines are ray paths from events (stars) to stations (squares), and the bold lines are the inner core portion of PKIKP ray paths. The circles are the turning points of PKIKP in the inner core.
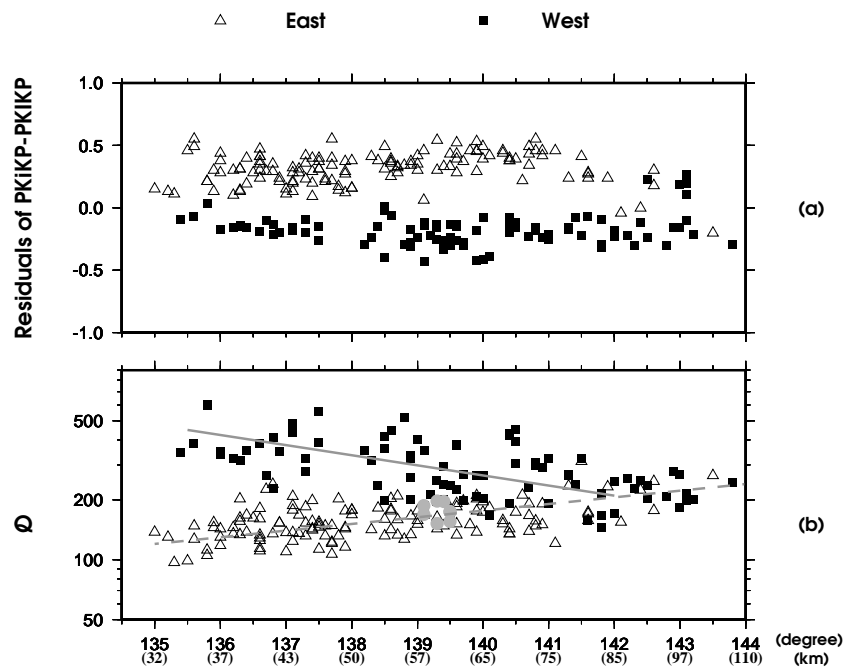
Figure 4.5: (a) Differential travel time residuals (referring to PREM). The measurement error is less than ~ 0.1 second. (b) Q_α with respect to the epicentral distance and depth beneath the ICB. The average standard deviations are from ~ 24, ~ 43, to ~ 50. High-lighted green squares show the data sampling offshore northwest of Africa. The event epicentral distances were all calibrated with a reference focal depth 100 km.
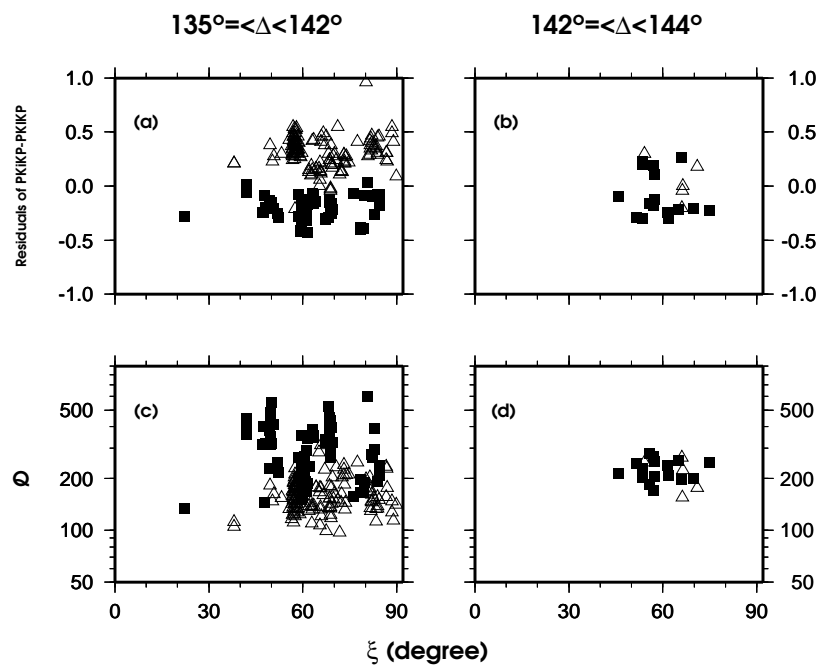
Figure 4.6: Differential travel time residuals between PKiKP and PKIKP and Q_α versus ξ (ray angle of PKIKP with respect to the Earth's spin axis), respectively.
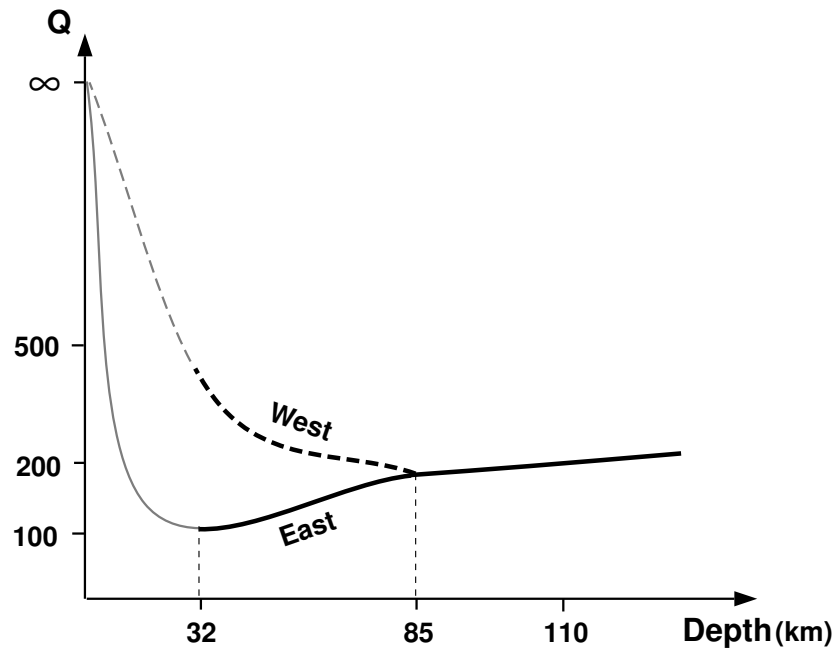
Figure 4.7: Cartoon diagram of the hemispherical transition of seismic attenuation at the top of the Earth's inner core, where Q_α turns from decreasing to increasing with depth. Our sampling range is approximately from 32 to 110 km. In the deeper depth range, the increase of Q_α with respect to depth was suggested by a number of previous studies [31]. The grey thinner lines in the shallower depth range are inferred from our observation and *Stroujkova and Cormier*'s [2004] result.

Chapter 5

PKJKP

This chapter has been published in *Science* [*Cao et al.*, 2005] under the title 'An Observation of PKJKP: Inferences on Inner Core Shear Properties', and also includes Supporting Online Material published at www.sciencemag.org/cgi/content/full/1109134/DC1 (sections 5.3-5.6).

Summary

The seismic phase PKJKP, which traverses the inner core as a shear wave, and would provide direct evidence for its solidity, has been difficult to detect. Using stacked broadband records from the Gräfenberg array in Germany, we document a high signal to noise phase, whose arrival time and slowness agree with theoretical predictions for PKJKP. The back-azimuth of this arrival is also consistent with predictions for PKJKP as is the comparison with a pseudo-liquid inner core model. Envelope modeling of the PKJKP waveform implies a slightly larger shear velocity gradient with depth in the inner core than that in PREM model.

5.1   Introduction

Soon after *Lehmann* [1936] discovered Earth's inner core through the analysis of travel times of teleseismic body waves, *Birch* [1940] suggested that the inner core should be solid as a result of freezing of liquid iron. Thirty years later, indirect evidence of the solidity of the inner core was documented by means of seismic normal mode eigenfrequency measurements [*Dziewonski & Gilbert*, 1971]. However, the observation of the phase PKJKP, which traverses the inner core as a shear wave (Fig. 5.1A), has been a controversial issue. *Julian et al.* [1972] and *Okal & Cansi* [1998] each suggested the detection of PKJKP based on data from short-period seismic arrays at frequencies of $\sim$ 1.0 Hz and 0.1-0.5 Hz, respectively. *Deuss at al.* [2000] argued that these two claims were misidentifications, and instead, proposed an observation of pPKJKP+SKJKP between 0.01-0.1 Hz.

PKIKP, which traverses the inner core as a compressional wave (Fig. 5.1A), is routinely observed. It should be observed simultaneously with PKJKP in the epicentral distance range 116° to 180°, according to the seismic reference model PREM [*Dziewonski & Anderson*, 1981]. The relative amplitude of PKJKP varies strongly with frequency (Fig. 5.1B). Although we cannot rule out the possibility of observing PKJKP at frequencies of 0.1 to 0.5 Hz [*Okal & Cansi*, 1998], it is more likely to be found at lower frequencies [*Deuss et al.*, 2000].

5.2   Data, Results, and Discussion

Here we use data from the broadband Gräfenberg Seismic Array (GRF) in Germany to detect PKJKP (Fig. 5.1C). With an aperture of $\sim$ 100km x 50km, GRF has provided continuous records at 13 stations since 1980. Its location with respect to frequent

large events ($Mw > 7.0$) in the south Pacific Ocean at distances of $\sim 140^o$, make it an ideal broadband seismic array to study PKJKP. We studied ~ 20 large events in the vicinity of Tonga and Santa Cruz islands occurring from 1980 to 1999 [*Engdahl et al.*, 1998]. One of them (Mw=7.3, depth=76 km, 02/06/1999) is uniquely favorable to the observation of PKJKP (Fig. 5.1C). We chose the 0.06 to 0.1 Hz band for our analysis. From 100 s before PKIKP and 200 s after PKJKP, the amplitude spectrum (Fig. 5.2B) indicates that the amplitude decays significantly at periods longer than 0.06 Hz. Only in the frequency range 0.06-0.1 Hz is the amplitude relatively constant.

The GRF seismic array has a relatively small aperture, but there is still noticeable variation of differential travel times of PKIKP, which can be as large as 0.6 s across the array. This variation is presumed to be primarily related to crust and (or) uppermost mantle heterogeneity just beneath the array. This heterogeneity should also influence PKJKP at a similar level, because the two ray paths are very close in this region (Fig. 5.1A). GRB2, which is at the center of this broadband seismic array, is chosen as the reference station.

We aligned the seismograms with respect to the origin time of the event and made an array-sided travel time correction (Fig. 5.2A), filtered the data with a band-pass filter, normalized the seismograms with respect to the first arrival (PKIKP+PKiKP), and stacked them using the phase weighted stack (PWS) technique [*Schimmel & Paulssen*, 1997]. We computed two vespagrams. The first one (Fig. 5.3A) corresponds to the time and slowness window in which we expect the group PKIKP/PKiKP and their depth phases. The second one (Fig. 5.3C) corresponds to the predicted window for PKJKP, according to the PREM model [*Dziewonski & Anderson*, 1981]. We observe clear energy maxima in both windows. We also observe a clean stacked waveform corresponding to the energy maximum in the PKJKP window (Fig. 5.3D). We verified that this phase arrives within 5° of the great circle path from the source, ruling out a scattered near array phase (Fig. 5.3E). We further investigated whether this phase could be a mantle, outer core, or even crust phase, by considering for reference a model with a liquid inner core, as was done by *Duess et al.* [2000]. In such a model,

there would not be a PKJKP phase. We constructed synthetic vespagrams using the Direct Solution Method (DSM) [*Takeuchi et al.*, 1996] (see also sec. 5.4).

Consideration of near source local structure, as well as moment tensor information (see sec. 5.3) allowed us to model both the waveform of PKIKP+PKiKP and its depth phase, pPKIKP+pPKiKP (Fig. 5.4A) for both solid and liquid inner cores, providing accurate source time functions for the synthetic calculations. It is not possible to discern PKJKP in an individual synthetic trace, because PKJKP is so weak that it is deeply hidden behind unidentifiable mantle, outer core, and crust phases. In order to extract the PKJKP phase, we generated synthetic differential seismograms between solid inner core and liquid inner core (Fig. 5.4B). However, even when we chose Q_β=300 for the solid inner core PKJKP and pPKJKP were not prominent enough. This is because transmission coefficients of the inner core P-wave phases (PcPPKIKP, pPcPPKIKP, sPcPPKIKP, and PKKPdf, see Fig. 5.8) are artificially increased in the case of the liquid inner core, compared to the real earth. This artificial energy is weak, but stronger than that of the potential PKJKP.

The liquid inner core model serves to remove the inner core shear wave energy from the time window shown in Fig. 5.4B, so as to better extract PKJKP and pPKJKP in the differential seismogram. We can also achieve this by reducing the shear wave velocity in the inner core by 8% compared to the PREM model. In this case, the inner core shear wave energy moves beyond the appropriate time window (PKJKP and pPKJKP are moved backwards by $\sim$ 50 s). Meanwhile, the artificial compressional energy is significantly reduced (Fig. 5.4C) and both PKJKP and pPKJKP phases are present in the synthetic differential seismogram. pPKJKP is $\sim$ 2.2 times weaker than PKJKP. If in addition, we take the background noise into account, amplitude ratio of PKJKP to pPKJKP may be as large as $\sim$ 4.8 (Fig. 5.6). Therefore, it is not surprising that we do not observe pPKJKP for this event. We thus only discuss PKJKP. Synthetic vespagrams for this pseudo-liquid inner core (Fig. 5.5A) show that there is no energy maximum corresponding to waves with negative slowness, confirming that the target phase observed in Fig. 5.3C, D and E is not a crust, mantle, or outer core phase. The

phase observed in Fig. 5.3C and D cannot be due to random noise. (1) The PWS stacking technique [*Schimmel & Paulssen*, 1997] is designed specifically to remove the influence of the background incoherent noise. (2) If what we observed were random noise, the energy extrema should also distribute randomly in the observed vespagram.

The PKJKP waveform (Fig. 5.3D) allows us to estimate the shear wave velocity in the inner core by envelope function modeling. Synthetic envelope functions of PKJKP are computed from the synthetic differential seismograms between the solid inner core and the pseudo-liquid inner core (see sec. 5.5). We process the synthetic differential seismograms in the same way as the observed seismogram and compare the envelope to the observed one (Fig. 5.3D). The envelope function modeling suggests that the observed PKJKP is about 9.0 s faster than the synthetic PKJKP. It implies that the shear wave velocity in the inner core may be $\sim 1.5\%$ faster than that for the PREM model [*Dziewonski & Anderson*, 1981]. PREM is primarily based on normal mode data which mainly sample the shallow portion of the inner core, whereas here, PKJKP samples the central part (Fig. 5.1A). Thus, it is in agreement with previous results if one allows for a slight increase in shear velocity with depth in the inner core.

The use of GRF array data was key to this study. Compared with global broadband seismic networks [*Deuss et al.*, 2000], GRF has a number of distinct advantages: (i) we can examine all potential interfering phases, which are expected to appear in the time window of our study, to make sure they arrive sufficiently far away in time and (or) slowness from PKJKP. When using global networks, the number of identifiable interfering phases is much larger. So it seems harder to avoid some relatively strong phase(s) to appear close to PKJKP (or pPKJKP). Usually, the stacking technique cannot suppress this kind of energy completely to prevent these phases from interfering with the very weak PKJKP (or pPKJKP) en ergy [*Schimmel & Paulssen*, 1997]. (ii) we can expect that the presumed PKJKP phases recorded at every station in GRF are coherent. When using global networks, polarities of the expected PKJKP (or pPKJKP) phases in different quadrants may be opposite, which needs to be corrected for. (iii)GRF stations use identical seismometers. We can directly process the data

without removing instrument responses as we adopt normalized traces to constrain Q_β. Although the aperture of GRF seismic array is relatively sm all, for this very sharp large event, it is sensitive to small perturbations in arrival times (as low as $\sim 0.3s$) using vespagrams. This is also the reason why the array-sided travel time correction is necessary.

5.3   Event Characterization

The event occurred in the slab of the Santa Cruz Islands subduction zone. Depth phases pPKIKP+pPKiKP and pPKJKP are reflected from the oceanic floor, and the distances of their surface bounce points are within 12 km. This requires us to take both a magma wedge and an oceanic layer into account in the near source region. In a magma wedge, quality factors for both compressional and shear waves are thought to be extremely low (approximately 50 and 20, respectively) [*Barazangi & Isacks*, 1971] in an oceanic layer, part of the energy of reflected phases leaks into the water. We use the moment tensor from the PDE bulletin of the National Earthquake Information Center (http://neic.usgs.gov/neis/sopar/) and the source time function (Fig. 5.1C) obtained from the P phase observed at YAK.

Due to the strong attenuation and poor phase conversions in the inner core, we need to select large earthquakes to search for inner core shear waves. The two events used in the last two studies [*Okal & Cansi*, 1998; *Deuss et al.*, 2000] are both Mw ~ 8.0. However, their corresponding source durations are also much longer (approximately 20 and 40 seconds [*Goes et al.*, 1997], and so the chance for PKJKP and pPKJKP to interfere with other phases is also higher. Thus, it is better to find an event which can balance the magnitude and the source duration. In this study, we systematically examined other large events in Tonga and Santa Cruz Islands regions. Combinations of epicentral distance, event depth, and source duration result in contamination of the potential PKJKP by other phases. We believe this is one of the important reasons

why PKJKP is so difficult to observe.

5.4   Direct Solution Method (DSM)

So far, the identifiable phases for which we may specify the ray paths are very limited. For example, there are only ~ 100 phases in the IASPEI standard seismic phase list. However, theoretically, the number of the possible phases should be infinite. It means that most of the phases are unidentifiable because they are very weak. These phases are usually negligible, but if we want to study the elusive PKJKP phase, they might cause serious problems.

Therefore, for the synthetic modeling of PKJKP, completeness of synthetic seismograms is required. All the synthetic codes which are based on the specification of ray paths are no longer adaptable. DSM computes the displacement solution directly from the Galerkin weak form of elastic equation of motion [*Geller & Ohminato*, 1994]. It can be used to generate highly accurate and complete synthetic seismograms [*Takeuchi et al.*, 1996].

5.5   Envelope Function Modeling

Heterogeneity in the mantle can give rise to dispersion and phase shift of the waveform. Thus we choose to model the envelope function rather than directly the waveform in order to better constrain the arrival of the PKJKP phase. The envelope function is the modulus of a complex trace, for which the original trace is the real part and its Hilbert transform is the imaginary part. In general, the envelope function can characterize the amplitude and arrival time of the energy extrema better than the waveform. The synthetic vespagram for the pseudo-liquid inner core (Fig. 5.5A or 5.7A) implies that we cannot directly use the synthetic envelope function for the solid inner core

to constrain the shear wave velocity. In the time window of interest (Fig. 5.5A or 5.7A), sPcPPKIKP (predicted slowness and arrival time are 1.93 s/deg and 1674 s, respectively) and pPcPPKIKP (predicted slowness and arrival time are 1.93 s/deg and 1665 s, respectively) should have appeared. But the relatively strong synthetic mantle phases (D in Fig. 5.5A or 5.7A), whose slownesses are $\sim 8.0s/deg$, arrive at the same time. The consequence is that only the dominant energy is apparent in the vespagram. Only PcPPKIKP (predicted slowness and arrival time are 1.93 s/deg and 1645 s, respectively) seems less contaminated (Fig. 5.7A and B). The synthetic phase E arrives at almost the same time as the predicted PKJKP. Therefore, it is not possible to obtain a reliable synthetic envelope function for PKJKP from the synthetic seismograms generated for a solid inner core.

The absence of the mantle phase E (Fig. 5.73A) in the observed vespagram suggests that we can directly use the envelope function of PKJKP in the synthetic differential seismogram between the solid inner core and the 'pseudo-liquid' inner core, where the mantle phase E is removed, to constrain the shear wave velocity and Q_β (this will be addressed in Chapter 6) in the inner core.

5.6 Potential Interfering Phases in the PKJKP Window

In the epicentral distance range ($\sim 138^o$) of our study, theoretically, four phases (PcPPKIKP, pPcPPKIKP, sPcPPKIKP, and PKKPdf) (Fig. 5.4) could be present in our PKJKP windows (Fig. 5.3C and D; Fig. 5.5A and B) with respect to the reference seismic model PREM [*Dziewonski & Anderson*, 1981]. Nevertheless, few of PKKPdf have been observed due to its very small reflection coefficient at the CMB [*Earle & Shearer*, 1997]. On the other hand, predicted PcPPKIKP and its two depth phases are barely starting to exist at the distance of GRF (Fig. 5.8). Thus, their observabilities are strongly dependent on the heterogeneity of the real earth.
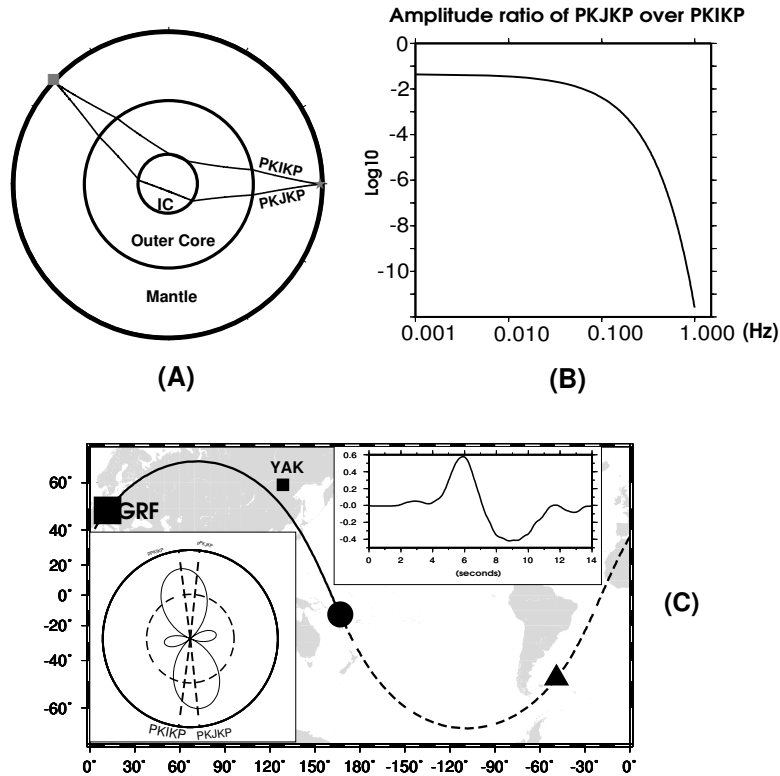
Figure 5.1: (A) Ray paths of PKJKP and PKIKP. The star and square indicate the source and GRF array locations, respectively. (B) The theoretical amplitude ratio of PKJKP over PKIKP as a function of frequency based on the reference model PREM [*Dziewonski & Anderson*, 1981], after correcting for transmission and geometrical spreading [*Cao & Romanowicz*, 2004b]. The reference epicentral distance is 138º. Given the dynamic range of present seismometers, it is unlikely that one could observe PKJKP (or pPKJKP) in the frequency range $\sim$ 1.0 Hz [*Julian et al.*, 1972]. (C) Geographical setting of the event (dot) and GRF seismic array (square). The solid line is the ray path of PKIKP and the dashed line is the ray path of PKJKP projected on the earth's surface. The triangle marks the location of the bottoming point of PKJKP in the inner core. The upper-right inset shows the source time history of the event characterized by a P phase recorded at a broadband station (YAK, distance = 80.1º) of the Global Seismographic Network, located in a similar azimuth as GRF. The lower-left inset illustrates the P-wave radiation pattern in the vertical plane of the great circle. This event is exceptional: (i) the source duration is less than 9 seconds; (ii) the expected PKJKP is emitted from the top of the lobe of the P-wave radiation pattern; (iii) the potential interfering phases identified in previous studies *(4)(5)*, such as PcPPKIKP, pPcPPKIKP, sPcPPKIKP, and PKKPdf, are at least 17 seconds away from the predicted PKJKP arrival time (according to PREM).

PKIKP   **PKJKP**

(A)

GRB2   BHZ
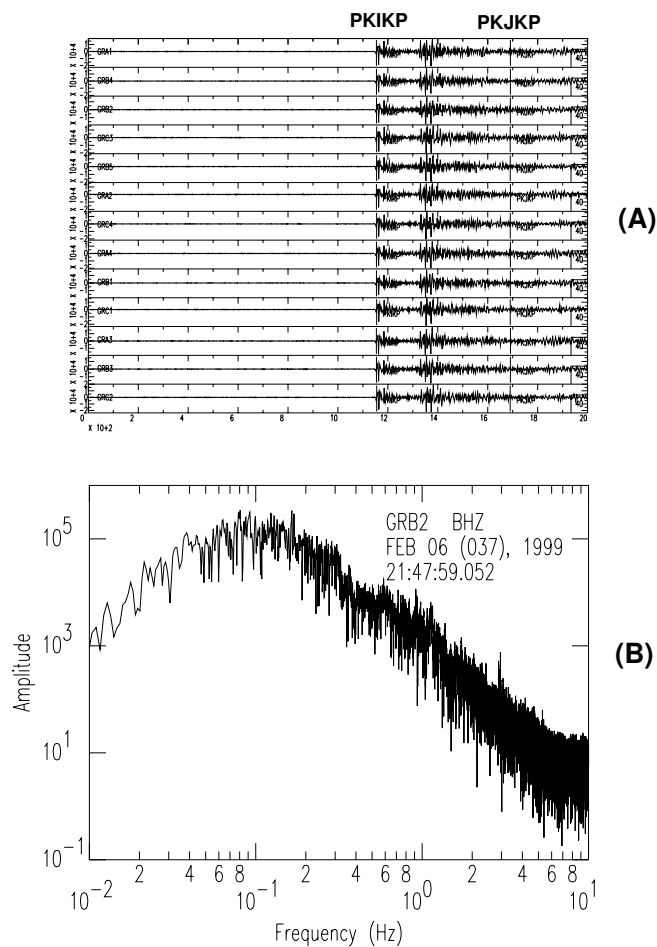FEB 06 (037), 1999
21:47:59.052

(B)

Figure 5.2: (A) Vertical component raw traces for the 02/06/1999 Santa Cruz Island event, starting at the origin time, for stations of the GRF array. PKIKP and PKJKP phases are labeled, respectively. PKJKP is not visible in the individual traces. We choose station GRB2, which is at the center of the GRF array, as the reference station. (B) An example of amplitude spectrum. The time window used to compute the spectrum is from 100 seconds before PKIKP to 200 seconds after PKJKP. The amplitude spectrum is maximum and relatively constant in the frequency range 0.06 to 0.1 Hz.
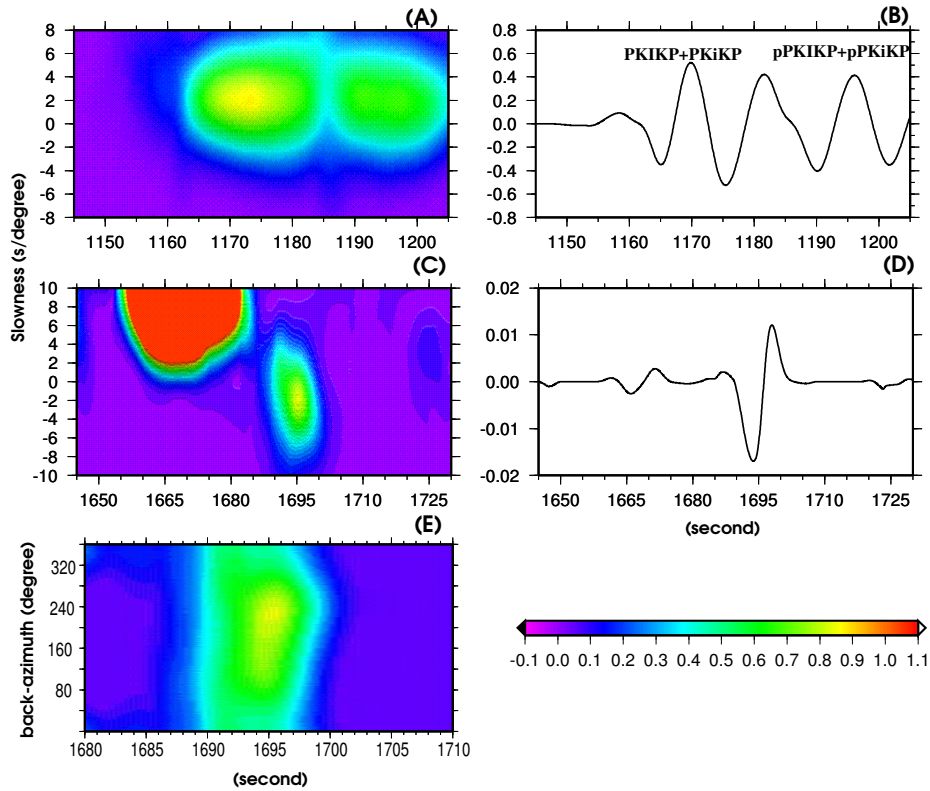
Figure 5.3: (A) Observed vespagram for PKIKP+PKiKP and their depth phases (the energy level is amplified 1.6 times). The center of the energy maximum is for a slowness of $\sim 1.9s/deg$, which is the average of slownesses of PKIKP (1.85 s/deg) and PKiKP (2.04 s/deg) predicted from PREM [*Dziewonski & Anderson*, 1981]. The following weaker energy maximum corresponds to pPKIKP+pPKiKP, and has the same slowness, as predicted from PREM. (B) Stacked waveforms for PKIKP+PKiKP and their depth phases for the energy maximum in (A). (C) Observed vespagram for the potential PKJKP (energy level is amplified 40 times). The slowness of the energy maximum is $\sim -1.6s/deg$, close to the PREM prediction of -1.43 s/deg. The arrival time is also compatible with PREM (1695 sec for the maximum energy, compared to a prediction of 1690 sec for the high frequency onset of the pulse). (D) Stacked waveform corresponding to the energy maximum in (C). (E) Vespagram in the back-azimuth and travel time domain. This shows the direction of arrival of the detected energy, which we identify as PKJKP, in the negative slowness range. The estimated back-azimuth is $\sim 223^o$, which shows that the observed energy propagates along the major arc from the source (the expected back-azimuth of PKJKP is 218.º). This indicates that the observed phase is not a near-array scattered phase, and provides additional evidence for its identification as PKJKP.
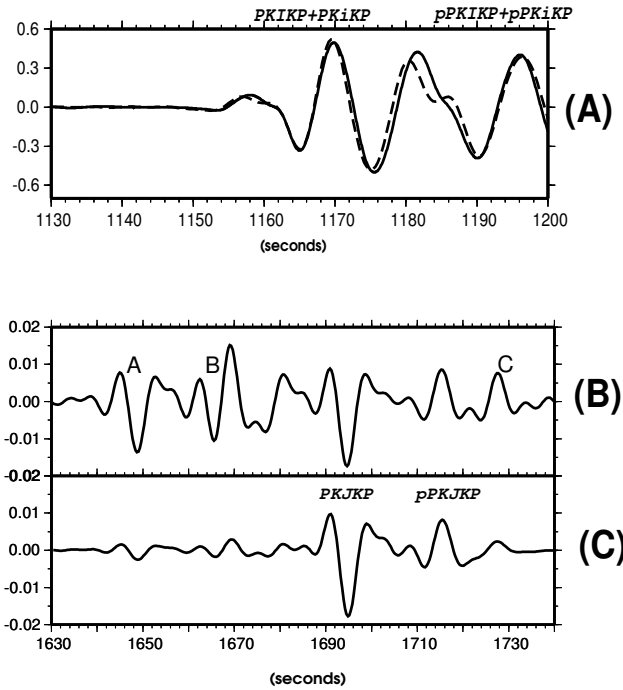
Figure 5.4: Synthetic modeling. (A) Waveform modeling of PKIKP+PKiKP as well as pPKIKP+pPKiKP based on USGS PDE moment tensor. Both observed (dashed line) and synthetic (solid line) seismograms are normalized after applying the band-pass filter (2-poled Butterworth with corner frequencies of 0.06 and 0.1 Hz). Synthetics are obtained using DSM [*Takeuchi et al.*, 1996]. (B) Synthetic differential seismogram for the PREM model compared to a true liquid inner core, for which the shear wave velocity is equal to zero. A (PcPPKIKP), B (pPcPPKIKP+sPcPPKIKP), and C (PKKPdf) are artificially enhanced by the assumption of liquid inner core. (C) Synthetic differential seismogram based on the pseudo-liquid inner core used in this paper. We now can clearly see both PKJKP and pPKJKP phases. The amplitude of PKJKP is approximately 2.2 times larger than that of pPKJKP.
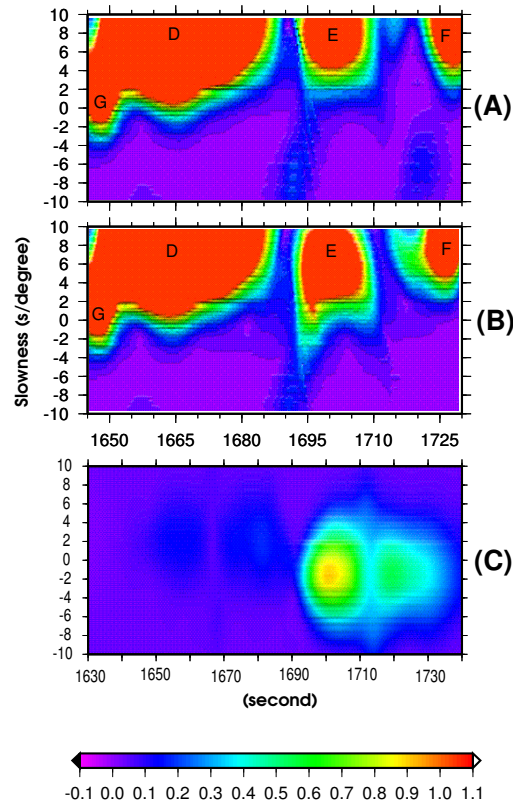
Figure 5.5: Synthetic vespagrams. (A) Pseudo-liquid inner core model. Time windows are identical to those in Fig. 5.3C. Energy level is amplified 40 times, as in Fig. 5.3C. D, E, and F are crust, mantle, or outer core phases, and G is PcPPKIKP. See Fig. 5.7 for a plot with energy level amplified only 20 times to bring out the relative strength of these phases. (B) Solid inner core model, assuming $Q_\beta = 300$. Because the strong mantle phase E in the synthetic model arrives at the same time as PKJKP, the dominant energy of phase E hides the much weaker PKJKP, which only slightly distorts the pattern of phase E. Likewise, pPKJKP slightly distorts the pattern of phase F. Phases E and F are not present in the observed stacks. Therefore, we cannot directly use the comparison of observed vespagram to that predicted by the solid inner core model, and instead, we use a differential seismogram modeling approach, in which the energy from phases E and F is removed. (C) Synthetic differential vespagram in the slowness-time domain. This vespagram is calculated for the solid inner core minus the pseudo-liquid inner core models. The time window is the same as that in Fig. 5.4C. The estimated slownesses of the energy maxima are both -1.4 s/deg, as are the predictions based on PREM. This identifies the two phases in the differential seismogram (Fig. 5.4) as PKJKP and pPKJKP.
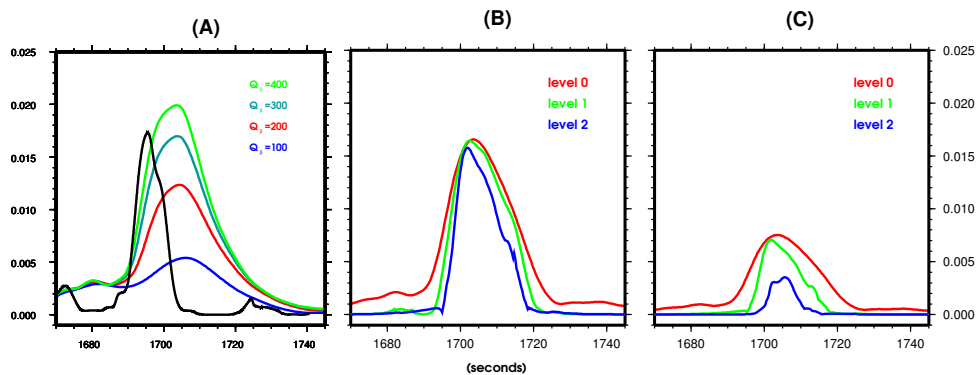
Figure 5.6: (A) Envelope function modeling. The solid black line corresponds to the observed PKJKP, and color lines indicate synthetic PKJKP for different shear wave quality factors assumed in the inner core. Note that a $Q_\beta \sim 300$ appears to fit the data best. Further investigation of this measurment is underway. The envelope function of the observed PKJKP is narrower than that of the synthetic PKJKP. This is due to the background noise at the GRF stations. The existence of the incoherent noise can make the waveform narrower after non-linear stacking [*Schimmel & Paulssen*, 1997]. (B) and (C) are the background noise experiments. The original amplitude in panel (B) is ~ 2.2 times larger than in panel (C). The results indicate that adding background noise (using 200 to 300 s before the first arrival) at individual stations into the synthetic differential seismograms can narrow the resulting envelope functions, as well as reduce the amplitudes. Level 0: no seismic noise is added to synthetic PKJKP traces; Level 1: the original strength of seismic noise is added, and the corresponding amplitude ratio increases to ~ 2.4; Level 2: the strength of seismic noise is amplified twice before being added to the individual traces, and the corresponding amplitude ratio increases to ~ 4.8. The results show that the lower the original amplitude, the more influenced by the background noise after stacking.
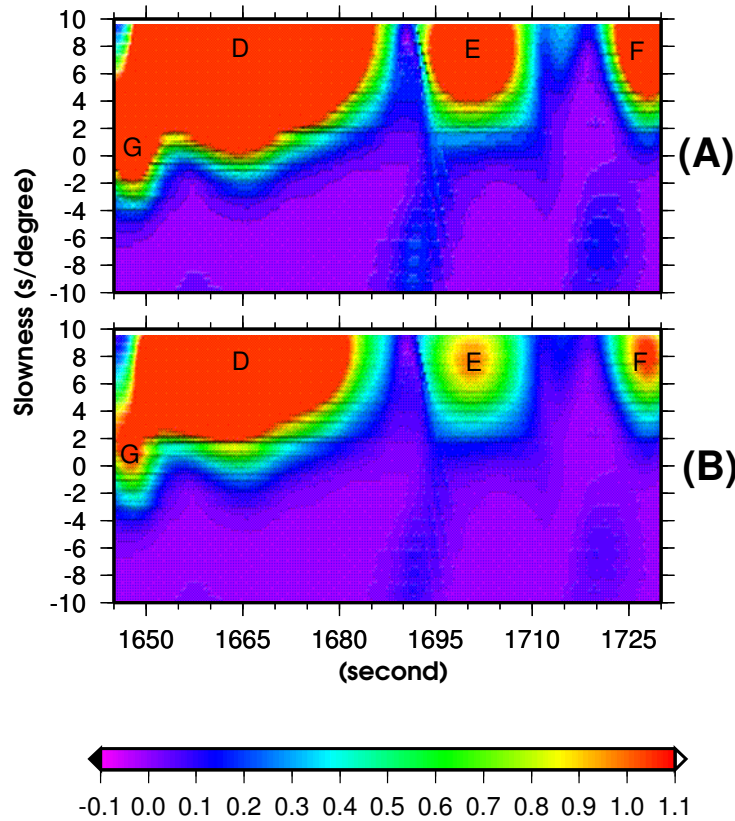
Figure 5.7: Synthetic vespagrams in the slowness and travel time domain. (A) for the pseudo-liquid inner core, which is the same as Fig. 5.5A. (B) Same as (A), but energy level is amplified 20 times, to bring out the relative strengths of these phases. By comparing the synthetic vespagram (Fig. 5.7A) with the observed vespagram (Fig. 5.3C), we may note that mantle phases E and F (Fig. 5.7A) are not observed in the real earth. Only the mantle phase D, which is stronger than mantle phases E and F (Fig. 5.7B), remains in the observed vespagram. This is most likely due to seismic scattering caused by mantle heterogeneity.
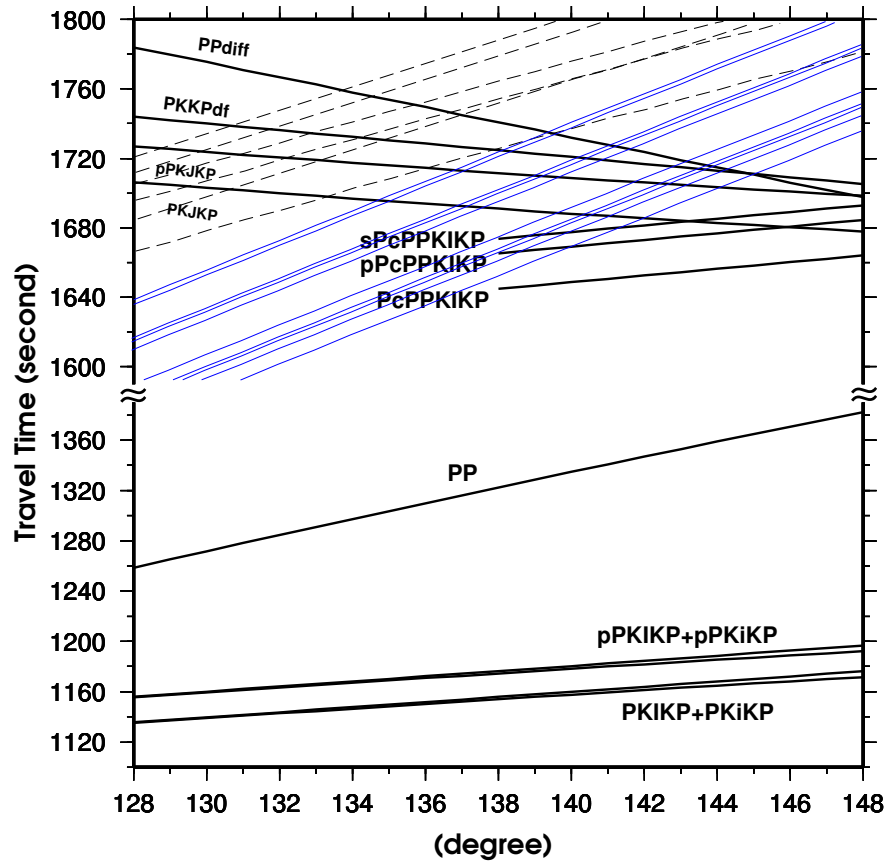
Figure 5.8: Travel times of the phases related to this study (with respect to PREM model). The epicentral distance range of study is $\sim 138^o$. The thin dashed lines are the travel time curves of SKKS, SKKKS, pSKKS, sSKKS, pSKKKS, and sSKKKS phases, respectively, along the travel time axis on the left. The thin blue lines are the travel time curves of pPPPPPmP, pPPPP2(PmP), sPPPPPmP, pPPPP3(PmP), sPPPP2(PmP), sPPPP3(PmP), sPPPP6(PmP), pPPPP8(PmP), sPPPP7(PmP), pPPPP11(PmP), and sPPPP10(PmP), respectively, where n(PmP) means the wave is reflected n times at the Moho. In terms of the travel times and slownesses, the mantle phase D in Fig. 5.5 matches pPPPPPmP, pPPPP2(PmP), sPPPPPmP, pPPPP3(PmP), sPPPP2(PmP), and sPPP3(PmP); E matches sPPPP6(PmP), pPPPP8(PmP), and sPPPP7(PmP); and F matches sPPPP10(PmP), and pPPPP11(PmP).

Chapter 6

Estimate of Inner Core Q_β from PKJKP

This chapter was submitted to *Earth and Planetary Science Letters* with the title 'Constraints on Shear Wave Attenuation in the Earth's Inner Core from an observation of PKJKP' [*Cao & Romanowicz*, 2005].

Summary

Based on the high quality broadband data from Gräfenberg array in Germany, we recently detected a reliable PKJKP phase, for which four kinds of evidence (travel time, slowness, back-azimuth, and comparison with a pseudo-liquid inner core model) were simultaneously provided. Also, for the first time, a clear waveform of PKJKP was observed. This gives us an unprecedented opportunity to put constraints on the shear wave attenuation in the earth's inner core using body waves. In order

to minimize the potential influence of dispersion and phase shift caused by mantle heterogeneity, we adopt an envelope modeling approach. Our results show that the estimated Q_β from shear body wave PKJKP is significantly larger ($\sim 315 \pm 150$) than that from normal mode observations. Because PKJKP samples the deep inner core, this indicates an increase of Q_β with depth in the inner core, in agreement with what is generally observed for Q_α.

6.1   Introduction

Seismic attenuation in the inner core may provide significant insight into the solidification processes at the earth's center. Even before the first indirect evidence of the solidity of the inner core was documented by means of seismic normal mode observations [*Dziewonski & Gilbert*, 1971], the study of Q_α from short-period body wave observations had already suggested that Q_α is extremely low near the Inner Core Boundary (ICB) and increases with depth [*Sacks*, 1969]. This implies the existence of a mushy zone with partial melting at the top of the inner core [*Doornbos*, 1974; *Loper & Fearn*, 1983].

Since then, studies of Q_α based on both short-period and broadband data have presented evidence in support of this model (e.g., [*Souriau & Roudil*, 1995; *Li & Cormier*, 2002]) and revealed more complex attenuation structure in the inner core [*Souriau & Romanowicz*, 1996; *Cao & Romanowicz*, 2004b; *Cormier and Li*, 2002]. Similar to the P-wave velocity anisotropy [*Morelli et al.*, 1986; *Woodhouse et al.*, 1986], Q_α may be also anisotropic [*Souriau & Romanowicz*, 1996]. The partial melting mushy zone may be confined to the uppermost inner core [*Cao & Romanowicz*, 2004b]. At the top $\sim 85km$ of the inner core, Q_α shows a remarkable hemispherical distribution and Q_α first decreases from the Inner Core Boundary (ICB) and then increases with depth. Both scattering related with iron crystal texturing and diffusion related to

liquid inclusions can account for the Q_α increase with depth [*Cormier and Li*, 2002; *Singh et al.*, 2000]. As for which is the dominant factor, it may depend on the depth range of study.

While significant progress has been made in the study of Q_α in the inner core using body wave observations, the shear wave quality factor, Q_β, is still estimated only from a few normal mode measurements [*Dziewonski & Anderson*, 1981; *Widmer et al.*, 1991]. The constraint of Q_β from shear body waves in the inner core (e.g., PKJKP and SKJKP) has never been documented. The inner core shear waves are very difficult to detect due to the poor efficiency of phase conversion at ICB and the strong attenuation through the inner core [*Deuss et al.*, 2000]. Thus, a reliable inner core shear waveform, which is essential to constrain Q_β from body waves, has not been observed until recently.

Taking advantage of high quality broadband seismic array data, we presented a reliable PKJKP phase (Fig. 6.1) with a clear waveform [*Cao et al.*, 2005]. Four kinds of different evidence (arrival time, slowness, back-azimuth, and comparison with a quasi-liquid inner core model) were provided jointly to support our PKJKP observation. In this paper we make an attempt, for the first time, to constrain Q_β directly using a PKJKP waveform.

6.2   Data, Method, and Results

The Gräfenberg Array (GRF), founded in the early 1970's, is the first digital broadband seismic array in the world (with an aperture of ~ 100km x 50km) (Fig. 6.2a). It provides continuous high quality records at all 13 stations since 1980. Frequent large events ($M_w > 7.0$) which occur in the south Pacific Ocean at distance around 140° make it an ideal broadband seismic array to study PKJKP (Fig. 6.2b). We systematically examined those large events which occurred from 1980 to 1999, during which the relocated catalog by *Engdahl et al.* [1998] is available. There are approxi-

mately 20 large events which occurred in the vicinity of Tonga and Santa Cruz islands in this time interval. One of them (Mw=7.3, depth=76 km, 02/06/1999) turned out to be particularly suitable for the detection of PKJKP (Fig. 6.2c,d) using data from GRF [*Cao et al.*, 2005].

6.2.1   Observation of PKJKP

The details of the data processing were given in [*Cao et al.*, 2005]. Here we only summarize them briefly. We align seismograms with respect to the origin time of the event after making an array-sided travel time correction (Fig. 6.3a). After band-pass filtering (2-poled Butterworth) the seismograms in the frequency band 0.06-0.1 Hz (Fig. 6.3b), normalizing with respect to the first arrival (PKIKP+PKiKP), and stacking using the Phase Weighted Stack (PWS) technique [*Schimmel & Paulssen*, 1997], we observed a PKJKP phase, for which three kinds of evidence (travel time, slowness, and back-azimuth) were provided (Fig. 6.4a,c). The fourth evidence which ruled out the possibility for it to be an outer core, mantle, or crust phase, was presented (Fig. 6.4d) using synthetic seismograms computed using the DSM method [*Takeuchi et al.*, 1996]. The completeness of synthetic seismograms is required. All the synthetic codes which are based on the specification of ray paths are not suitable. The Direct Solution Method (DSM) computes the displacement directly from the Galerkin weak form of the elastic equation of motion [20], so it can be used to generate highly accurate and complete synthetic seismograms [*Geller & Ohminato*, 1994].

The event occurred in the slab of the Santa Cruz Islands subduction zone. Depth phases pPKIKP+pPKiKP and pPKJKP are reflected from the oceanic floor, and their distances are less than 12 km. This requires us to take both a magma wedge and an oceanic layer into account in the near source region. In a magma wedge,

quality factors for both compressional and shear waves are thought to be extremely low (approximately 50 and 20, respectively) [*Barazangi & Isacks*, 1971]; in an oceanic layer, part of the energy of reflected phases leaks into the water. The consideration of these two aspects allows us to successfully model both the waveform of PKIKP+PKiKP and its depth phase, pPKIKP+pPKiKP (Fig. 6.5a), using the moment tensor from the PDE bulletin of the National Earthquake Information Center (http://neic.usgs.gov/neis/sopar/) and the source time function (Fig. 6.2c) obtained from the P phase observed at a GSN broadband station (YAK, distance = 80.1^o) which has a similar backazimuth as GRF.

It is impossible to discern PKJKP in an individual synthetic trace because PKJKP is so weak that it is deeply hidden behind unidentifiable mantle, outer core, and (or) crust phases. In order to extract PKJKP prominently, we introduced a pseudo-liquid inner core model [*Cao et al.*, 2005], in which the shear wave velocity in the inner core is 8% less than that in the reference mode PREM [*Dziewonski & Anderson*, 1981]. We computed synthetic seismograms for both solid and pseudo-liquid inner cores based on the same geometry for the event and the seismic array. In the resulting differential seismogram we may clearly see PKJKP (Fig. 6.5b).

6.2.2 Constraints on Q_β in the inner core

The clear observed and synthetic PKJKP waveforms (Fig. 6.4b, 6.5b) look suitable to constrain the shear wave attenuation in the inner core directly by waveform modeling. However, heterogeneity in the mantle can give rise to the dispersion and phase shift of the waveform. Thus we choose to model the envelope function rather than directly the waveform. In general, the envelope function can characterize the amplitude and arrival time of the energy maximum better than the waveform.

On the other hand, the synthetic vespagram for the pseudo-liquid inner core (Fig. 6.4d) indicates that we cannot directly use the synthetic envelope function to constrain the shear wave attenuation in the inner core. In the time window of interest (Fig. 6.4d), sPcPPKIKP (predicted slowness and arrival time are 1.93 s/deg and 1674 s, respectively) and pPcPPKIKP (predicted slowness and arrival time are 1.93 s/deg and 1665 s, respectively) should have appeared. But relatively strong synthetic mantle phase (A in Fig. 6.4d), whose slownesses are $\sim 8.0 s/deg$, arrive at the same time. The consequence is that only the dominant energy is apparent in the vespagram. The synthetic phase B (Fig. 6.4a) arrives at almost the same time as the predicted PKJKP. Therefore, it is not possible to obtain a reliable synthetic envelope function for PKJKP from the synthetic seismograms generated for a solid inner core. However, we can directly use the envelope function of PKJKP in the synthetic differential seismogram between the solid inner core and the pseudo-liquid inner core, where mantle phases are removed, to constrain the Q_β in the inner core.

In order to estimate the standard deviation of the observed PKJKP envelope, we repeat the envelope calculation with subsets of the GRF array. During this process, up to two stations are removed, but the two stations are required to be from different subarrays (Fig. 6.2). Clear PKJKP waveforms can be seen for ~ 60 subsets of data after stacking. In principle, the envelope should not change with respect to any phase shift of the waveform. We use this criterion to further examine the stability of the stacked PKJKP waveforms. Two envelopes are computed for every stacked PKJKP waveform, one for itself and the other for its Hilbert transform (90° phase shift). In most cases the two envelopes are very close (amplitude variation less than 20%). Our final envelope mean and the standard deviation (Fig. 6.6) are calculated based on these stable envelopes.

We process the synthetic differential seismograms in the same way as the observed seismogram. Based on the stacked seismogram of the synthetic PKJKP, we perform the envelope function modeling (Fig. 6.7). According to the standard deviation of the observed PKJKP envelope, the estimated Q_β in the inner core is in the range of

~ 230 to ~ 400. When we assume that Q_β is ~ 315, the envelope amplitudes of the observed PKJKP and the synthetic PKJKP are comparable. As pointed out before [*Cao et al.*, 2005], the envelope function modeling also suggests that the observed PKJKP is about 9.0 seconds faster than the synthetic PKJKP (Fig. 6.7, 6.8). This means that the constrained shear wave velocity in the inner core is $\sim 1.5\%$ faster than that for the PREM model. If we allow the shear wave velocity increases towards the center of the inner core, the constrained velocity seems compatible with that in PREM model.

6.3 Discussion

Due to the strong attenuation and poor phase conversions in the inner core, we need to select large earthquakes to search for inner core shear waves. The two events used in the previous two studies [*Deuss et al.*, 2000; *Okal & Cansi*, 1998] are both around Mw 8.0. However, their corresponding source time durations are also much longer (approximately 20 and 40 seconds [*Goes et al.*, 1997]), and so the chance for PKJKP and pPKJKP to interfere with other phases are also higher. Thus, it is better to find an event which can balance the magnitude and the source duration.

Large events usually have large rupture lengths and strong directivity. This may result in significant error for the direct estimation of Q_β in the inner core using the absolute envelope modeling of PKJKP. In order to control the influence of the directivity of the rupture as well as the uncertainty in the moment tensor, we normalize observed seismograms and synthetic seismograms with respect to the first waveform (PKIKP+PKiKP), respectively. The difference of take-off angles between PKJKP and PKIKP (or PKiKP) is only about 8 degrees (Fig. 6.2d). We may expect the directivity of the rupture to affect PKJKP and PKIKP in almost the same way.

The envelope function of the observed PKJKP is narrower than that of the synthetic PKJKP (Fig. 6.7). This is related to the background noise in the GRF seismic array. The existence of the incoherent noise can make the waveform narrower after non-linear stacking [*Schimmel & Paulssen*, 1997]. In order to have a further quantitative understanding, we conduct background noise experiments (Fig. 6.8, 6.9). Realistic seismic noise is taken from time windows of 200 to 400 seconds before the first arrivals in the individual observed traces. Synthetic PKJKP phases are computed from differential seismograms, with the noise added, before computing envelope. Our results show that the lower the original amplitude, the more influenced by the background noise after stacking. In the synthetic differential seismogram, pPKJKP is ~ 2.2 times weaker than PKJKP (Fig. 6.5b). The experiment (Fig. 6.8) indicates that the amplitude ratio of PKJKP to pPKJKP may be as large as ~ 4.8 if we take the background noise into account. Therefore, it is not surprising that we do not observe pPKJKP for this event (Fig. 6.4a).

In the case of the background noise Level 2 (Fig. 6.9), we may readily note that the envelope for $Q_\beta = 85$ in PREM decreases more than 10 times compared with that in Fig. 6.7. Whereas the envelope for $Q_\beta = 400$ only barely decreases (~ 1.0 percent). Our experiments demonstrate that the presence of background noise would make the PKJKP amplitude smaller in the realistic observation. This implies that Q_β in the inner core based on the envelope function modeling (Fig. 6.7) is under-estimated. In spite of this, we can still see that the envelope for the observed shear body wave PKJKP is significantly larger (> 3.5 times) than that for the upper bound of the estimate of Q_β (< 150) from normal mode observations [*Widmer et al.*, 1991] (Fig. 6.9). If taking account of the uncertainty in the amplitude spectrum within the range of our study (Fig. 6.3b), the lower bound of our Q_β estimate might be tuned as low as ~ 165. But, as discussed above, this value should be more under-estimated than the mean value ($Q_\beta = \sim 315$).

6.4   Conclusion

Our constraint on Q_β in the inner core suggests a significantly higher value than that observed from normal mode measurements [*Dziewonski & Anderson*, 1981; *Widmer et al.*, 1991]. The normal modes, which are sensitive to the shear wave structure in the inner core, mainly sample the shallow portion of the inner core. Whereas PKJKP (and pPKJKP) samples most of the inner core deep into the center (Fig. 6.1) Thus, we find that Q_β increases with depth in the inner core, just as Q_α does [*Souriau & Roudil*, 1995].

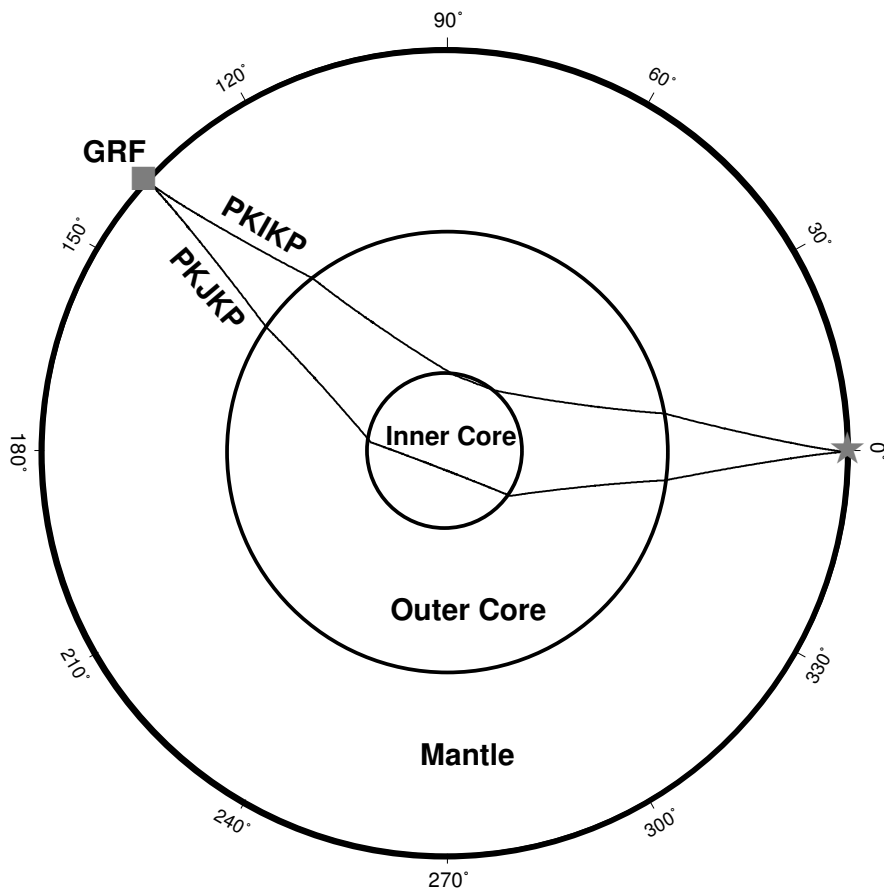Figure 6.1: (a) Ray paths of PKJKP and PKIKP. The event source and GRF seismic array are indicated by a star and a square, respectively.
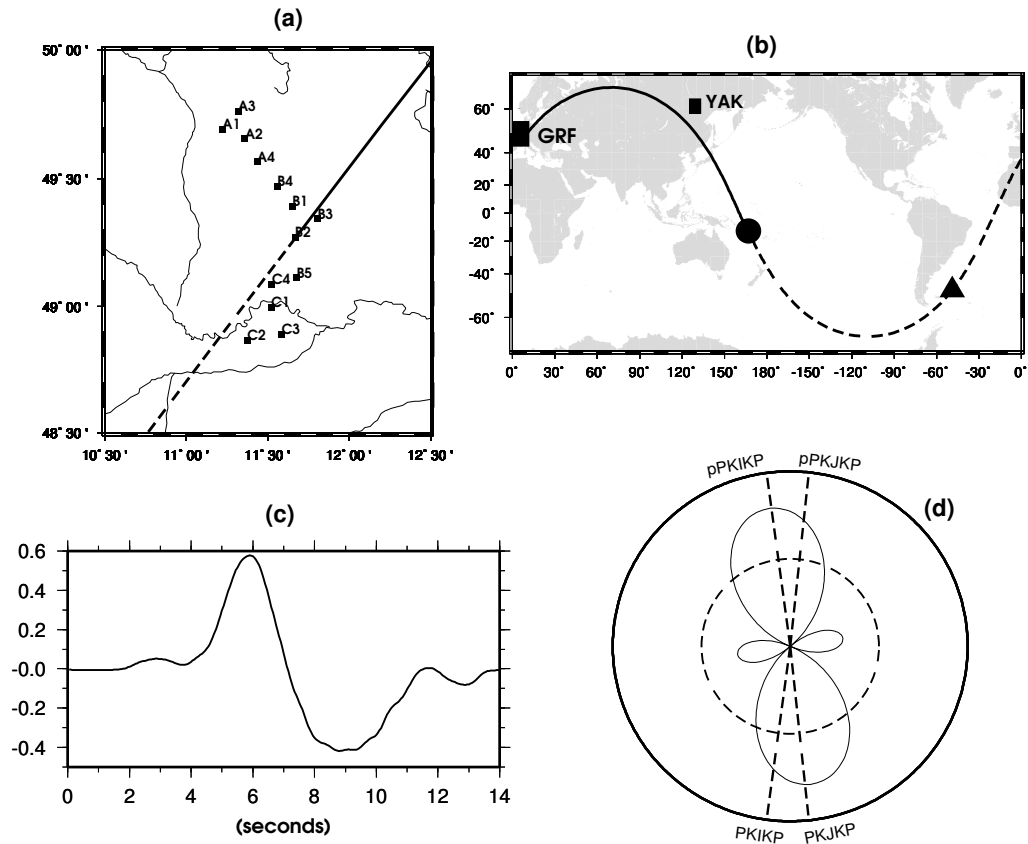
(a)

(b)

(c)

(d)

Figure 6.2: (a)Subarrays of the broadband GRF seismic array. The central station, GRB2, is chosen as the reference station for the PWS stacking. (b) Geographical map with the event (dot), GRF seismic array (square), PKIKP, and PKJKP raypaths. The triangle is the location of the PKJKP bottoming point in the inner core. (c) Source time history of the event illustrated by a P wave recorded at the GSN station YAK ($\Delta = 80.1^o$), located in a close azimuth as GRF. The source time duration is less than 9 seconds. (d) P wave radiation pattern in the vertical plane of the great circle. The expected PKJKP is emitted from the top of the lobe.
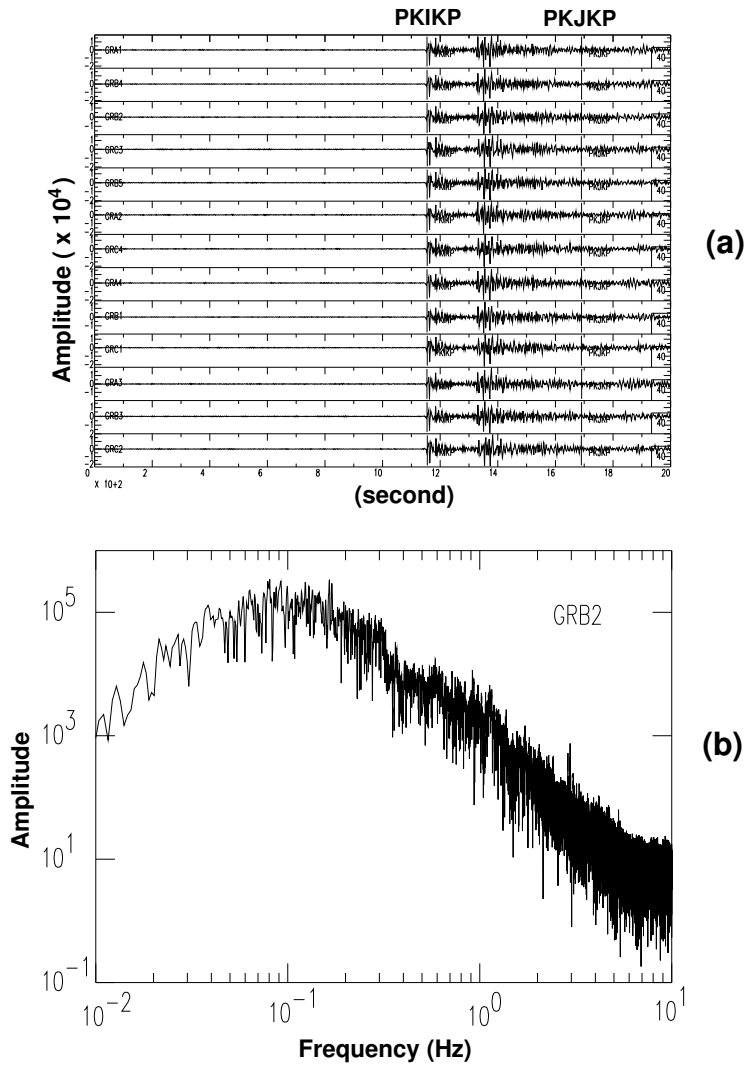
Figure 6.3: (a) Vertical component raw traces of this event recorded at the stations of GRF array. The time window starts at the origin time of the event. (b) An example of amplitude spectrum. It is computed using a time window from 100 seconds before PKIKP to 200 seconds after PKJKP. In the frequency range of 0.06 to 0.1 Hz, the amplitude is almost constant, so we choose this frequency range in our study.
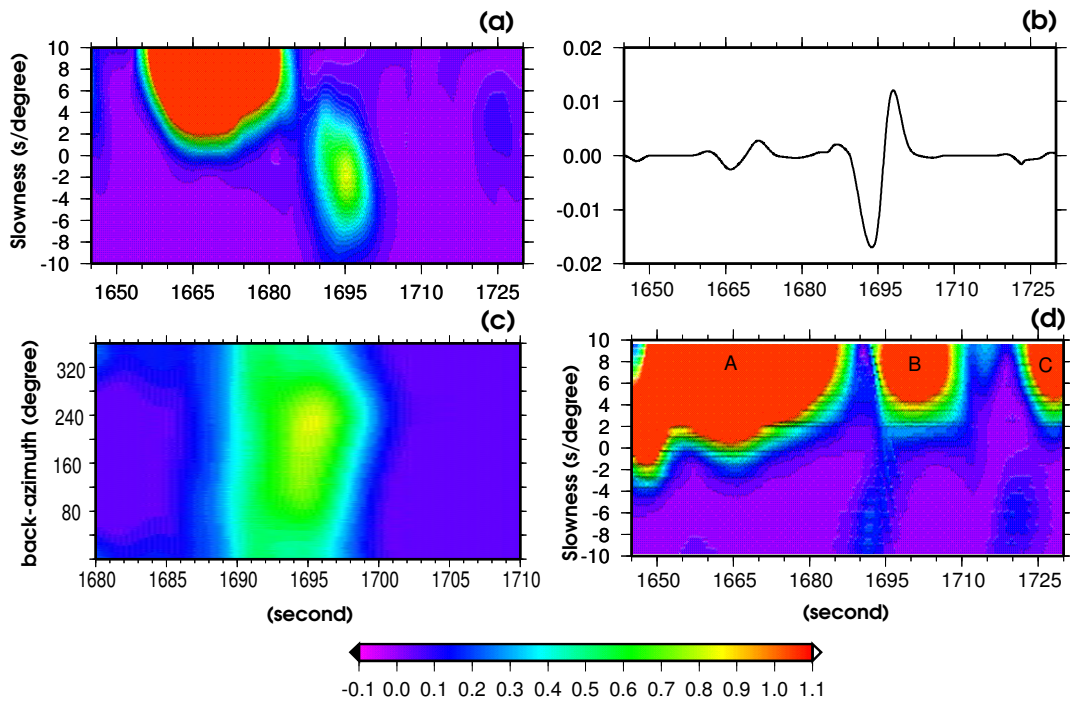
Figure 6.4: Evidence for the observation of PKJKP. (a) Observed vespagram for PKJKP in the slowness and travel time domain. The energy level is amplified 40 times. The slowness of the energy maximum is $\sim -1.6s/deg$, close to the PREM prediction of -1.43 s/deg. The arrival time is also compatible with PREM (1695 sec for the maximum energy, compared to a prediction of 1690 sec for the high frequency onset of the pulse). (b) Stacked waveform corresponding to the energy maximum in (a). (c) Observed vespagram in the back-azimuth and travel time domain. showing the direction of the PKJKP arrival. The estimated back-azimuth is $\sim 223^{o}$, which shows that the observed PKJKP propagates along the major arc from the source (the expected back-azimuth of PKJKP is 218.º). (d) Synthetic vespagram for the pseudo-liquid inner core model. In the negative slowness region there is no energy maximum corresponding to the observation in (a). This means that the observed phase in (a), (b), and (c) is not an outer core, mantle, or crust phase.
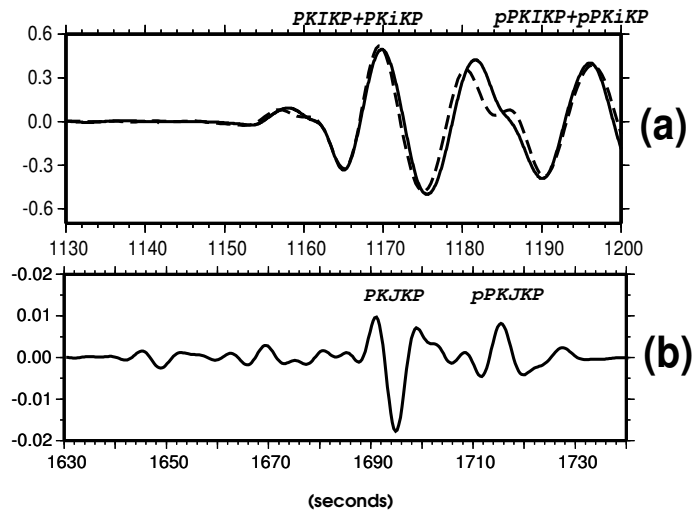
Figure 6.5: Synthetic modeling. (a) Waveform modeling of PKIKP+PKiKP as well as pPKIKP+pPKiKP using DSM [19]. The moment tensor is from PDE catalog of the National Earthquake Information Center. Both observed (dashed line) and synthetic (solid line) seismograms are normalized after applying the bandpass filter (2-poled Butterworth with corner frequencies 0.06-0.1 Hz). (b) PKJKP and pPKJKP in the synthetic differential seismogram between solid and pseudo-liquid inner core models. Here Q_α in the solid inner model is assumed as 300.
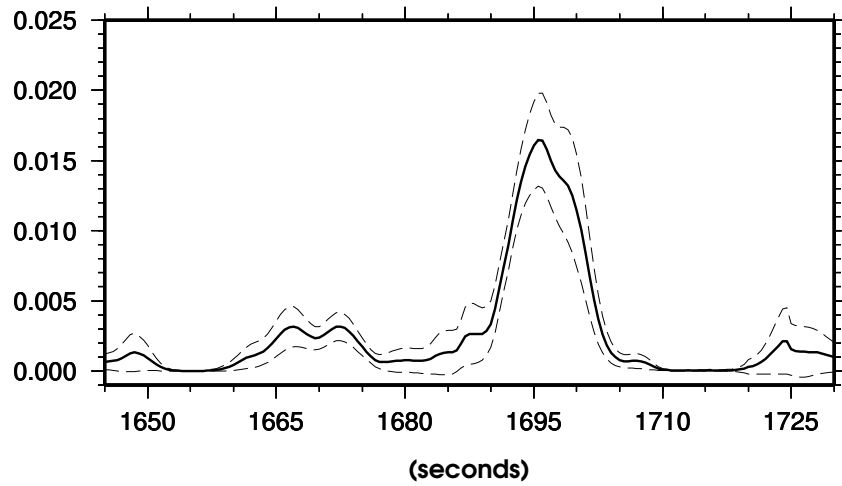
Figure 6.6: Uncertainty of the observed PKJKP envelope. The solid line denotes the mean of envelopes calculated using the subsets of the observed records. Two dashed lines demonstrate the range of the standard deviation.
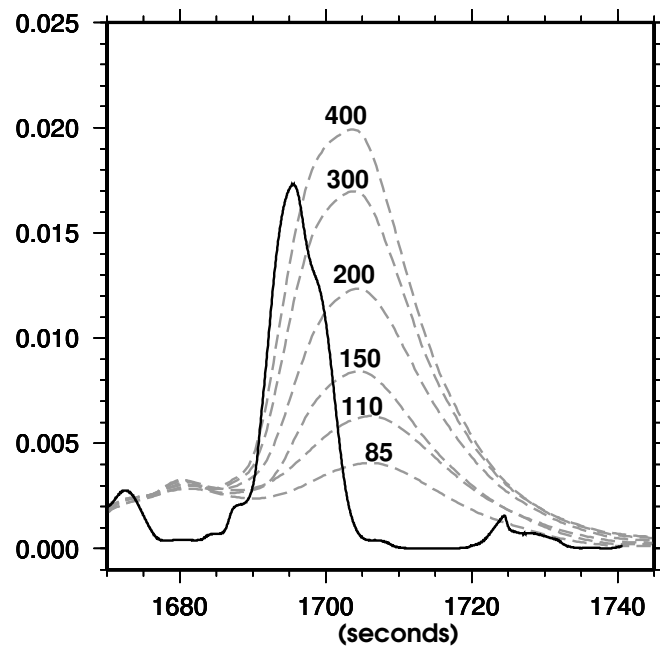
Figure 6.7: Envelope function modeling. The solid black line corresponds to the observed PKJKP, and dashed lines denote synthetic PKJKP with respect to different shear wave quality factors assumed in the inner core.
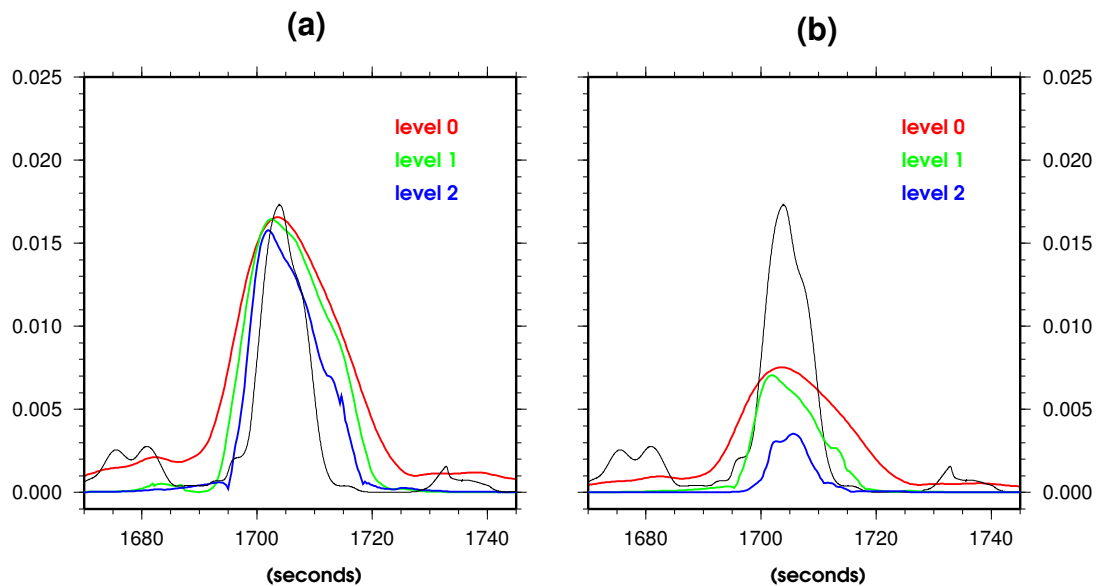
Figure 6.8: Influence of noise on the determination of Q_β using the PWS stack envelopes. The black lines are the observed envelopes (shifted 9 s backwards). Level 0: no seismic noise is added to synthetic PKJKP traces; Level 1: the original strength of seismic noise is added; Level 2: the strength of seismic noise is amplified twice before being added to the individual traces. (a) Here the model Q_β is assumed to be 300. The estimated Q_β for the envelope function Level 0 is 300; estimated Q_β for Level 1 is ~ 295; estimated Q_β for Level 2 is ~ 280. (b) Here the model Q_β is assumed to be 150. the estimated Q_β for Level 0 is 150; estimated Q_β for Level 1 is ~ 140; and estimated Q_β for Level 2 is ~ 80. The original amplitude in panel (a) is ~ 2.2 times larger than in panel (b).
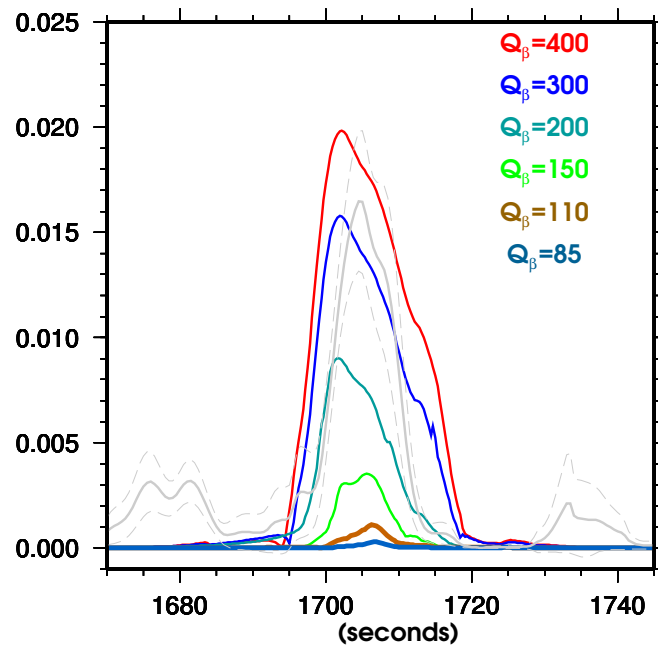
Figure 6.9: Comparison of the synthetic and observed envelopes after stacking. The background noise Level 2 is taken into account. The color lines are the synthetic envelopes with a series of assumption of Q_β in the inner core, in which $Q_\beta = 85$ [13] and $Q_\alpha = 110$ [14] are the estimates based on normal mode observations. The grey solid and dashed lines denote the observed envelope and its corresponding standard deviation range (shifted 9 s backwards).

Chapter 7

Conclusions

We discussed the inner core solidity from different angles: the density jump at the Inner Core Boundary, the soft mushy layer at the top, the direct evidence PKJKP, and the shear wave attenuation. The results gave us significant insight into the dynamic processes of the inner core.

We revisited the issue of density contrast ($\Delta\rho$) at the ICB by means of PKiKP/PcP amplitude ratio in the epicentral distance range of $10 - 70^o$. Based on our high quality observations of pairs of PKiKP and PcP, we obtained the estimates of $\Delta\rho$ in the range $0.6 - 0.9 g/cm^3$ and ΔV_β in the range of $2 - 3km/s$ with respect to different reference seismic models. Our estimate of $\Delta\rho$, together with a recent re-evaluation by normal mode observations [*Masters & Gubbins*, 2003] reconciled the long-term discrepancy from body wave and mode studies, and provided a tighter constraint on $\Delta\rho$ at the ICB for geodynamo studies. Meanwhile, our estimate of ΔV_β suggested a lower shear wave velocity jump at the ICB than that in PREM, which is consistent with our observed soft mushy layer at the top of the inner core.

Based on our P-wave attenuation study, we confirmed the existence of a soft mushy layer at the top of the solid inner core. Further, we showed that this mushy layer

should be well confined to the top $\sim 85km$ of the inner core. To accompany this mushy layer, we observed the attenuation transition in the western hemisphere of the inner core, where Q_α decreases first with depth from the ICB and then turns to increase at the depth of $\sim 85km$. We did not observe the attenuation transition in the eastern hemisphere, but we inferred that it exists in the top $\sim 32km$ beneath the ICB. In addition, our measurement of differential travel time residuals of PKiKP and PKIKP also confirmed the existence of a hemispherical pattern of the isotropic P-wave velocity at the top of the inner core. High Q_α and low velocity are present in the western hemisphere, and low Q_α and high velocity in the eastern hemisphere. This kind of hemispherical pattern may be related to the small variation of temperature at the top of the inner core and their influence on the morphology of porosity and connectivity of liquid inclusions in the mushy zone.

The observation of PKJKP provided the direct evidence for the solidity of the inner core. Our results clearly demonstrate the difficulty of this task. First of all, a high quality broadband seismic array is necessary. Due to the strong shear wave attenuation in the inner core, only in the low frequency range is it possible to detect PKJKP. Second, a good combination of epicentral distance and event depth is necessary. This guarantees that the potential interfering phases are far enough away from the elusive PKJKP. Third, the balance between the event magnitude and duration is important. A strong event ($M_w > 7.0$) but with a short source time history (less than 10 seconds) would be a good candidate. Fourth, the broadband seismic array should have an ideal aperture. If it is too small, the slowness resolution is very poor; if it is too big, the number of the potential interfering phases increases significantly. Finally, the joint provision of arrival time, slowness, back-azimuth, and comparison with a 'liquid' inner core model is indispensable. Especially, any lack of one of least two evidence would likely result in the misidentification of PKJKP.

Our observed high signal-to-noise PKJKP waveform made it possible to constrain the inner core shear wave properties by means of envelope modeling. For the shear wave velocity, it is suggested that the observed PKJKP is $\sim 9.0s$ faster than the synthetic

PKJKP. This means the shear-wave velocity in the inner core is $\sim 1.5\%$ faster than that in the reference model PREM. For the shear wave attenuation, it is suggested that the Q_β is significantly larger than that from normal mode observations. Q_β is well constrained to be larger than ~ 150 (compared to 85 for the reference PREM model) and our best estimate is $Q_\beta \sim 315 \pm 150$. Because PKJKP samples the deep inner core, whereas the PREM estimate is based on normal mode data which have sensitivity primarily to the top of the inner core, this indicates increases of V_β and Q_β with depth in the inner core. The increase of Q_β with depth is in agreement with what is generally observed for Q_α.

Our PKJKP studies provide a new perspective to discuss the inner core anisotropy in the future. If the anisotropy does exist, an independent evidence can be obtained from the inner core shear wave PKJKP (or SKJKP) according to *Stixrude and Cohen*'s (1995) study. They pointed out that the fast direction of inner core shear waves may be 45° between the earth's rotation axis and the equatorial plane. This is very different from P-wave's fast direction (along polar paths). Meanwhile, based on their study, it can be readily inferred that inner core shear waves may be up to 50 seconds faster along the fast direction than along the slow direction, which are much longer than the observed ~ 7 seconds for the P-wave anisotropy. Thus, it looks like inner core shear waves might demonstrate the inner core anisotropy better than inner core P-waves. More PKJKP (or SKJKP) observations from other broadband seismic arrays around the world will be very useful.

Bibliography

Aki, K. and P.G. Richards, Quantitative seismology, *Freeman and company*, 1980.

Aki, K. and P.G. Richards, Quantitative seismology, *University Science Books*, 2002.

Backus, G.E., Gross thermodynamics of heat engines in deep interior of Earth, *Nat. Acad. Sci. USA*, **72**, 1555-1558, 1975.

Barazangi, M. and B. Isacks, Lateral variation of seismic-wave attenuation in the upper mantle above the inclined earthquake zone of the Tonga Island arc: Deep anomaly in the upper mantle. *J. Geophys. Res.*, **76**, 8493-8516, 1971.

Beghein, C. and J. Trampert, Robust normal mode constraints on inner core anisotropy from model space search, *Science*, **299**, 552-555, 2003.

Ben-Menahem, A. and S.J. Singh, Seismic waves and sources, *Springer-Verlag*, 1981.

Bergman, M.I., Solidification of the Earth's Core, in: V. Dehant, K.C. Creager, S. Karato, S. Zatman (Ed.), Earth's Core: Dynamics, Structure, Rotation, *AGU Geodynamics Series*, **31**, 105-127, 2002.

Bhattacharyya, J., P. Shearer, and G. Masters, Inner core attenuation from sort period PKP(BC) versus PKP(DF) waveforms, *Geophys. J. Int.*, **114**, 1-11, 1993.

Birch, F., The alpha-gamma transformation of iron at high compressionals and the problem of the Earth's magnetism, *Am. J. Sci.*, **238**, 192, 1940.

Birch, F., Density and composition of the mantle and core, *J. geophys. Res.*, **69**, 4377-4388, 1964.

Bolt, B.A. and A. Qamar, Upper bound to the density jump at the boundary of the Earth's inner core, *Nature*, **228**, 148-150, 1970.

Bolt, B.A., The detection of PKIIKP and damping in inner core, *Ann. Geofis.*, **30**, 507-520, 1977.

Braginsky, S.I., Structure of the F layer and reasons for convection in the earth's core, *Dokl. Acad. Sci. USSR., Engl. Transl.*, **149**, 8-10, 1963.

Breger, L., H. Tkalcic, and B. Romanowicz, The effect of D" on PKP(AB-DF) travel time residuals and possible implications for inner core structure, *Earth Planet. Sci. Lett.*, **175**, 133-143, 2000.

Buffett, B.A., H.E. Huppert, J.R. Lister, and A.W. Woods, On the thermal evolution of the Earth's core, *J. Geophys. Res.*, **101**, 7989-8006, 1996.

Bullen, K.E., An introduction to the theory of seismology, *Cambridge university press*, 1963.

Bullen, K.E. and B.A. Bolt, An introduction to the theory of seismology, *Cambridge university press*, 1985.

Cao, A., B. Romanowicz, and N. Takeuchi, An observation of PKJKP: Inferences on inner core shear properties, *Science*, **308**, 1453-1455, 2005.

Cao, A. and B. Romanowicz, Constraints on Shear Wave Attenuation in the Earth's Inner Core from an observation of PKJKP *Earth planet. Sci. Lett.*, submitted.

Cao, A. and B. Romanowicz, Constraints on density and shear velocity contrasts at the inner core boundary, *Geophys. J. Int.*, **157**, 1146-1151, 2004.

Cao, A. and B. Romanowicz, Hemispherical transition of seismic attenuation at the top of the Earth's inner core, *Earth planet. Sci. Lett.*, **228**, 243-253, 2004.

Choy, G.L., and V.F. Cormier, The structure of the inner core inferred from short-period and broadband GDSN data, *Geophys. J. R. astr. Soc.,* 21-29, 1983.

Hewitt, J.M., D.P. McKenzie, and N.O. Weiss, Dissipative heating in convective flows, *J. Fluid Mech.*, **68**, 721-738, 1975.

Cormier, V.F. and P.G. Richards, Comments on 'The damping of the core waves' by Antony Qammar and Alfredo Eisenberg, *J. geophys. Res.*, **981**, 3066-3068, 1976.

Cormier, V.F. and G.L. Choy, A search for lateral heterogeneity in the inner core from differential travel ti mes near PKP-D and PKP-C, *Geophys. Res. Lett.*, **13**, 1553-1556, 1986.

Cormier, V.F. and X. Li, Frequency-dependent seismic attenuation in the inner core 2. A scattering and fabric interpretation, *J. Geophys. Res.*, **107**, 2362, 2002.

Creager, K.C., Large-scale variations in inner core anisotropy, *J. Gephys. Res.*, **104**, 23127-23139, 1999.

Cummins, P., and L.R. Johnson, Short-period body wave constraints of properties of the Earth's inner core boundary, *J. Geophys. Res.*, **93**, 9058-9074, 1988.

Deuss, A., J.H. Woodhouse, H. Paulssen and J. Trampert, The observation of inner core shear waves, *Geophys. J. Int.*, **142**, 67-73, 2000.

Doornbos, D.J., The anelasticity of the inner core, *Geophys. J. R. astr. Soc.*, **38**, 397-415, 1974.

Dziewonski, A.M. and F. Gilbert, Solidity of the inner core of the Earth inferred from normal mode observations, *Nature*, **234**, 465-466, 1971.

Dziewonski, A.M., and F. Gilbert, The effect of small, aspherical perturbations on travel times and a re-examination of the corrections for ellipticity, *Geophys. J. R. Astron. Soc.*, **44**, 7-17, 1976.

Dziewonski, A.M. and D.L. Anderson, Preliminary reference earth model, *Phys. Earth planet. Inter.*, **25**, 297-356, 1981.

Earle, P.S. and P.M. Shearer, Observations of PKKP precursors used to estimate small-scale topography on the core-mantle boundary, *Science*, **277**, 667-670, 1997.

Engdahl, E.R., E.A. Flinn and C.F. Romney, Seismic waves reflected from the Earth's inner core, *Nature*, **228**, 852-853, 1970.

Engdahl, E.R., R.D. van der Hilst and R.P. Buland, Global teleseismic earthquake relocation with improved travel times and procedures for depth determination, *Bull. Seism. Soc. Am.*, **88**, 722-743, 1998.

Fearn, D.R., D.E. Loper, and P.H. Roberts, Structure of the Earth's inner core, *Nature*, **292**, 232-233, 1981.

Finlayson, B.A., The method of weighted residuals and variational principles, *Academic Press*, New York, 1972.

Garcia, R. Constraints on upper inner-core structure from waveform inversion of core phases, *Geophys. J. Int.*, **150**, 651-664, 2002.

Geller, R.J. and T. Ohminato, Computation of synthetic seismograms and their partial derivatives for heterogeneous media with arbitrary natural boundary conditions using the Direct Solution Method (DSM), *Geophys. J. Int.*, **116**, 421-446, 1994.

Gilbert, F., A.M. Dziewonski, and J.N. Brune, An informative solution to a seismological inverse problem, *Proc. Natl. Acad. Sci.*, **70**, 1410-1413, 1973.

Gilbert, F., and A.M. Dziewonski, A.M., An application of normal mode theory to the retrieval of structural parameters and source mechanisms from seismic spectra. *Phil. Trans. R. Soc. Lond.*, bf A278, 187-269, 1975.

Goes, S., L. Ruff and N. Winslow, The complex rupture process of the 1996 deep Flores, Indonesia earthquake (Mw 7.9) from teleseismic P-waves, *Geophys. Res. Lett.*, **24**, 1295-1298, 1997.

Gubbins, D., Energetics of the Earth's core, *J. Geophys.*, **43**, 453-464, 1977.

Gubbins, D., T.G. Masters, and J.A. Jacobs, Thermal evolution of the Earth's core, *Geophys. J. R. Astron. Soc.*, **59**, 57-99, 1979.

Gubbins, D., D. Alfe, G. Masters, G.D. Price, and M.J. Gillan, Can the Earth's dynamo run on heat alone? *Geophys. J. Int.*, **155**, 609-622, 2003.

Hage, H., Velocity constraints for the inner core inferred from long-period PKP amplitudes, *Phys. Earth Planet. Inter.*, **31**, 171-185, 1983.

Hedlin, M.A.H., P.M. Shearer, P.S. Earle, Waveform stacks of PKP precursors: evidence for small-scale heterogeneity throughout the mantle, *Nature*, **387**, 145-150, 1997.

Ishii, M., A.M. Dziewonski, J. Tromp, and G. Ekstrom, Joint inversion of normal mode and body wave data for inner core anisotropy 2, Possible complexities, *J. Geophys. Res.*, **107**, 2380, 2002.

Jacobs, J.A., The earth's inner core, *Nature*, **172**, 297, 1953.

Jeffreys, H., The Eearth; it origin, history, and physical construction, *Cambridge University Press*, 1924.

Julian, B.R., D. Davies and R.M. Sheppard, PKJKP, *Nature*, **235**, 317-318, 1972.

Kennett, B.L.N. and E.R. Engdahl, Travel times for global earthquake location and phase identification, *Geophys. J. Int.*, **105**, 429-465, 1991.

Kennett, B.L.N., E.R. Engdahl, and R. Buland, Constrains on seismic velocities in the Earth from travel times, *Geophys. J. Int.*, **122**, 108-124, 1995.

Labrosse, S., J.P. Poirier, and J.L. LeMouel, On cooling of the Earth's core, *Phys. Earth Planet. Int.*, **99**, 1-17, 1997.

Lay, T. and T.C. Wallace, Modern global seismology, *Academic press*, 1995.

Lehmann, I., P', *Bur. Centr. Seismol. Int. A., Travaux Scientifiques*, **14**, 87-115, 1936.

Li, X. and V.F. Cormier, Frequency-dependent seismic attenuation in the inner core 1. A viscoelastic interpretation *J. Geophys. Res.*, **107**, 2361, 2002.

Loper, D.E., The gravitationally powered dynamo, *Geophys. J. R. astr. Soc.*, **54**, 389-404, 1978.

Loper,D.E. and D.R. Fearn, A seismic model of partially molten inner core, *J. Geophys. Res.*, **88**, 1235-1242, 1983.

Loper, D.E., The nature and consequences of thermal interactions twixt core and mantle, *G. Geomagn. Geoelectr.*, **43**, 79-91, 1991.

Masters, G., Observational constraints on the chemical and thermal structure of the earth's deep interior, *Geophys. J. R. Astron. Soc.*, **57**, 507-534, 1979.

Masters, G. and D. Gubbins, On the resolution of density within the Earth, *Phys. Earth. planet. Int.*, **140**, 159-167, 2003.

McElhinny, M.W., and W.E. Senanayake, W.E., Paleomagnetic evidence for the existence of the geomagnetic field 3.5Ga ago, *J. Geophys. Res.*, **85**, 3523-3528, 1980.

McSweeney, T.J., K.C. Creager, R.T. Merrill, Depth extent of inner-core seismic anisotropy and implications for geomagnetism, *Phys. Earth Planet. Inter.*, **101**, 131-156, 1997.

Mollett, S.,Thermal and magnetic constraints on the cooling of the Earth, *Geophys. J. R. Astron. Soc.*, **76**, 653-666, 1984.

Morelli, A., A.M. Dziewonski, and J.H. Woodhouse, Anisotropy of the inner core inferred from PKIKP trave times, *Geophys. Res. Lett.*, **13**, 1545-1548, 1986.

Muirhead, K.J., Eliminating false alarms when detecting seismic events automatically, *Nauter*, **217**, 533-534, 1968.

Niu, F. and L. Wen, Hemispherical variations in seismic velocity at the top of the Earth's inner core, *Nature*, **410**, 1081-1084, 2001.

Oldham, R.D., The constitution of the interior of the Earth as revealed by earthquakes, *J. geol. Soc. Lond.*, **62**, 456-475, 1906.

Okal, E.A. and Y. Cansi, Detection of PKJKP at intermediate periods by progressive multi-channel correlation, *Earth planet. Sci. Lett.*, **164**, 23-30, 1998.

Oreshin, S.I. and L.P. Vinnik, Heterogeneity and anisotropy of seismic attenuation in the inner core, *Geophys. Res. Lett.*, **31**, L02613, 2004.

Romanowicz, B., H. Tkalcic, and L. Bréger, On the origin of complexity in PKP travel time data from broadband records, in Earth's Core: Dynamics, Structure, Rotation, V. Dehant and K. Creager Eds, *AGU Geodynamics Series*, **31**, 31-44, 2002.

Sacks, I.S., Anelasticity of the inner core, in *Carnegie Institution Year Book*, **69**, 416-419, 1969.

Schimmel, M. and H. Paulssen, Noise reduction and the detection of weak, coherent signals through phase-weighted stacks, *Geophys. J. Int.*, **130**, 497-505, 1997.

Schweitzer, PKiKP and PcP observations of the Chinese Nuclear Test on May 21, 1992 05:00 UTC, *Eos. Trans. Am. Geophys. Union,* 408, 1992.

Shearer, P.M., and G. Masters, The density and shear velocity contrast at the inner core boundary, *Geophys. J. Int.*, **102**, 491-498, 1990.

Singh, S.C., M.A.J. Taylor, and J.P. Montagner, On the presence of liquid in Earth's inner core, *Science*, **287**, 2471-2474, 2000.

Song, X. and D.V. Helmberger, Depth dependence of anisotropy of the Earth's inner core, *J. Geophys. Res.*, **100**, 9805-9816, 1995.

Song, X. and D.V. Helmberger, A P wave velocity model of Earth's core, *J. Geophys. Res.*, **100**, 9817-9830, 1995.

Song, X., Anisotropy in central part of inner core, *J. Geophys. Res.*, **101**, 16089-16097, 1996.

Souriau, A. and M. Souriau, Ellipticity and density at the inner core boundary from sub-critical PKiKP and PcP data, *Geophys. J. Int.*, **98**, 39-54, 1989.

Souriau, A. and P. Roudil, Attenuation in the uppermost inner core from broad-band GEOSCOPE PKP data, *Geophys. J. Int.*, **123**, 572-587, 1995.

Souriau, A. and B. Romanowicz, Anisotropy in inner core attenuation: A new type of data to constrain the nature of the solid core, *Geophys. Res. Lett.*, **23**, 1-4, 1996.

Stacey, F.D., The cooling earth: A reappraisal, *Phys. Earth Planet. Inter.*, **22**, 89-96, 1980.

Stacey, F.D. and C.H.B. Stacey, Gravitational energy of core evolution: implications for thermal history and geodynamo power, *Phys. Earth planet. Int.*, **110**, 83-93, 1999.

Stixrude, L., and R.E. Cohen, High-pressure elasticity of iron and anisotropy of earth's inner core, *Science*, **267**, 1972-1975, 1995.

Stroujkova, A. and V.F. Cormier, Regional variations in the uppermost 100 km of the Earth's inner core, *J. Geophys. Res.*, **109**, 2004.

Sumita, I., S. Yoshida, M. Kumazawa, and Y. Hamano, A model for sedimentary compaction of a viscous medium and its application to inner-core growth, *Geophys. J. Int.*, **124**, 502-524, 1996.

Sumita, I. and P. Olson, A laboratory model for convection in Earth's core driven by a thermally heterogeneous mantle, *Science*, **286**, 1547-1549, 1999.

Takeuchi, N., R.J. Geller and P.R. Cummins, Highly accurate P-SV complete synthetic seismograms using modified DSM operators, *Geophys. Res. Lett.*, **23**, 1175-1178, 1996.

Taner, M.T. and F. Koehler, Velocity spectra-digital derivation and applications of velocity functions, *Geophys.*, **84**, 859-881, 1969.

Tanaka, S. and H. Hamaguchi, Degree one heterogeneity and hemispherical variation of anisotropy in the inner core from PKP(BC)-PKP(DF) times, *J. Geophys. Res.*, **102**, 2925-2939, 1997.

Tkalucic, H., B. Romanowicz, and N. Houy, Constraints on $D^{"}$ structure using PKP(AB-DF), PKP(BC-DF) and PcP-P traveltime data from broad-band records, *Geophys. J. Int.*, **148**, 599-616, 2002.

Vinnik, L., B. Romanowicz, and L. Brger, Anisotropy in the center of the inner core, *Geophys. Res. Lett.*, **21**, 1671-1674, 1994.

Wen, L. and F. Niu, Seismic velocity and attenuation structures in the top of the Earth's inner core, *J. Geophys. Res.*, **107**, 2273, 2002.

Widmer, R., G. Master and F. Gilbert, Spherically symmetric attenuation within the Earth from normal mode data, *Geophys. J. Int.*, **104**, 541-553, 1991.

Woodhouse, J.H., D. Giardini, and X.D. Li, Evidence for inner core anisotropy from free oscillations, *Geophys. Res. Lett.*, **13**, 1549-1552, 1986.